10-24-2018

BEAM THEORY FOR CLASSICAL AND QUANTUM NONLINEAR OPTICS---EXPOSING CLASSICAL AND QUANTUM CORRELATIONS OF TRANSVERSE-SPATIAL MODES

Robert Nicholas Lanning
Louisiana State University and Agricultural and Mechanical College

BEAM THEORY FOR CLASSICAL AND QUANTUM NONLINEAR OPTICS— EXPOSING CLASSICAL AND QUANTUM CORRELATIONS OF TRANSVERSE-SPATIAL MODES

A Dissertation

Submitted to the Graduate Faculty of the
Louisiana State University and
Agricultural and Mechanical College
in partial fulfillment of the
requirements for the degree of
Doctor of Philosophy

in

The Department of Physics & Astronomy

by
Robert Nicholas Lanning
B.S. Physics, Lamar University, 2012
B.S. Mathematics, Lamar University, 2012
December 2018

To my family, especially my wife Beth, for all their love and support.

Acknowledgments

The majority of this thesis is derived from the following four articles published under Copyright © 2011 by the American Physical Society (APS):

1) M. Zhang, R. N. Lanning, Z. Xiao, J. P. Dowling, I. Novikova, and E. E. Mikhailov, "Spatial multimode structure of atom-generated squeezed light", *Phys. Rev. A*, vol. 93, no. 1, p. 013853, 2016.

2) M. Zhang, M. A. Guidry, R. N. Lanning, Z. Xiao, J. P. Dowling, I. Novikova, and E. E. Mikhailov, "Multipass configuration for improved squeezed vacuum generation in hot Rb vapor", *Phys. Rev. A*, vol. 96, no. 1, p. 013835, 2017.

3) R. N. Lanning, Z. Xiao, M. Zhang, I. Novikova, E. E. Mikhailov, and J. P. Dowling, "Gaussian-beam-propagation theory for nonlinear optics involving an analytical treatment of orbital-angular-momentum transfer", *Phys. Rev. A*, vol. 96, no. 1, p. 013830, 2017.

4) R. N. Lanning, Z. Xiao, M. Zhang, I. Novikova, E. E. Mikhailov, and J. P. Dowling, "Quantized nonlinear Gaussian-beam dynamics—tailoring multimode squeezed-light generation", *Phys. Rev. A*, vol. 98, no. 4, p. 043824, 2018.

The author has the right to use the articles or portions of the articles in this thesis without requesting permission from APS, provided the bibliographic citations are given and the APS copyright credit line is given on the appropriate pages. Please see Appendix C and/or https://journals.aps.org/copyrightFAQ.html for full details.

This research was supported by the Air Force Office of Scientific Research Grant No. FA9550-13-1-0098. The author would also like to acknowledge additional support from the Army Research Office, the Defense Advanced Research Projects Agency, the National Science Foundation, and the Northrop Grumman Corporation.

Table of Contents

Abstract

Optics is arguably the most important branch of physics that has ever been studied. It is not only an essential ingredient of many other branches of physics that we study, it governs how we see, how we measure, and how we communicate in the modern world. And as the world continues to change, so do our tools and resources. In a relatively short amount of time, we have progressed from rudimentary tools that shape the world around us, to tools that harness the fundamental laws of nature. Unsurprisingly, the laws of nature governing optics remain paramount. This is because many of today's most advanced technologies rely on the classical and quantum properties of specially prepared beams of light. For example, there are quantum computing, quantum information, the quantum internet, quantum-enhanced metrology and quantum-enhanced imaging, to name a few. It is time to go a layer deeper in our understanding of these beams of light, particularly ones generated in nonlinear-optical interactions, since these are commonly the source of beams with quantum properties.

The critical observation is that in each spatial mode (or spectral mode) of light exiting a nonlinear interaction, there are actually many transverse-spatial modes that have not been fully investigated. We use a Born-like approximation and a Green's function method to predict the classical mode structure of beams created during nonlinear interactions. Then, we extend the single-mode quantum theory by developing a second-quantization procedure of the classical modes. We derive an amplitude matrix, which governs the interaction between the modes and we calculate the evolution of the system.

We show that our classical theory agrees nicely with experimental results, better than previous theories. Furthermore, we present simulations that predict ways to tailor the mode structure while adding, subtracting, and canceling orbital angular momentum transfer in nonlinear interactions. We use our quantum theory to predict the variance, covariance, the coupling of the modes, and how the noise suppression is distributed among the modes. In each case, we focus on exposing the underlying transverse spatial mode structure and suggest ways to tailor it depending on the intended use of the quantum resources. The simulations

herein illustrate the utility of our theory, which is a convenient and powerful optimization tool. It can be used to show how the interplay of experimental beam parameters can influence the quantum properties of the beam(s) generated during the interaction. For example, the mode structure of the input beam(s), along with beam waist(s) and focal position(s), can all have significant influence on the quantum properties. Coupling to the generated beam(s) can also be a formidable problem. Thus, it allows one to investigate which beam parameters should be targeted to enhance the quantum resources.

1 Introduction

1.1 Central Ideas

We are on the cusp of a new age of quantum physics and technology, where multi-spatial-mode beam propagation will play an ever more essential role. This is because a majority of the most useful quantum resources are produced during nonlinear light-matter interactions using optical beams. In these interactions, even when the incident beams have a simple structure, the properties of the output and stimulated beams can be quite complex. Recently for example, it has been particularly alluring to study nonlinear effects in response to beams carrying orbital angular momentum (OAM), which is directly related to the transverse-spatial-mode (TSM) properties of the beam. For example, a Laguerre-Gauss (LG) spatial mode, with azimuthal index ℓ, has an azimuthal phase dependence of $\exp[i\ell\phi]$, which corresponds to OAM of $\ell\hbar$ per photon [5, 6]. Conservation and storage (via slow and stopped light) of OAM have been realized in several processes, including the entanglement of OAM modes in parametric down-conversion (PDC) [7, 8], second-harmonic generation (SHG) [9], and four-wave mixing (FWM) in semiconductors [10]. Unlike solid-state processes, nonlinear optics in atomic vapors is highly efficient and requires low-light intensities. Transfer of OAM into atomic media [11–14], transfer to frequency converted light [15–21], and amplification [22] have all been observed in atomic vapors. The azimuthal structure of LG beams is only half of the story. There are also changes in the radial structure of the beam, which can be much less intuitive since there is *no known* conservation law governing the radial mode interactions.

It has been observed that the transfer of OAM to frequency converted light in atomic media is typically accompanied by a disturbance of the radial component structure, that is, frequency-converted beams have nonzero radial index p, even when the pump beams have $p = 0$ [1, 17, 23]. These effects may be subtle, or even negligible when analysis is limited

to comparing images collected with a CCD camera. However, these effects can be quite detrimental to quantum processes such as squeezing [1] and entanglement generation [24–27]. Nonlinear processes leading to the production of LG modes, with nonzero radial index p, can actually contaminate the mode structure and degrade the performance of the process. As for the ℓ structure, the conservation of OAM dictates the allowed ℓ modes of the output beam, but predicting which modes will be stimulated is not always so simple. Transfer to some of these modes can be quite improbable [17, 20], even when the interaction does not violate OAM conservation. Therefore, an analysis simply based on conservation can be quite misleading. With these concerns in mind, we develop a relatively simple, yet analytic, semiclassical theory, which predicts the spatial-mode structure of beams created during nonlinear interactions. We show that the predictions of our theory have excellent agreement with OAM transfer observations. Furthermore, the theory allows us to study and optimize the interaction to enhance performance and the output mode structure. For example, we can optimize over the beam waists, focal positions, and incident angles of the input beams to tailor the output mode structure. To demonstrate this, we simulate OAM transfer in several different nonlinear configurations, showing the addition, subtraction, and cancellation of OAM. Finally, an accurate description of the mode structure is a crucial ingredient in the general second-quantization procedure, which we delve into next.

Quantum nonlinear optical devices producing single photons, multiple photons with nonclassical correlations, and quantum fields with suppressed noise are the cornerstones of many advanced quantum technologies. For example, most high-performance schemes for quantum imaging [28–31], metrology [32–35], optomechanics [36–38], cryptography [39–41], and information [42, 43], rely on one or more these resources. The pursuit of ever better performance demands the full understanding of the spatial distribution and mode composition of quantum light. Much progress has been made on several fronts. An increasing number of studies have been performed, which investigate the spatial distribution and TSM structure of squeezed light [44]. This has prominently been done for squeezed light generated in atomic vapors via

the polarization self-rotation effect (PSR) [45–48] and FWM [49–52] processes. The squeezed vacuum generated via PSR has been studied experimentally using spatial masks [1] and optimized for various optical depths [2]; in each case elucidating more about the spatial-mode structure of the noise suppression. Squeezing generated via FWM is typically harnessed as two-mode squeezing and spatial correlations between the twin beams have also been studied in detail [53–56]. However, FWM has also been used to create a single squeezed beam, which is quadrature squeezed in a large number of spatial modes within the beam [57].

On the other hand, the problem of creating single photons and entangled photon pairs typically involves the PDC process [44,58]. Progress on this front has focused on characterizing the spectral properties and angular distribution of photons in the PDC twin beam [59–62]. One popular approach for studying the spatial mode content is the Schmidt mode analysis [63]. As an extension, these models are used to calculate the biphoton rate, coupling efficiency, and heralding efficiency [64–66]. In all of these studies, there has remained a crucial area to be investigated. In each spatial-angular mode of the output beams of FWM and PDC, there are actually many TSMs, which potentially have quantum correlations.

In this thesis, we develop a theory that predicts the TSM structure in each spatial-angular mode of FWM and PDC beams. We use this knowledge to predict the variance, covariance, and relative coupling strength between the modes [67]. Furthermore, we identify the eigenmodes of the interaction, and use these to show how to enhance the noise suppression in the system [68]. Also, we show that, under certain conditions, they can be used as a basis to represent the interaction. To demonstrate the theory, we simulate several interactions, including PSR, FWM, and PDC. In each case, we focus on exposing the underlying TSM structure and suggesting ways to tailor it depending on the intended use of the quantum resources.

In the remainder of this chapter, we will develop some of the theory necessary to understand the topics in this thesis. These sections are not intended to be comprehensive, rather, the purpose is to set a foundation from which we can begin the presentation of our

experimental discoveries and develop our corresponding theory. Therefore, we begin with a description of optical beam propagation in vacuum, followed by propagation in matter. This allows us to develop a mathematical description of the aforementioned LG modes, which are one of the *main ingredients* in our theory. The description of light propagating in matter naturally progresses to a description of nonlinear interactions, which refers to the optical response of the of the medium to the incident field. Nonlinear interactions are the source of many different interesting phenomenon, but a rigorous description is outside the scope of this thesis. Therefore, we will develop a phenomenological model, that can be used in both semiclassical and fully second-quantized treatments. We direct the reader to Refs. [44,58,69] for more complete descriptions of the topics discussed in this Chapter.

In Chapter 2 we will discuss our experimental work related to squeezing generated via PSR, which triggered our theoretical investigation of TSM structure in nonlinear optics. In Chapter 3 we develop our aforementioned theory, which begins with a semiclassical description of the interaction followed by a quantum treatment. In Chapter 4 we return to the topic of PSR squeezing, and use our theory to model our experimental results. Finally, in Chapters 5 and 6 we showcase our theory by presenting simulations of OAM transfer and spontaneous nonlinear interactions.

1.2 Beam Propagation

In this section we will develop the free-space optical-beam theory that gives rise to the Laguerre-Gauss transverse-spatial modes. Then, we will show how the the interaction of a beam with matter can induce a polarization in the medium. This polarization, which depends on the mode structure of the input beam, can act like a driving term in the inhomogeneous wave equation. Therefore, the polarization can give rise to new mode structure in the beam. Later in Chapter 3, we will present our method for solving the propagation equation, and we will develop a second-quantization procedure which describes the beam dynamics quantumly.

1.2.1 Beam Propagation In Vacuum

First, we investigate the electric field propagating in vacuum. For completeness, we start with Maxwell's equations in the absence of sources:

$$\nabla \cdot \tilde{\mathbf{E}} = 0 \tag{1.1a}$$

$$\nabla \times \tilde{\mathbf{E}} = -\frac{\partial \tilde{\mathbf{B}}}{\partial t} \tag{1.1b}$$

$$\nabla \cdot \tilde{\mathbf{B}} = 0 \tag{1.1c}$$

$$\nabla \times \tilde{\mathbf{B}} = \frac{1}{c^2}\frac{\partial \tilde{\mathbf{E}}}{\partial t}, \tag{1.1d}$$

where the tilde indicates rapidly varying quantities. To find the wave equation for the electric field, we substitute Eq. (1.1b) into the curl of Eq. (1.1d) which gives

$$\nabla \times (\nabla \times \tilde{\mathbf{E}}) = -\frac{1}{c^2}\frac{\partial^2 \tilde{\mathbf{E}}}{\partial t^2}. \tag{1.2}$$

Using a vector identity, we can rewrite the this result as

$$\nabla(\nabla \cdot \tilde{\mathbf{E}}) - \nabla^2 \tilde{\mathbf{E}} = -\frac{1}{c^2}\frac{\partial^2 \tilde{\mathbf{E}}}{\partial t^2}. \tag{1.3}$$

Then, using Eq. (1.1a) to omit the first term on the left, we find the homogeneous wave equation

$$\nabla^2 \tilde{\mathbf{E}} - \frac{1}{c^2}\frac{\partial^2 \tilde{\mathbf{E}}}{\partial t^2} = 0. \tag{1.4}$$

Focusing on a single frequency component ω, we can introduce the field $\tilde{\mathbf{E}}(\mathbf{r}, t) = \mathbf{E}(\mathbf{r})e^{-i\omega t}$ into Eq. (1.4), and find the homogeneous Helmholtz equation

$$(\nabla^2 + k^2)\mathbf{E}(\mathbf{r}) = 0. \tag{1.5}$$

Next, we will search for beam-like solutions to the wave equation. Beams have two

distinct properties. First, their intensity drops off very rapidly in the direction transverse to the direction of propagation, and second, their intensity changes very little along the direction of propagation. To model these properties, we let the z axis be the axis of propagation, and further assume that the field is a plane wave with a spatially modulated amplitude

$$\mathbf{E}(\mathbf{r}) = \boldsymbol{\mathcal{E}}(\mathbf{r}_\perp, z)e^{ikz}, \tag{1.6}$$

where $\mathbf{r}_\perp \equiv x\,\hat{\mathbf{x}} + y\,\hat{\mathbf{y}}$. To target the z dependence, we define

$$\nabla_\perp^2 + \frac{\partial^2}{\partial z^2} \equiv \frac{\partial^2}{\partial x^2} + \frac{\partial^2}{\partial y^2} + \frac{\partial^2}{\partial z^2} = \nabla^2, \tag{1.7}$$

and use these last two definitions in Eq. (1.5) to find an equation for the modulation function:

$$\big(\nabla_\perp^2 + 2ik\frac{\partial}{\partial z} + \frac{\partial^2}{\partial z^2}\big)\boldsymbol{\mathcal{E}} = \mathbf{0}. \tag{1.8}$$

Now, we make our statement about the properties of beams more rigorous and assume that $\boldsymbol{\mathcal{E}}(\boldsymbol{r}_\perp, z)$ changes very slowly in the z direction over the wavelength $\lambda = 2\pi/k$. Mathematically, this statement corresponds to what is known as the paraxial approximation,

$$\big|k\,\frac{\partial \mathcal{E}}{\partial z}\big| \gg \big|\frac{\partial^2 \mathcal{E}}{\partial z^2}\big|, \tag{1.9}$$

and allows us to drop the last term in Eq. (1.8). Rearranging terms, we find the homogeneous paraxial wave equation

$$\big(\frac{\partial}{\partial z} - \frac{i}{2k}\nabla_\perp^2\big)\boldsymbol{\mathcal{E}} = 0. \tag{1.10}$$

From this point forward, we consider beams with cylindrical symmetry. In cylindrical coordinates, the homogeneous paraxial wave equation gives rise to the LG family of solu-

tions [70]:

$$u_{\ell,p}(\vec{r}) = \frac{C_{\ell,p}}{w(z)} \exp\Big(-\frac{r^2}{w(z)^2}\Big) \exp\Big(-\frac{ikr^2 z}{2(z^2+z_R^2)}\Big)\Big(\frac{\sqrt{2}r}{w(z)}\Big)^{|\ell|} \times L_p^{|\ell|}\Big(\frac{2r^2}{w(z)^2}\Big) \exp(i\ell\phi) \exp\Big(i(2p+|\ell|+1)\arctan(z/z_R)\Big), \tag{1.11}$$

where ℓ is the azimuthal index, p is the radial index for each mode, $C_{\ell,p} = \sqrt{2p!/\pi(|\ell|+p)!}$ is a normalization constant, w_0 is the beam waist, $w(z) = w_0\sqrt{1+(z/z_R)^2}$ is the width function of the beam, $L_p^{|\ell|}$ are the generalized Laguerre polynomials, $z_R = \pi w_0^2/\lambda$ is the Rayleigh range, and $k = 2\pi/\lambda$ is the wave number.

In Figures 1.1(b)–1.1(d), we present numerous LG modes, showing how the intensity profile changes with respect to the azimuthal index ℓ, the radial index p, and superpositions thereof. For $\ell = p = 0$, we have the fundamental Gaussian mode, which describes, for

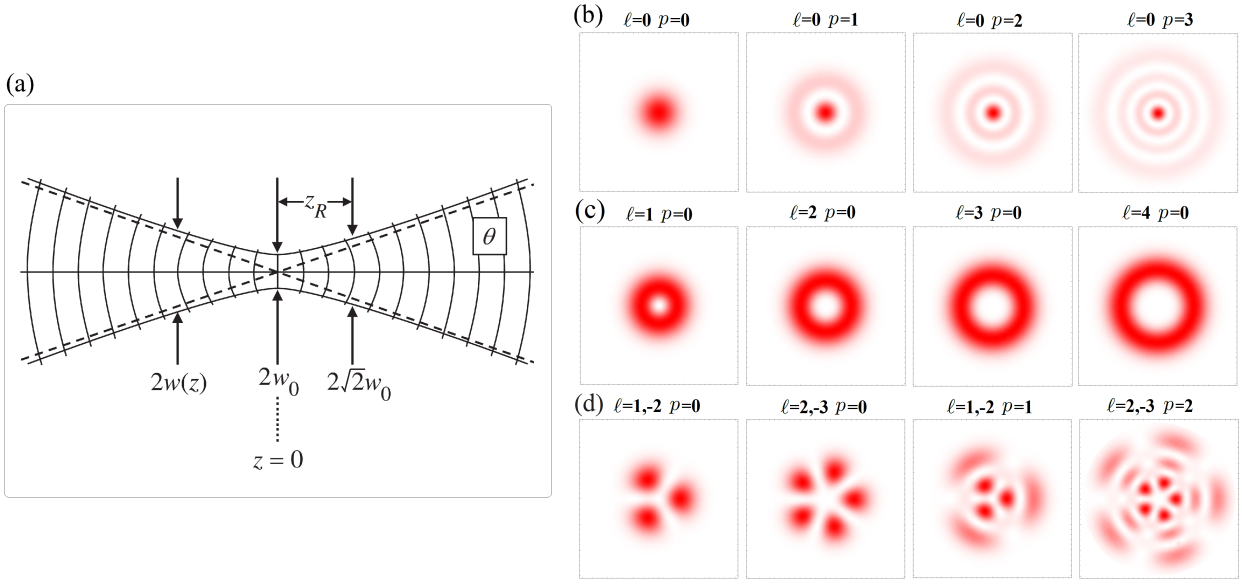

Figure 1.1. (a) LG mode propagation along the beam axis z; w_0 is the beam waist, $w(z)$ is the width function of the beam, and z_R is the distance from the focus that the waist grows by $\sqrt{2}$, otherwise referred to as the Rayleigh range, LG mode intensity profiles for (b) $\ell = 0$ and increasing p, (c) $p = 0$ and increasing ℓ, and (d) for several superpositions of ℓ with $p \leq 2$. Due to interference, superpositions with ℓ's of opposite sign will have a symmetric petal-like structure with $|\ell_1| + |\ell_2|$ petals. If these superpositions also have nonzero p, then there will be a ring-like structure similar to (a), but also with a petal-like structure.

example, an ideal laser beam. When the radial index p is increased, rings appear around a central Gaussian spot. When $p = 0$ and ℓ is increased, the central spot is replaced by a thick ring, sometimes referred to as a "donut mode". The diameter of the donut mode increases as ℓ increases, and the azimuthal phase dependence $\exp[i\ell\phi]$ gives a vortex like phase structure, that also intensifies with ℓ. In other words, ℓ gives the number of times the light twists around the z axis in one wavelength. The azimuthal phase dependence also corresponds to OAM of $\ell\hbar$ per photon [5, 6]. Superpositions of positive and negative ℓ's interfere to create petal patterns of light and dark fringes, such as Fig. 1.1(d). The number of petals is determined by the azimuthal induces of the beams in the superposition. For example, in the row of Fig. 1.1(d) we see $|1| + |-2| = 3$ lobes, and then $|2| + |-3| = 5$ lobes. See Reference [6] for an excellent description of optical OAM origins and behavior, including visualizations of the phase-vortex nature of beams carrying OAM.

1.2.2 Beam Propagation In Matter

We have shown how Maxwell's equations can give rise to the paraxial wave equation and the LG modes. Next, we will investigate the propagation of beams through an optical medium. Similar to the previous section, we want to derive the paraxial wave equation, except now in the presence of a polarizable material. Therefore, we start with Maxwell's equations in matter:

$$\nabla \cdot \tilde{\mathbf{D}} = \tilde{\rho} \tag{1.12a}$$

$$\nabla \times \tilde{\mathbf{E}} = -\frac{\partial \tilde{\mathbf{B}}}{\partial t} \tag{1.12b}$$

$$\nabla \cdot \tilde{\mathbf{B}} = 0 \tag{1.12c}$$

$$\nabla \times \tilde{\mathbf{H}} = \frac{\partial \tilde{\mathbf{D}}}{\partial t} + \tilde{\mathbf{J}}. \tag{1.12d}$$

We are actually interested in situations where the material is non magnetic, has no free charges, and no free currents. In this scenario we can establish:

$$\tilde{\mathbf{B}} = \mu_0 \tilde{\mathbf{H}} \tag{1.13a}$$

$$\tilde{\rho} = 0 \tag{1.13b}$$

$$\tilde{\mathbf{J}} = 0. \tag{1.13c}$$

However, we do allow for the rearrangement of the internal charge density in response to the applied field $\tilde{\mathbf{E}}$. This response is described by the polarization of the medium $\tilde{\mathbf{P}}$, and it is traditional to define the auxiliary field $\tilde{\mathbf{D}}$ in such a way to combine the two:

$$\tilde{\mathbf{D}} = \epsilon_0 \tilde{\mathbf{E}} + \tilde{\mathbf{P}}. \tag{1.14}$$

We now proceed as we did in the previous section. We use Eq. (1.12b) to replace $\tilde{\mathbf{H}}$ in the curl of Eq. (1.12d). This step, along with the conditions in Eq. (1.13a), allow us to find

$$\nabla \times (\nabla \times \tilde{\mathbf{E}}) = -\mu_0 \frac{\partial^2 \tilde{\mathbf{D}}}{\partial t^2}. \tag{1.15}$$

From here, we can eliminate $\tilde{\mathbf{D}}$ using Eq. 1.14 and find

$$\nabla(\nabla \cdot \tilde{\mathbf{E}}) - \nabla^2 \tilde{\mathbf{E}} + \frac{1}{c^2} \frac{\partial^2 \tilde{\mathbf{E}}}{\partial t^2} = -\frac{1}{\epsilon_0 c^2} \frac{\partial^2 \tilde{\mathbf{P}}}{\partial t^2}, \tag{1.16}$$

where we have used $\epsilon_0 \mu_0 = c^{-2}$ and the same vector identity used in the previous section. Now, since we intend to use the inhomogeneous wave equation to describe nonlinear interactions in the next section, we have to be careful with the left-hand side. In general, the $\nabla \cdot \tilde{\mathbf{E}}$ term does not vanish in nonlinear interactions. However, it can be neglected since we will operate in the slowly varying amplitude approximation.

Therefore, we have found a form of the inhomogeneous wave equation that will suit our

needs for nonlinear optics:

$$\nabla^2\tilde{\mathbf{E}} - \frac{1}{c^2}\frac{\partial^2\tilde{\mathbf{E}}}{\partial t^2} = \frac{1}{\epsilon_0 c^2}\frac{\partial^2\tilde{\mathbf{P}}}{\partial t^2}. \tag{1.17}$$

Assuming phase matching, we introduce the field $\tilde{\mathbf{E}}(\mathbf{r},t) = \mathbf{E}(\mathbf{r})e^{-i\omega t}$ *and* the polarization $\tilde{\mathbf{P}}(\mathbf{r},t) = \mathbf{P}(\mathbf{r})e^{-i\omega t}$ into Eq. (1.17) and find the inhomogeneous Helmholtz equation. Next, we let $\mathbf{E}(\mathbf{r}) = \boldsymbol{\mathcal{E}}(\mathbf{r}_\perp, z)e^{ikz}$, $\mathbf{P}(\mathbf{r}) = \boldsymbol{\mathcal{P}}(\mathbf{r}_\perp, z)e^{ikz}$, and along with the paraxial approximation ($|k\,\partial\mathcal{E}/\partial z| \gg |\partial^2\mathcal{E}/\partial z^2|$) we transform the Helmholtz equation into the inhomogeneous paraxial wave equation

$$(\frac{\partial}{\partial z} - \frac{i}{2k}\nabla_\perp^2)\boldsymbol{\mathcal{E}} = \frac{ik}{2\epsilon_0}\boldsymbol{\mathcal{P}}. \tag{1.18}$$

Depending on the scenario, there are several methods available for modeling the polarization $\boldsymbol{\mathcal{P}}$, and in many cases a simple phenomenological approach will lead to interesting and accurate results. Regardless of the method used, the polarization is, in general, a complicated function of the field, that is, $\boldsymbol{\mathcal{P}} = \boldsymbol{\mathcal{P}}(\boldsymbol{\mathcal{E}})$. Thus, once $\boldsymbol{\mathcal{P}}(\boldsymbol{\mathcal{E}})$ is known, there remains the difficult task of finding solutions to Eq. 1.18, which can be a coupled set of equations relating, for example, the different $\hat{\mathbf{x}}$-, $\hat{\mathbf{y}}$-, and $\hat{\mathbf{z}}$-polarization components of the field. In order to delve into the mathematical structure and phenomenon related to the polarization $\boldsymbol{\mathcal{P}}$, we'll transition to field of nonlinear optics.

1.3 Nonlinear Optics

Nonlinear optics is the study of phenomenon that arise from the modification of the optical properties of a material by the presence of incident light. Nonlinear phenomenon are "nonlinear" in the sense that they occur when the response of the material, to the incident optical field, depends in a nonlinear manner on the strength of the optical field. As we developed in the previous section, the response of the material can be characterized by the polarization $\tilde{\mathbf{P}}$, and can act as a driving term in the inhomogeneous wave equation. Therefore, it is natural to expect that the polarization can be expanded in a power series of

the incident optical field. In fact, the general rule is that

$$\tilde{P}_i = \epsilon_0 \chi^{(1)}_{ij} \tilde{E}_j + \epsilon_0 \chi^{(2)}_{ijk} \tilde{E}_j \tilde{E}_k + \epsilon_0 \chi^{(2)}_{ijk\ell} \tilde{E}_j \tilde{E}_k \tilde{E}_\ell + \cdots, \tag{1.19}$$

where $\chi^{(i)}$ is the ith order susceptibility tensor of the interaction. The tensor nature of the susceptibilities allows for the possibility that $\tilde{\mathbf{P}}$ is not actually parallel to $\tilde{\mathbf{E}}$. Thankfully, most of the interactions of interest in quantum optics do not require the full tensor nature of the susceptibility. This is because the field of interest $\tilde{E}_{\text{stim}}$, stimulated by $\tilde{\mathbf{P}}$, in many cases began as a vacuum input or a weak probe. Furthermore, symmetries in the material often reduce the complexity of the susceptibility χ, effectively decoupling the interaction. Therefore, it suffices to drop the vector nature of the fields and separate the polarization response into its respective terms:

$$\tilde{P}^{(1)}_{\text{stim}} = \epsilon_0 \chi^{(1)} \tilde{E}_1 \tag{1.20a}$$

$$\tilde{P}^{(2)}_{\text{stim}} = \epsilon_0 \chi^{(2)} \tilde{E}_1 \tilde{E}_2 \tag{1.20b}$$

$$\tilde{P}^{(3)}_{\text{stim}} = \epsilon_0 \chi^{(3)} \tilde{E}_1 \tilde{E}_2 \tilde{E}_3, \tag{1.20c}$$

where $\tilde{E}_i$ refer to the relevant components of the incident optical field, and $\chi^{(j)}$ is simply a constant which scales these field components to the polarization $\tilde{P}^{(j)}$. The fields $\tilde{E}_i$ could be different polarization components, different frequency components, different spatial modes, etc. Therefore, there may be situations where one or more fields could be complex conjugated, which would indicate that a photon is being created in that field, as opposed to annihilated. We will see the quantum optics analog in the next section. In any case, as long as we have found a way to decouple the interaction, we can use the form of Eq. (1.20) in Eq. (1.17) to find the new components of the field, stimulated by the nonlinearity.

The field of nonlinear optics was sparked shortly after the invention of the laser, when second-harmonic generation was discovered by Franken *et al.* in 1961. The phenomenon is

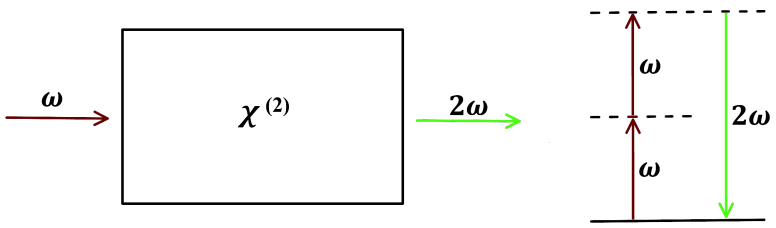

Figure 1.2. Schematic and energy diagram of the second-harmonic generation interaction discovered by Franken *et.al.* in 1961. Two pump photons are absorbed and one signal photon is created in their place. Thus, it has twice the energy of a pump photon and frequency 2ω.

a second-order interaction, and it can be described by the polarization

$$\tilde{P}^{(2)}(2\omega) = \epsilon_0 \chi^{(2)} \tilde{E}^2(\omega), \tag{1.21}$$

where in this case, the electric field is degenerate since there is a single pump laser. This polarization represents the response at 2ω due to the annihilation of two pump photons at ω (see Fig. 1.2). One of the main objectives of this thesis is to show how one can find the TSM properties of the generated beam, for this type interaction, and for more sophisticated interactions. In Chapter 3 we develop the theory, and in Chapter 5 we use it to simulate OAM transfer in several nonlinear interactions. Another objective is to show how one can predict the quantum properties of these beams; thus, in the next section we develop the groundwork of quantum-nonlinear optics.

1.4 Quantum Optics

The prototypical quantum optics problem is to second-quantize the electromagnetic field confined to a one-dimensional conducting cavity. The first step is to solve the problem classically, find the mode structure, then quantize the modes. This is formally equivalent to solving the quantum harmonic oscillator, which is a standard problem in undergraduate quantum texts. It is traditional to introduce the annihilation ($\hat{a}$) and creation ($\hat{a}^\dagger$) operators (for a single field-mode), that satisfy the commutation relation

$$[\hat{a},\, \hat{a}^\dagger] = 1, \tag{1.22}$$

and allow us to write the Hamiltonian operator as

$$\hat{H} = \hbar\omega\big(\hat{a}^\dagger\hat{a} + \frac{1}{2}\big). \tag{1.23}$$

We let $|n\rangle$ denote the energy eigenstate of the field and find that

$$\hat{H}|n\rangle = \hbar\omega\big(n + \frac{1}{2}\big)|n\rangle = E_n|n\rangle, \tag{1.24}$$

where E_n is are the energy eigenvalues. Thus, defining the number operator $\hat{n} = \hat{a}^\dagger\hat{a}$, we are able to expose the *photon number* according to $\hat{n}|n\rangle = n|n\rangle$. In other words, the energy eigenstates have a precisely know photon number [see Fig. 1.3(a)], and are often referred to as the number states. Upon normalizing the number states, we see that as the name suggests, the annihilation and creation operators change the energy of the system by adding

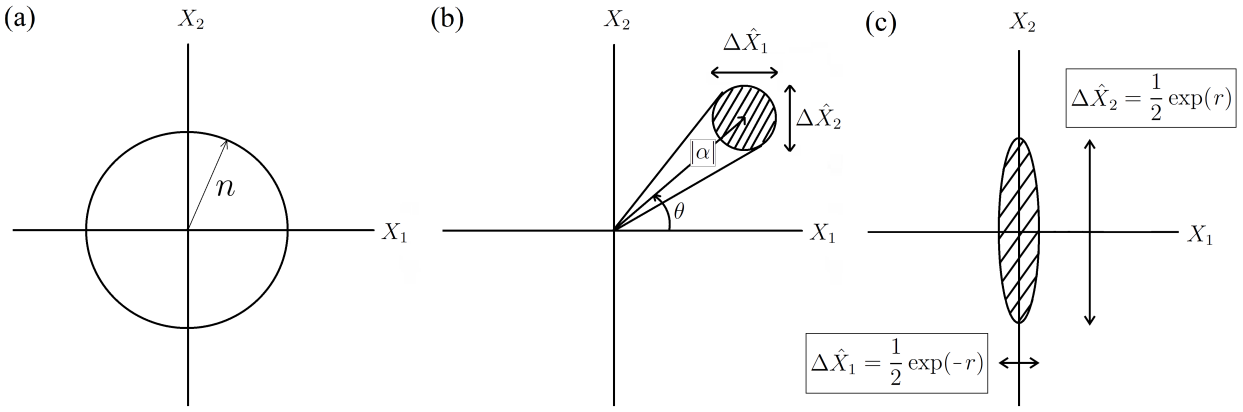

Figure 1.3. (a) Phase space representation of a number state, (b) the coherent state, and (c) the squeezed vacuum state. The axis X_1, X_2 are the quadratures of the electromagnatic field. In (a) we see that, for the number state, the photon number n is precisely known but the phase is completely uncertain. In (b) we see the coherent state, which can be interpreted as a displaced vacuum state with amplitude $|\alpha|$ and phase θ, where $\alpha = |\alpha|\exp(i\theta)$. The noise of the coherent state is that of the vacuum, thus $\Delta\hat{X}_1 = 1/2 = \Delta\hat{X}_2$. In (c) we see the squeezed vacuum state for the special case that the squeezing angle $\theta = 0$. When $\theta \neq 0$, the noise ellipse is simply rotated by $\theta/2$ from the X_1-axis.

and removing photons from the cavity:

$$\hat{a}|n\rangle = \sqrt{n}\,|n-1\rangle \tag{1.25a}$$

$$\hat{a}^\dagger|n\rangle = \sqrt{n+1}\,|n+1\rangle. \tag{1.25b}$$

Furthermore, the number states can be generated from the vacuum $|0\rangle$ by repeated action of the creation operator:

$$|n\rangle = \frac{(\hat{a}^\dagger)^n}{\sqrt{n!}}\,|0\rangle. \tag{1.26}$$

The number states may be states of well defined energy, but they are not states of well defined electric field. In fact,

$$\langle\hat{E}\rangle = \langle n|\,\hat{E}\,|n\rangle = 0, \tag{1.27}$$

where $\hat{E} = \hat{E}(z,t) = A(\hat{a}+\hat{a}^\dagger)\sin(kz)$ is the electric field operator of the 1D cavity and A is a constant. The mean field may be zero, but the mean-square field is not, and this leads us to a discussion of the fluctuations in the field. The fluctuation in the electromagnetic field is typically characterized by the variance, and it is traditional to define the quadrature operators, which are the scaled-dimensionless electric and magnetic fields:

$$\hat{X}_1 = \frac{1}{2}(\hat{a}+\hat{a}^\dagger) \tag{1.28}$$

$$\hat{X}_2 = \frac{1}{2i}(\hat{a}-\hat{a}^\dagger). \tag{1.29}$$

They satisfy the commutation relation $[\hat{X}_1,\,\hat{X}_2] = i/2$, from which an uncertainty relation follows:

$$\langle(\Delta\hat{X}_1)^2\rangle\langle(\Delta\hat{X}_2)^2\rangle \geq \frac{1}{16}. \tag{1.30}$$

For the number states $\langle\hat{X}_1\rangle = 0 = \langle\hat{X}_2\rangle$, but $\langle\hat{X}_1^2\rangle = (2n+1)/4 = \langle\hat{X}_2^2\rangle$, which reveals that the noise is balanced in both quadratures. Note that even for the vacuum state (n=0), the

field has fluctuations, the so-called vacuum fluctuations:

$$\langle(\Delta\hat{X}_1)^2\rangle_{\text{vac}} = \frac{1}{4} = \langle(\Delta\hat{X}_2)^2\rangle_{\text{vac}}. \tag{1.31}$$

An introduction to quantum optics would not be complete without mention of the coherent states. The coherent state $|\alpha\rangle$ is the eigenstate of the annihilation operator, and is more classical than a number state, in the sense that

$$\langle\alpha|\,\hat{E}\,|\alpha\rangle \propto |\alpha|\sin(kz+\theta) \tag{1.32}$$

looks like a classical field, where $\alpha = |\alpha|e^{i\theta}$ is the amplitude of the state. The coherent states are also classical-like states because they contain only the noise from the vacuum:

$$\langle(\Delta\hat{X}_1)^2\rangle_{\alpha} = \frac{1}{4} = \langle(\Delta\hat{X}_2)^2\rangle_{\alpha}. \tag{1.33}$$

In this sense, they can be thought of as displaced vacuum states, with the position in phase space given by the complex amplitude α [see Fig. 1.3(b)]. The coherent states can be created (at least mathematically) by applying the displacement operator

$$\hat{D}(\alpha) = \exp(\alpha\hat{a}^\dagger - \alpha^*\hat{a}), \tag{1.34}$$

to the vacuum state. Continuing the theme of modified vacuum fluctuations, we move on to the topic of squeezed states.

Squeezed states are quantum states in which the quadrature noise is unbalanced between the quadratures, without violating the uncertainty principle in Eq.(1.30). This is in contrast to the vacuum and coherent states, in which the noise is balanced. These states remain an active area of research to this day because they are a resource in quantum-enhanced metrology. There are measurement schemes, for example interferometry, where the ultimate precision of

the measurement is limited by the quantum noise of the state of light used. Therefore, using states with suppressed noise can boost the ultimate precision of the measurement scheme.

The simplest example is the single-mode squeezed vacuum, which can be generated (at least mathematically) by the squeezing operator

$$\hat{S}(\xi) = \exp\left[\frac{1}{2}(\xi^* \hat{a}^2 - \xi \hat{a}^{\dagger 2})\right], \tag{1.35}$$

where $\xi = re^{i\theta}$, r is the squeezing parameter, and θ is the squeezing angle. We will discuss the physical processes that generate squeezing below. The $\hat{a}^2$ and $\hat{a}^{\dagger 2}$ in the squeezing operator indicate that photons will be created or destroyed in pairs, thus it is a kind of two-photon generalization of the displacement operator used to create the coherent state. In this case however, the noise in the state is squeezed. To see this, we can calculate the quadrature variances for the vacuum squeezed state and find

$$\langle(\Delta\hat{X}_1)^2\rangle_\xi = \frac{1}{4}[\cosh^2 r + \sinh^2 r - 2\sinh r \cosh r \cos\theta] \tag{1.36}$$

$$\langle(\Delta\hat{X}_2)^2\rangle_\xi = \frac{1}{4}[\cosh^2 r + \sinh^2 r + 2\sinh r \cosh r \cos\theta]. \tag{1.37}$$

These equations give the quadrature variance of the noise ellipse squeezed by r, for example Fig. 1.3(c), but oriented in phase space by the angle $\theta/2$ from the X_1 axis. For the special case that the squeezing angle $\theta = 0$, the variances reduce to

$$\langle(\Delta\hat{X}_1)^2\rangle_\xi = \frac{1}{4}\exp(-2r) \tag{1.38}$$

$$\langle(\Delta\hat{X}_2)^2\rangle_\xi = \frac{1}{4}\exp(2r), \tag{1.39}$$

and we see that all the noise suppression exists totally in the $\hat{X}_1$ quadrature [see Fig. 1.3(c)]. Next, we will discuss the physical processes that can lead to squeezing, and show how the process leads the the squeezing operator in Eq. (1.35).

The squeezing process actually leads us back to the topic of nonlinear optics. The squeez-

ing operator is nonlinear in the creation and annihilation operators, because it represents the evolution in a nonlinear optical medium. In this case, Eq. (1.35) is the result of a degenerate PDC process, in which a pump photon ω_p is destroyed and two signal photons are created with frequency $\omega_s = \omega_p/2$. The Hamiltonian for this process is given by

$$\hat{H} = \hbar\omega_s\, \hat{a}^\dagger \hat{a} + \hbar\omega_p\, \hat{b}^\dagger \hat{b} + i\hbar\chi^{(2)}(\hat{a}^2\hat{b}^\dagger - \hat{a}^{\dagger 2}\hat{b}), \tag{1.40}$$

where $\hat{a}$ is the signal mode, $\hat{b}$ is the pump laser mode, and $\chi^{(2)}$ is the second order nonlinear susceptibility. We assume that the pump is a strong (undepleted) coherent state and approximate the mode $\hat{b}$ with $\beta e^{-i\omega_p t}$. Therefore, we can drop the insignificant constant term and rewrite the Hamiltonian as

$$\hat{H} = \hbar\omega_s\, \hat{a}^\dagger \hat{a} + i\hbar\chi^{(2)}(\hat{a}^2\beta^* e^{i\omega_p t} - \hat{a}^{\dagger 2}\beta e^{-i\omega_p t}). \tag{1.41}$$

Next, we transform to the interaction picture and obtain

$$\hat{H}_I = i\hbar\chi^{(2)}\big(\hat{a}^2\beta^* e^{i(\omega_p - 2\omega)t} - \hat{a}^{\dagger 2}\beta e^{-i(\omega_p - 2\omega)t}\big). \tag{1.42}$$

If we assume perfect phase matching, we can drop the exponential term and the Hamiltonian becomes time-independent. Therefore, the associated evolution operator is

$$\hat{U} = \exp\Big(-\frac{i}{\hbar}\int dt\, \hat{H}_I\Big) = \exp\Big[\frac{1}{2}(\xi^*\hat{a}^2 - \xi\hat{a}^{\dagger 2})\Big], \tag{1.43}$$

where $\xi \equiv 2\chi^{(2)}\beta t$. Thus, we see that the evolution generated by this nonlinear Hamiltonian is precisely the squeezing operator introduced in Eq. (1.35). Now that we have discussed how to create squeezed vacuum, we'll move on to how to detect it.

There are several possible ways to detect squeezed light, but we will consider the only method relevant to this thesis, the one known as balanced homodyne detection. This detec-

tion scheme (and heterodyne for that matter) was actually developed in the field of radio waves and microwaves. The basic idea is to mix a weak signal with a strong signal, referred to as the local oscillator (LO), and detect the intensity in such a way to access properties of the weak signal. This detection scheme is referred to as *balanced* because it uses two detectors (photodiodes) at the output of a balanced (50:50) beam splitter. Furthermore, it is *homodyne* because the signal and LO are the same frequency, it most cases derived from the same laser source. A balanced homodyne detection scheme is depicted in Fig. 1.4(a). From the formalism for beam splitters, we find the relation between the input ($\hat{a}$, $\hat{b}$) and output ($\hat{c}$, $\hat{d}$) modes of the beam splitter:

$$\begin{aligned} \hat{c} &= \frac{1}{\sqrt{2}}(\hat{a} + i\hat{b}) \\ \hat{d} &= \frac{1}{\sqrt{2}}(\hat{b} + i\hat{a}). \end{aligned} \tag{1.44}$$

The detectors at the output of the beam splitters detect the intensities $I_c = \langle \hat{c}^\dagger \hat{c} \rangle$ and $I_d = \langle \hat{d}^\dagger \hat{d} \rangle$, and we define their difference as $\langle \hat{n}_{cd} \rangle = \langle \hat{c}^\dagger \hat{c} - \hat{d}^\dagger \hat{d} \rangle$. Using Eq. (1.44) and some

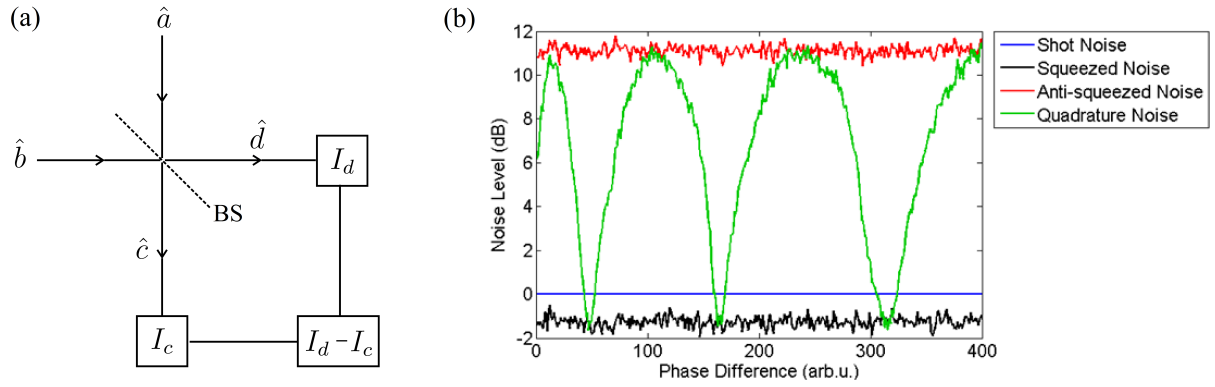

Figure 1.4. (a) Balanced homodyne detection scheme and (b) experimental squeezed vacuum noise data measured using balanced homodyne detection. In (a) the two modes $\hat{a}$ and $\hat{b}$ are mixed on a 50:50 beam splitter (BS), and sent to the intensity detectors I_c and I_d. Intensity differencing leads to the noise plotted in (b). The squeezed field is blocked in order to attain the shot noise limit (blue line). Then, the phase of the LO is changed to reveal the oscillating nature of the noise.

algebra we are able to find

$$\langle \hat{n}_{cd} \rangle = i\langle \hat{a}^\dagger \hat{b} - \hat{a}\hat{b}^\dagger \rangle. \tag{1.45}$$

Next, we'll assume that the $\hat{a}$ mode is our signal which we can set as $\hat{a} = \hat{a}_0 e^{-i\omega t}$, and that the $\hat{b}$ mode is a strong coherent state $|\beta e^{-i\omega t}\rangle$ where $\beta = |\beta| e^{-i\phi}$. Letting $\theta = \phi + \pi/2$ we may write $\langle \hat{n}_{cd} \rangle = 2|\beta| \langle \hat{X}(\theta) \rangle$, where $\langle \hat{X}(\theta) \rangle = (\hat{a}_0 e^{-i\theta} + \hat{a}_0^\dagger e^{i\theta})/2$ is the field quadrature operator at the angle θ. Thus, we see that the intensity difference measurement is proportional to a quadrature measurement. It follows that the variance of the intensity difference operator $\hat{n}_{cd}$, in the limit of a strong LO is

$$\Big\langle (\Delta \hat{n}_{cd})^2 \Big\rangle = 4|\beta|^2 \Big\langle (\Delta \hat{X}(\theta))^2 \Big\rangle, \tag{1.46}$$

which allows one to access the quadrature noise of the signal. Therefore, by adjusting θ, which can be done by adjusting ϕ of the LO, one can measure the noise of an arbitrary quadrature of the signal field. In an actual experiment, the signal would first be blocked in order to find the shot-noise limit, which is the blue line in Fig. 1.4(b). Then, the signal will be unblocked, and θ will be adjusted to find the lowest possible noise, which corresponds directly to the maximum amount of quadrature squeezing. As long as there is not too much excess noise in the experiment, the noise signal will dip below the shot-noise limit.

2 Experimental Motivation — PSR Squeezing

In this chapter we introduce the experimental discoveries that triggered our theoretical investigation of beam dynamics in nonlinear interactions. These discoveries were part of a collaborative effort between the Quantum Science and Technologies Group at Louisiana State University and the Quantum Optics Group at The College of William and Mary. This chapter is largely based on our collaborative papers, which investigated the spatial structure of atom-generated squeezed vacuum.

Our original goal was to investigate how squeezed vacuum, generated via the PSR effect, is effected by the change of the optical depth of the nonlinear medium; in this case warm ^{87}Rb vapor. One of the preliminary steps was to verify, as was then expected, that the TSM properties of the output beam, and squeezed field, were the same as the pump beam. However, on the contrary, preliminary results suggested a rich *and perplexing* mode structure, one that demanded a more rigorous explanation. Therefore, we proceeded by studying the spatial dependence of squeezing using spatial masks in two different beam configurations. This experimental study and subsequent theoretical development led to clear evidence of the higher-order mode structure of the squeezed beam. Then, turning full circle, we used configurations where the beams traversed the vapor cell multiple times to investigate how the mode structures changes with the optical depth of the ^{87}Rb vapor. Finally, we used a double-cell configuration to investigate if the first cell can act as a mode-prep or mode-filter to enhance the amount of squeezing generated in the second cell.

In order to explain our findings, this chapter is organized as follows. In Section 2.1 we give a brief description of the experimental apparatus and the generation of squeezed vacuum via the PSR effect. In Section 2.2 we present our study of the transverse-spatial mode properties of PSR squeezing using spatial masks. Lastly, in Section 2.3 we present our study of multi-pass and double-cell configurations, which allowed the investigation of the optical depth dependence of squeezing.

2.1 Generation of Squeezed Light via PSR

2.1.1 Qualitative Explanation

The PSR effect is a variant of the general four-wave mixing interaction, which can take place in $\chi^{(3)}$ nonlinear materials [see Fig. 2.1(a)]. These materials exhibit an intensity dependent index of refraction, and this phenomenon is the key to the classical description of PSR. The polarization of the electric field can be decomposed into x- and y-components, and depicted by a polarization ellipse, as in Fig. 2.1(b). Since the intensity of the two components are different, they experience different induces of refraction in the nonlinearity, thus acquiring a phase shift. This phase shift between the components manifests as a rotation of the polarization ellipse. Thus, it would appear that E_x was amplified and E_y was attenuated. Interestingly, the interaction persists even if only vacuum fluctuations enter the x-polarized port [see Fig. 2.1(c)]. Furthermore, as in the classical case, the vacuum in the x polarization can experience a phase-sensitive amplification by the y-polarized pump beam. It is this phase-sensitive amplification that gives rise to squeezing in the PSR scheme, and a more complete description is developed Chapter 4.

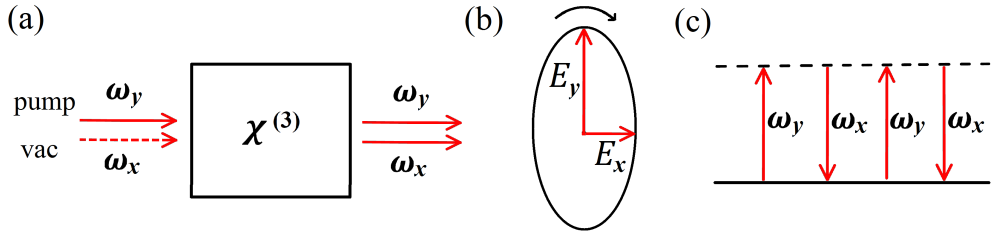

Figure 2.1. Description of the PSR effect used in our experiment. In (a) we depict the four wave mixing interaction between a y-polarized pump beam and vacuum fluctuations in the x polarization. Classically, the interaction can be described using the polarization ellipse in (b); suppose E_y is a strong pump and E_x is a weak probe, the two fields experience different induces of refraction in the $\chi^{(3)}$ material, and this causes the polarization ellipse to rotate. Quantumly, the interaction takes place even if E_x is blocked, in other words, even if vacuum fluctuations enter the x-polarized port. In (c) we depict the energy level diagram describing the quantum interaction between the x- and y-polarization modes.

2.1.2 Experimental Apparatus

Squeezing via PSR is arguably the simplest way to create squeezed vacuum, which should be evident by the depiction of the experimental apparatus in Fig. 2.2. The beauty of this configuration is twofold. First, the pump beam and squeezed beam are co-propagating, and second, the modified pump beam exiting the vapor cell acts as the LO in the detection scheme. This makes the alignment relatively simple and reduces the number of necessary optical components. Furthermore, the compact layout and robustness makes this method ideal for quantum enhanced magnetometry [71].

A cavity diode laser was detuned approximately 100 MHz to the red of the $5^2S_{1/2}, F = 2 \rightarrow 5^2P_{1/2}, F' = 2$ transition of ^{87}Rb ($\lambda \simeq 795$ nm). The laser output was spatially filtered by passing it through a single-mode-polarization-maintaining (SMPM) fiber, linearly

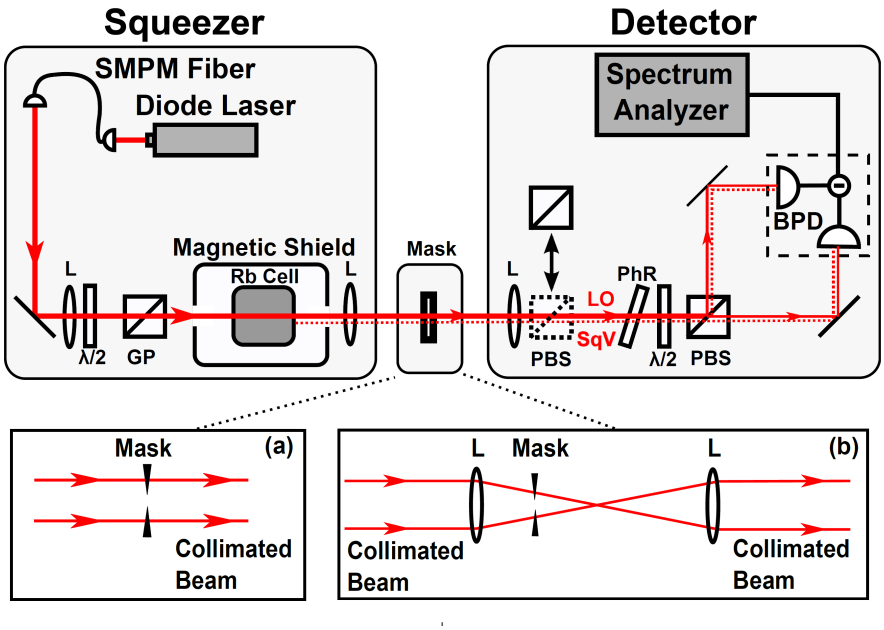

Figure 2.2. Detailed diagram describing an experimental setup used to generate squeezed light via PSR. SMPM is a single-mode polarization-maintaining fiber, $\lambda/2$ is a half wave plate, GP is a Glan-laser polarizer, PBS is a polarizing beam splitter, PhR is a phase-retarding wave plate, and BPD is a balanced photodetector. The PBD is inserted to eject the squeezed field and determine the shot noise (standard quantum limit). To investigate the spatial mode properties, different masks were inserted in either a (a) collomated beam or a (b) focused beam before the detector.

polarized using a Glan-laser polarizer (GP) and focused into a 7.5-cm long cylindrical Pyrex cell with isotopically enriched ^{87}Rb vapor and no buffer gas. The waist of the focused beam (diameter 100 μm at $1/e^2$ intensity level) was located 6.5 cm from the front of the cell. The cell was mounted inside three layer μ-metal magnetic shielding, and maintained at a constant temperature of 66°C, corresponding to a Rb density of 5.4×10^{11} cm^{-3}.

In order to measure quadrature noise of the modified vacuum field, we rotated the polarization of the two fields by 45° and mixed them on a polarization beam splitter (PBS) before sending them to a balanced photodiode (BPD). We thus realized a homodyne detection in which the strong laser field served as the LO [71, 72]. The relative phase (quadrature angle) of the two fields was adjusted by tilting the phase-retarding (PhR) plate (a birefringent quarter-wave plate with a crystal axis set parallel to the LO polarization). All the measurements discussed here were performed at 1-MHz detection frequency with 100-kHz resolution and 30-Hz video bandwidths. To calibrate the SQL (Standard Quantum Limit, i.e., shot-noise) level, we inserted an additional PBS into the beam after the cell, which reflects the squeezed field and passes only the LO field.

2.2 Investigation with Spatial Masks

All previous experimental and theoretical analysis of PSR squeezing assumed an identical single spatial mode for both the strong pump and vacuum fields, with either fundamental Gaussian [71, 72] or Laguerre-Gaussian [73] transverse profiles. However, as we show below, the spatial composition of the squeezed field mode is more complex.

In order to investigate the spatial property of the squeezed field, we inserted different radially symmetric spatial masks into the collimated beam after the Rb cell [shown in Fig.2.3(a)]. We classify the beam masks as irises or disks, depending on whether they block the outer or inner part of the laser beam. We used an adjustable iris, and a set of fixed sized disks. These masks were inserted into the collimated part of the laser beam after the interaction with the atoms, making sure that the masks are properly centered. Since the masks reduced the LO power, we carefully recalibrated the shot-noise level for every mask and adjusted the

phase retarding plate to track the maximally squeezed and anti-squeezed quadrature noises.

The modifications of the quantum noise by different types of masks are presented in Fig. 2.3. Based on a single-mode description of the optical field, one would expect the changes in the detected quantum noise in all cases to depend only on the total optical transmission T, and to be accurately described by the beam-splitter expression:

$$SqV_{\rm out} = 10 \cdot \log_{10}[\mathrm{T} \cdot 10^{\mathrm{SqV_{in}}/10} + (1 - \mathrm{T})], \tag{2.1}$$

where $SqV_{\rm in,out}$ are the quadrature noise measured in dB before and after the mask. Clearly, the experimentally measured noise values deviate significantly from the expected dependencies; shown in Figs. 2.3(a)–2.3(d) as dashed and dotted lines, indicating non-trivial spatial correlations [**?**]. For example, even small losses of about 10% (for the iris mask) and 30% (for

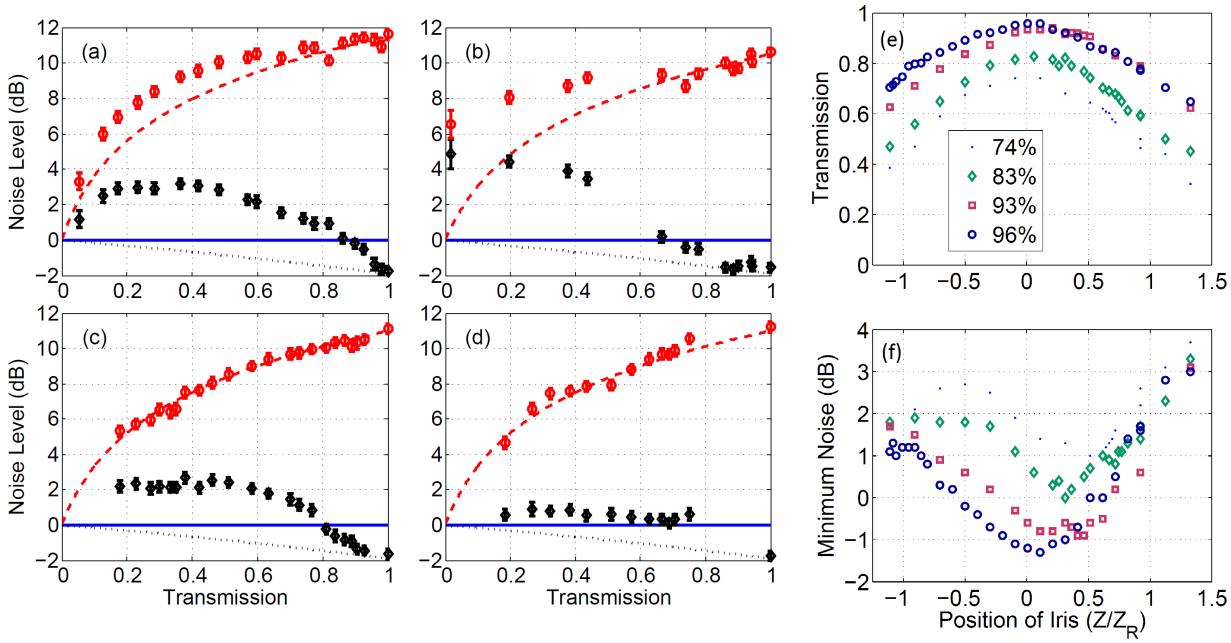

Figure 2.3. The minimum (diamonds) and maximum (circles) quadrature noise detected when the beam is partially blocked by different masks: (a) an iris, (b) a disk, and (c,d) both an iris and a disk. The noise level is plotted vs. the fraction of LO intensity transmitted through the mask. The central disk alone blocked (c) 8% and (d) 25% of the LO intensity. The dashed and dotted lines are predictions based on a single-mode model, and zero of the vertical axis corresponds to the shot noise.

the disk mask) bring the squeezed quadrature noise significantly above shot noise. Moreover, for the disk mask, even at small transmission ($T < 5\%$), the quantum noise in both quadratures is more than 5 dB above shot noise [see Fig. 2.3(b)]. In contrast, Eq. (2.1) predicts that in all cases we should expect the noise to approach the SQL monotonically from below, never exceeding the shot noise level.

To gain additional insight about the spatial distribution of the squeezed vacuum field, we looked at the noise of a ring-like slice of the laser beam. To do this we constructed a mask consisting of a fixed size opaque disk and a variable size iris. Figures 2.3(c) and 2.3(d) represent modifications of transmitted quantum noise by such masks where the fixed disk sizes are characterized by 8% and 25% blockage of LO power. Again, Figures 2.3(c) and 2.3(d) show that we were not able to improve the measured noise suppression below that of the unobstructed beam, even though the anti-squeezing noise followed the uniform loss model much better. Perhaps, such combined masks were able to block especially noisy spatial modes. The above observations suggested that the generated squeezed field consists of several spatial modes, some of which are "noisier" than others. These modes are expected to be radially symmetric due to the cylindrical symmetry of our setup. Furthermore, because of the conservation of angular momentum, we expected that only modes with $\ell = 0$ can be excited via the PSR process.

The portion $\exp[i(2p + |\ell| + 1)\arctan(z/z_R)]$ of the general LG mode [Eq. (1.11)] is known as the Gouy phase. It is responsible for a π phase shift near the beam focus, but this shift is altered by the LG parameters ℓ and p. Therefore, if a superposition of LG modes is propagating through a focus, we can expect interference effects to modify the intensity profile of the beam. If our LO and squeezed field do in fact have a mixed LG structure, then we should observe asymmetries about such a focal point; otherwise, the beam will have a simple Gaussian profile on both sides of the focus. Therefore, we built a one-to-one telescope to create an extra focal point and displaced the iris mask down the telescope to investigate the LG structure. The modified setup is depicted in Fig. 2.2(b) and the results

are plotted in Figs. 2.3(e) and 2.3(f). Qualitatively, the transmission of the LO [Fig. 2.3(e)] is quite symmetric. Therefore, it seems that the LO retains a majority of the Gaussian-mode structure of the pump. However, it is noteworthy that the position of the maximum transmission shifted as we varied the iris size, thus evident of some underlying multi-mode structure. On the other hand, the minimum noise data in Fig. 2.3(f) has very pronounced asymmetry. Furthermore, the irises with 93% and 86% peak transmission, there are more than one local minima. This suggests that the squeezed vacuum field has a significant TSM structure, and the Gouy phase of each mode of the modes in the superposition create this peculiar dependence on the iris position with respect to the focal point. At this stage we developed the hypothesis that the Gouy phase of each mode must be closely related to the squeezing angle of each mode. This idea will be developed formally in Section 4.2.

2.3 Optical Depth Investigation

Next, we investigated the optical depth dependence of PSR squeezing using two methods for changing the optical depth: by changing the interaction length within the atomic medium and changing the atomic density of medium. Specifically, we compared the maximum amount of squeezing possible when the light passes through the vapor cell once, or multiple times, at different atomic densities. We also used a double cell configuration which allowed us to independently vary the atomic density and the relative position of each cell. In addition, it was possible to insert the PBS after the first cell, effectively removing any quantum noise modifications, but preserving any changes to the pump field. In this way, the first cell can be used as a mode-filter, or mode-prep, to modify the pump beam in an advantageous way.

2.3.1 Multi-pass Configuration

To establish the double-pass setup, we placed a mirror after the output collimating lens to back reflect the beam into the cell, as shown in Fig. 2.4(b). The four-pass setup, shown in Fig. 2.4(c), is achieved by adding another retroreflecting mirror before the first lens, once more doubling the optical pass of the beam through the cell.

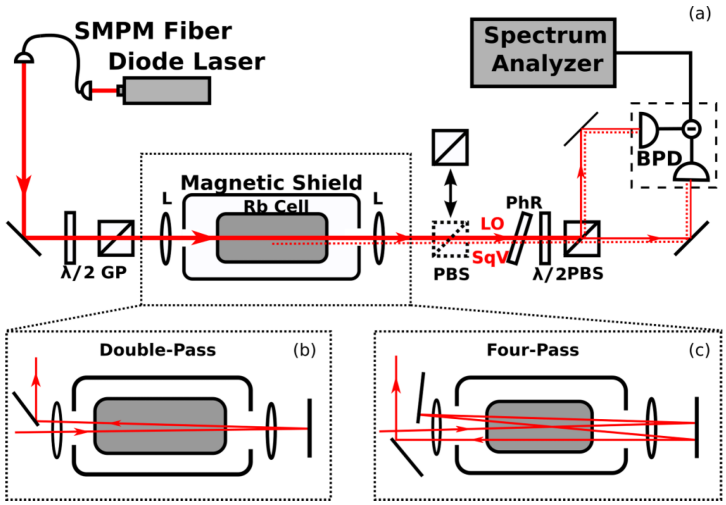

Figure 2.4. Detailed diagram of the (a) PSR squeezer experimental apparatus which has been modified with a (b) double-pass and (c) four-pass beam arrangement. All abbreviations are the same as Fig. 2.2.

We carried out a comparison of the squeezing level in three cases: single, double, and quadruple pass. Since previous studies found that the best squeezing required careful optimization of both atomic density and pump laser power, we carefully mapped the measured minimum quantum noise as a function of both parameters for each experimental arrangement. Fortunately, the highest beam power (11 mW) yielded the best squeezing for each configuration. This conveniently allowed us to fix the laser power for the further measurements, and to confidently compare the squeezing measurements performed at different atomic densities. In the case of a single pass, the best value of squeezing measured was 2.0 dB at the Rb density of $N_{\rm sngl}^{\rm opt} = 9.3 \times 10^{11}{\rm cm}^{-3}$. When the optical path was doubled, a squeezing level of 2.6 dB was achieved at the atomic density $N_{\rm dbl}^{\rm opt} = 4.3 \times 10^{11}{\rm cm}^{-3}$, showing a substantial improvement over the single-pass case. For the quadruple-pass setup we saw a slight decrease in the measured squeezing amount to 2.2 dB at $2.4 \times 10^{11}{\rm cm}^{-3}$. However, in this configuration we did not have full beam-shape control, and thus the expansion of the laser beam on the subsequent passes may have led to the lower observed squeezing.

To elucidate the different outcomes, in Fig. 2.5 we plot the measured squeezing as a function of the effective optical depth, defined as $d = \sigma_0 NL$, where $\sigma_0 = 10^{-9}{\rm cm}^2$ is the

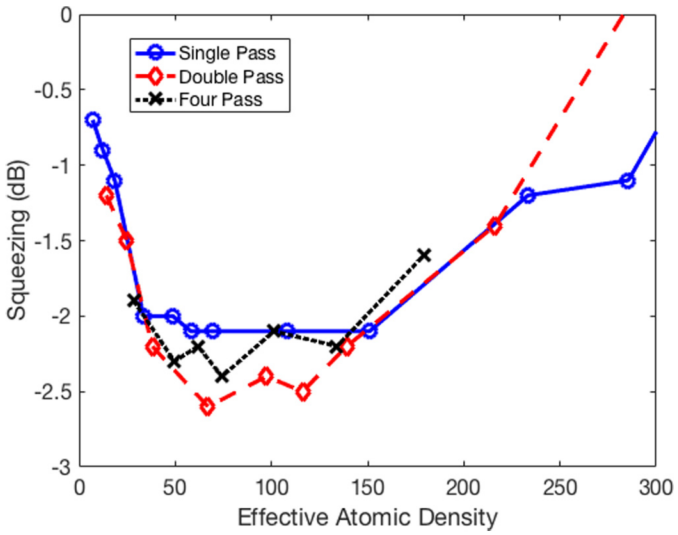

Figure 2.5. The measured dependence of minimum quadrature noise on the effective optical depth for single-, double-, and quadruple-pass configurations. The laser pump power for all three traces was 11 mW, which provided the best value of squeezing for all three geometries.

resonant absorption cross section, N is the atomic number density, and L is the effective length of the atomic medium. If the nonlinear interaction, leading to vacuum squeezing generation, depended only on the integrated optical depth of the ensemble, one could naively expect that all three curves would appear on top of each other. Indeed, there are several clear similarities between the three curves. The overall trends agree quite well. In the low-density limit, the measured squeezing improved with optical depth, reaching a rather broad plateau. However, further increase in atomic density resulted in rapid deterioration of squeezing. In each configuration the best squeezing occurred at approximately the same optical depth range. The main difference between the three geometries appeared in the squeezing magnitudes reached in each case. The single-pass configuration showed the worst quantum noise suppression (2.0 dB) and the double-pass showing the best (2.6 dB). In Chapter 4, this difference is explained by analyzing the dependence of higher-order TSM generation during the light-atom interaction.

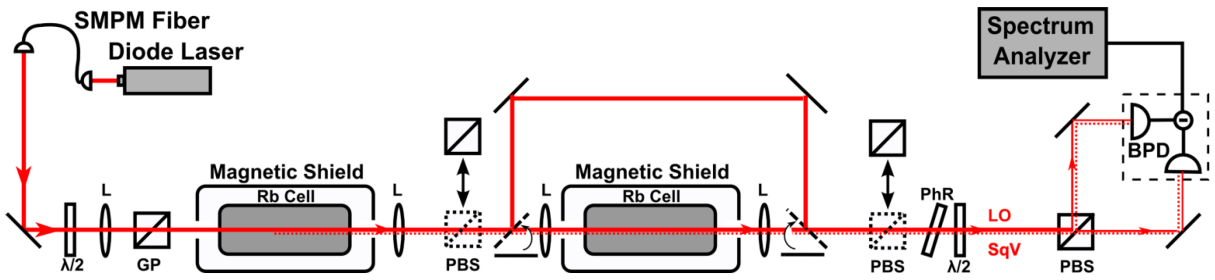

Figure 2.6. Experimental setup modified to include two independent vapor cells. This setup allows the investigation of minimum noise dependence as it relates to the atomic density of the two cells, and the position of the cells with respect to the focal point of the beams. All abbreviations are the same as Fig. 2.2.

2.3.2 Double-Cell Configuration

Continuing the investigation, we added another identical Rb cell to create an "unfolded" double-pass configuration, shown in Fig. 2.6. This configuration allows us to avoid some of the limitations of the previous setup, for example, the inability to independently control the relative position of the beam focus during each pass. The use of two different vapor cells also allowed us to independently vary their atom density and relative positions. In addition, it was possible to insert the polarizing beam splitter after the first cell, effectively removing the quantum noise modifications, but preserving any changes in the intensity distribution of the pump field resulting from the interaction with atoms in the first Rb cell. Consequently, for all the experimental parameters we performed two sets of measurements. First, the pump and the vacuum fields propagated through both cells unaltered. Second, the vacuum fluctuations modified by the first cell were ejected and replaced with a coherent vacuum. In the second case, the measured squeezing was influenced only by the modification of the pump beam in the first cell, thus utilizing the first cell solely for mode preparation.

Since it was possible to change the temperature of each cell independently, we studied the effect of changing atomic density in the second cell when the first-cell atom density was fixed at either $N_{\mathrm{sngl}}^{\mathrm{opt}} = 9.3 \times 10^{11}\mathrm{cm}^{-3}$, the optimal condition for the single-pass squeezing generation, or $N_{\mathrm{dbl}}^{\mathrm{opt}} = 4.3 \times 10^{11}\mathrm{cm}^{-3}$, at which the highest value of the measured squeezing

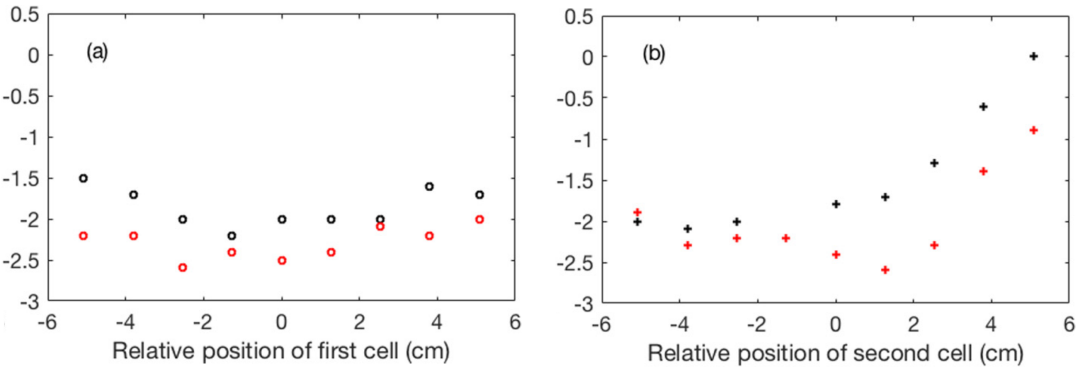

Figure 2.7. Dependence of squeezing on the position of the (a) first cell and (b) second cell. Red data gives the measured squeezing when the squeezed field generated in the first cell is filtered out before the second cell. Black data gives the measured squeezing when both cells are used with no filtering. In each case, when a cell is held fixed, it is held at its optimal position. The atomic density in both cells is $9.3 \times 10^{11}\text{cm}^{-3}$, in (a) the second cell is held at 1.3 cm, and in (b) the first cell is held at -2.5 cm.

in the double-pass configuration was observed. In all cases there exists again an optimal atomic-density at which the measured squeezing is maximized. If the squeezed vacuum propagates through both cells (crosses), we unsurprisingly observed the best squeezing when both cells were at the same atomic density, $N_{\text{dbl}}^{\text{opt}} = 4.3 \times 10^{11}\text{cm}^{-3}$, replicating the optimal conditions observed for the double-pass experiment. When the first cell was tuned to the optimal single-pass condition, the best squeezing was measured when the atomic density of the second cell was set slightly higher. However, there was no further improvements compared to the output of the single cell.

We also observed that if the squeezed vacuum field generated in the first cell was filtered out by the polarizing BS, the measured amount of squeezing after the second cell (2.8 dB) exceeded the best squeezing for the previous configurations. This observation implies that the pump modifications due to the interaction with the first cell resulted in more favorable conditions for generation of squeezed vacuum in the second cell. This shows us that it may be possible to further improve squeezing by actively optimizing the spatial mode decomposition of the pump field. Our experimental results also displayed strong dependence on the observed amount of squeezing to the relative position of the cells and the focal points of the optical

beams. Such behavior agrees with our previous observations that the exact decomposition of the higher-order TSM's is sensitive to the geometry of the interaction and changes depending on where in the cell the pump beam is focused. By translating each cell on the beam axis, we changed the position of the beam focus in each cell. We define the relative position of each cell such that for zero displacement, the focus of the pump beam is at the geometrical center of the cell. Furthermore, a positive displacement indicates that the focus is before the center of the cell. For example, the displacement of +2.5 cm means that the focal point is approximately 1.25 cm away from the front window, and 6.25 cm from the rear window of our 7.5-cm cell.

In Figure 2.7 we plot the dependence of squeezing on the relative position of the two cells. The atomic density in both cells is held at $9.3 \times 10^{11}\text{cm}^{-3}$. In Figure 2.7(a) the second cell is held at 1.3 cm while the first cell is translated, and in Fig. 2.7(b) the first cell is held at -2.5 cm while the second cell is translated. The black data is the minimum squeezing when no filtering was used between the two cells. The red data is the minimum squeezing when the vacuum fluctuations, which were modified by the first cell, are reflected and replaced with coherent vacuum. It is quite amazing that the second scenario almost always out performs the first. This is clear evidence of the TSM structure of the LO and squeezed field, once again demanding a more complete understanding of the multimode interaction. Furthermore, we see that the focal position in each cell can have significant impacts on the squeezing performance. It is clear that to maximize the output squeezing, the focus in each consecutive cell must be carefully optimized for each value of atomic density, and deviating from this optimal position can quickly deteriorate the output squeezing. This observation can partly explain why we did not see improved squeezing when we increased the number of passes from two to four in the previous experiment, since no independent focal position optimization was possible for each pass.

This Chapter has outlined the clear evidence we discovered in our investigation of the TSM properties of quadrature squeezing generated via PSR. In the following Chapter, we will

develop the theoretical tools necessary to begin to simulate this, and many other, nonlinear interaction. In Chapter 4, we will revisit PSR squeezing, and use our theory to model our experiment. Furthermore, we will show how to make predictions about the squeezing that is achieved, and how it is distributed among the TSMs.

3 Beam Theory

3.1 Classical Beam Theory for Nonlinear Optics

In this section, we present our solution to the inhomogeneous parxial wave equation developed in Section 1.2.1. To that end, we will discuss our use of the Born approximation, some significant properties of the Laguerre-Gauss modes, and then give an overview our method using Green's functions. Although this method makes use of some approximations, we will discuss how this approach is superior to numerical methods for our problems. An analytic method is preferred, because we wish to explicitly retain the mode structure of the resulting beam, such that we may use it to perform a second-quantization procedure, which follows in the next section. Please see Appendix A for full details of our Green's function solution method.

3.1.1 Spatial Mode Propagation

To proceed in solving the inhomogeneous paraxial wave equation, Eq. (1.18), we pause to recognize the symmetry with the nonlinear Schrödinger equation. With this similarity in mind, we make a first-order Born approximation [74], and replace $\boldsymbol{\mathcal{E}}$ with the input beam $\boldsymbol{\mathcal{E}}_0$ instead, which establishes a much simpler differential equation of the form,

$$(\frac{\partial}{\partial z} - \frac{i}{2k}\nabla_\perp^2)\boldsymbol{\mathcal{E}} = \frac{ik}{2\epsilon_0}\boldsymbol{\mathcal{P}}(\boldsymbol{\mathcal{E}}_0) \equiv \wp(\boldsymbol{\mathcal{E}}_0). \tag{3.1}$$

The first Born approximation was conceived for matter waves in the nonlinear Schrödinger equation with weak scattering potentials and small incident angles, but it is relevant to our nonlinear optical problem as well. Analogously, the nonlinearities are relatively weak and the incident angles are also small. Furthermore, our pump beams are strong *and* typically only slightly modified by the nonlinearity. As we pointed out in Section 1.3, most of the interactions of interest in quantum optics do not require the full tensor nature of the sus-

ceptibility, allowing us to decouple the inhomogeneous paraxial wave equation. Lastly, most nonlinear processes that involve the generation of new fields start with vacuum modes, thus the nonlinear medium is truly behaving like a source, as Eq. (3.1) describes. For example, as we have seen in the PSR squeezing scheme, the y-polarized pump beam is the source of new TSM structure in the x polarization, which began as vacuum entering the empty x-polarized port. Thus, the Born approximation accurately describes the actual physical process. That is, the optical response of the nonlinear material inherent in $\wp(\boldsymbol{\mathcal{E}}_0)$ behaves as a source for new mode components of the field.

3.1.2 Construction of the initial-value-problem

Seeing that the right-hand-side of Eq. (3.1) is effectively the source of the new beam, it is helpful to restate the problem here as an initial-value problem (IVP) in the compact form,

$$\begin{aligned} \text{DE}: \ & \hat{L}\mathcal{E} = \wp(\mathcal{E}_0) \\ \text{IV}: \ & \mathcal{E}_0, \end{aligned} \tag{3.2}$$

where $\hat{L} \equiv \frac{\partial}{\partial z} - \frac{i}{2k}\nabla_\perp^2$ and $\mathcal{E}_0$ is the input-field which is assumed to be undepleted. Although this IVP represents a first Born approximation, the following method can be used iteratively for cases when the nonlinearity and generated fields are stronger. In such cases, it may be necessary to include an attenuation factor, on the initial value, which conserves energy. Ideally, the theory does not require any free parameters for the source $\wp$, and can be used directly. In reality, however, it may be difficult to calculate the strength of the source if the model used does not capture the full complexity of the experimental system. Therefore, it may be convenient to capture such complexity with an interaction strength factor that, if necessary, can be used as a fitting parameter. For example, a fitting parameter is quite useful when simulating the generation of squeezed light in hot atomic vapor, where the direct calculations are too complex. In Chapter 4 we will use a fitting parameter to model the slight changes to the LO, effectively finding the relative strength of the nonlinearity [see Eq. (4.6)].

3.1.3 Laguerre-Gauss Mode Properties

In Section 1.2.1 we derived the paraxial wave equation and introduced the LG modes, which are solutions in cylindrical coordinates. Now, we will continue discussing some of their properties, which are critical to our solution method. The LG modes form a complete orthonormal set, and thus can be used as a basis set to expand an arbitrary paraxial beam $B = B(r, \phi, z)$ in free space. Using the orthogonality relation

$$\int r dr d\phi \, u^*_{\ell,p}(r, \phi, z) u_{q,n}(r, \phi, z) = \delta_{\ell q} \delta_{pn}, \tag{3.3}$$

we can write $B(r, \phi, z)$ as

$$B(r, \phi, z) = \sum_{\ell,p} c_{\ell,p}(w_0) u_{\ell,p}(r, \phi, z, w_0), \tag{3.4}$$

where

$$c_{\ell,p}(w_0) = \int r dr d\phi \, u^*_{\ell,p}(r, \phi, z_0, w_0) B(r, \phi, z_0). \tag{3.5}$$

The waist w_0 of the basis set is, in general, chosen to give the best fit and reduce the number of terms in the expansion, whereas the $c_{\ell,p}$ coefficients are independent of the position z_0. If we insert Eq. (3.5) in Eq. (3.4) and collect the LG modes we find

$$\begin{aligned} B(r, \phi, z) = &\int r' dr' d\phi' \, B(r', \phi', z_0) \\ &* \Big(\sum_{\ell,p} u^*_{\ell,p}(r', \phi', z_0) u_{\ell,p}(r, \phi, z) \Big). \end{aligned} \tag{3.6}$$

If we impose $z = z_0$, then we can establish the very important completeness relation:

$$\sum_{\ell,p} u^*_{\ell,p}(r', \phi', z) u_{\ell,p}(r, \phi, z) = \delta(r - r') \delta(\phi - \phi'). \tag{3.7}$$

The condition $z = z_0$ simply states that the LG modes are complete at equal z's, i.e, when the two z slices coincide. Furthermore, we will see that this condition reemerges as part of the mechanism which introduces the input beam in the solution of the IVP. Thus, the completeness relation is instrumental in the Green's function solution method, which we will now present briefly.

3.1.4 Green's Function Solution — Mode Structure of Generated Beam

The magic of the Green's function solution method [75] is that once the propagator K, and Green's function G are derived, the problem is solved (for full details of the solution method see Appendix A):

$$\begin{aligned}\mathcal{E} = &\int r'dr'd\phi'\, K(\mathbf{r}\,|\,\mathbf{r}')\mathcal{E}_0(\mathbf{r}')\;|_{z=z'} \\ &+ \int dz' \int r'dr'd\phi'\, G(\mathbf{r}\,|\,\mathbf{r}')\wp(\mathbf{r}').\end{aligned} \tag{3.8}$$

Although we solve this problem in free space, the properties of the LG modes allow us to utilize a method developed for fixed boundary conditions. Since the LG modes are a complete orthonormal set, we can use an eigenfunction expansion. Recalling the completeness relation in Eq. (3.7), we define the propagator and Green's function in terms of the LG modes:

$$\begin{aligned}K(r,\phi,z|r',\phi',z') &\equiv \sum_{\ell,p} u^*_{\ell,p}(r',\phi',z')u_{\ell,p}(r,\phi,z) \\ G(r,\phi,z|r',\phi',z') &\equiv \Theta(z-z')K(r,\phi,z|r',\phi',z'),\end{aligned} \tag{3.9}$$

where $\Theta(z-z')$ is the Heaviside step function.

At this point the problem is solved. However, we may further simplify matters by expanding the source $\wp$ in terms of the LG modes:

$$\wp(r,\phi,z) = \sum_{\ell,p} c_{\ell,p}(z)\, u_{\ell,p}(r,\phi,z), \tag{3.10}$$

where $c_{\ell,p}(z) = \int r dr d\phi \, u^*_{\ell,p}(r,\phi,z)\wp(r,\phi,z)$. To find the final form of our solution, we insert Eq. (3.9) and Eq. (3.10) into Eq. (3.8) and find

$$\mathcal{E}(\mathbf{r}) = \mathcal{E}_0(\mathbf{r}) + \sum_{\ell,p} u_{\ell,p}(\mathbf{r}) \int_{z_i}^{z_f} dz' c_{\ell,p}(z'). \tag{3.11}$$

So we see that the final solution is a superposition of the unmodified pump beam, and a collection of LG modes, which, referring to Eq. (3.1), will depend on the specified polarization $\mathcal{P}$ and the spatial structure of the input beam $\mathcal{E}_0$. The cautious reader may be concerned that we have solved a problem concerning a possibly localized source distribution using a free space Green's function method. Therefore, we point out that the effects of the source are totally subsumed in the spacial distribution of $\wp$. Furthermore, in most situations a Gaussian pump beam will be completely encompassed by the interaction region, effectively making the boundary in r infinite.

Thus, we have developed a general solution to the inhomogeneous paraxial wave equation, but we have not been explicit with the phase matching conditions or the interaction between the mode components of the field. A more careful treatment is due for each particular implementation. In Chapter 4 we will use this theory to explain the PSR experiment discussed in Chapter 2. Later, in Chapter 5, we will demonstrate how to use the theory to simulate beam dynamics in OAM transfer interactions.

3.2 Quantum Beam Theory for Nonlinear Optics

In Section 1.4 we introduced some of the framework of quantum optics. One should recall the two main ingredients in the recipe: first find the mode structure, then quantize the modes. Sometimes, the quantization procedure is referred to as "second quantization" because, in many ways, finding the mode structure of the classical field is the first quantization. Take, for example, the LG modes, which we have discussed in detail. Even in free space they form a complete and orthonormal set of modes, indexed by the azimuthal and radial

induces. It is this property that allows an eigenfunction-like expansion of the propagator in the Green's function solution method. Thus, now that the modes have been identified, it is time to quantize the modes. We will take a relatively simple approach, jump straight to the interaction picture, and analyze a general phenomenological Hamiltonian that is relevant to PDC and FWM interactions.

3.2.1 Hamiltonian and Unitary Evolution

Any third-order nonlinear interaction can be described in terms of the quantum fields $\hat{E}$ by a Hamiltonian of the form

$$H \propto \int d\mathbf{r}^3 \chi^{(3)}(\mathbf{r}) \left(\hat{E}_{d1}^{(-)}(\mathbf{r},t)\, \hat{E}_{d2}^{(-)}(\mathbf{r},t) \times \hat{E}_{s}^{(+)}(\mathbf{r},t)\, \hat{E}_{i}^{(+)}(\mathbf{r},t) - \text{H.c.} \right), \tag{3.12}$$

where $\chi^{(3)}(\mathbf{r})$ is the third-order nonlinearity, $\hat{E}^{(\pm)}$ corresponds to the positive and negative frequency components of the field, and $d1, d2, s, i$ correspond to drive (pump), signal and idler fields. We follow tradition in labeling the non-driving modes signal and idler (also referred to as target modes in literature). We elect to consider input beams with cylindrical symmetry, but we note that the following calculation can certainly be done in other coordinate systems. As was discussed in Section 1.2.1, the homogeneous paraxial wave equation gives rise to the LG family of solutions (Eq. 1.11) when solved in cylindrical coordinates.

To retain generality, we will assume that the pump beam modes are known but that the signal and idler modes have vacuum inputs. Therefore, we must allow for a large number of spatial modes in the signal and idler fields. Thus, we let

$$\begin{aligned} \hat{E}_{s}^{(+)}(\mathbf{r},t) &= \sum_{\ell,p} u_{\ell,p}(\mathbf{r})\, \hat{a}_{\ell,p}\, e^{i(\mathbf{k}_s \cdot \mathbf{r} - \omega_s t)} \\ \hat{E}_{i}^{(+)}(\mathbf{r},t) &= \sum_{m,q} u_{m,q}(\mathbf{r})\, \hat{b}_{m,q}\, e^{i(\mathbf{k}_i \cdot \mathbf{r} - \omega_i t)}. \end{aligned} \tag{3.13}$$

In reality, an infinite number of modes is not necessary and the sum can be truncated to a total of N modes. To determine the mode structure relevant to the interaction, one can use the semiclassical-beam theory developed in the previous section. Furthermore, if a vacuum mode is replaced with a seed beam, then the semiclassical theory can predict the beam evolution, which can be included here. The pump beams, on the other hand, are treated classically and have a well-known structure, and without loss of generality, we can choose them to be Gaussian beams of the form

$$\begin{aligned}\hat{E}_{d1}^{(+)}(\mathbf{r},t) &= A_{d1}\, u_{0,0}(\mathbf{r})\, \hat{d}_1\, e^{i(\mathbf{k}_{d1}\cdot\mathbf{r}-\omega_{d1}t)} \\ \hat{E}_{d2}^{(+)}(\mathbf{r},t) &= A_{d2}\, u_{0,0}(\mathbf{r})\, \hat{d}_2\, e^{i(\mathbf{k}_{d2}\cdot\mathbf{r}-\omega_{d2}t)},\end{aligned} \tag{3.14}$$

where A_{d1} and A_{d2} are complex amplitudes. In practice, one can plug in whatever mode structure is present in the pump beam(s). Next, we make the parametric approximation and drop the operator character of the pump fields, transforming Eq. (3.12) into

$$\hat{H} = \kappa \int d\mathbf{r}^3 \sum_{\ell p m q} \left(\chi^{(3)*}_{\ell,p;m,q} \hat{a}_{\ell,p}\, \hat{b}_{m,q} - \chi^{(3)}_{\ell,p;m,q} \hat{a}^\dagger_{\ell,p}\, \hat{b}^\dagger_{m,q} \right), \tag{3.15}$$

where κ is a coupling constant, the effective susceptibility is

$$\chi^{(3)}_{\ell,p;m,q} \equiv C\, \chi^{(3)}(\mathbf{r})\, A_{d1} A_{d2}\, u^2_{0,0}(\mathbf{r})\, u^*_{\ell,p}(\mathbf{r})\, u^*_{m,q}(\mathbf{r}), \tag{3.16}$$

C is a normalization constant, and we have assumed phase matching, which allows us to drop the exponential factor.

Next, we will simplify notation and make calculations more straightforward by turning the double sum in Eq. (3.15) into matrix multiplication. First, we will recognize that, in practice, the summation over the modes can be truncated. To simplify notation, we'll assume there is some $\ell_{\max} = m_{\max}$, and the sums run symmetrically over the azimuthal modes, that is $-\ell_{\max} \le \ell \le \ell_{\max}$ and $-m_{\max} \le m \le m_{\max}$. Likewise, there is some $p_{\max} = q_{\max}$, which

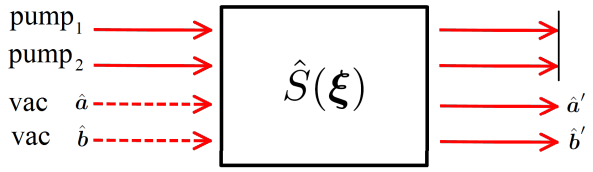

Figure 3.1. General unitary evolution generated in a $\chi^{(3)}$ material. In each spatial mode, there are actually many transverse-spatial modes interacting not only within the mode, but potentially with many other modes in the adjacent spacial modes. Our theory can accommodate single or dual pump modes and single or dual vacuum input modes. Furthermore, a vacuum mode, for example $\hat{\boldsymbol{b}}$, could be replaced with a seed beam and evolution could be calculated with our semi-classical beam theory for nonlinear optics, and incorporated into this second quantization procedure.

determine $0 \leq p \leq p_{\max}$ and $0 \leq q \leq q_{\max}$. Next, we will define the vector of operators

$$\begin{aligned} \hat{\boldsymbol{a}} &\equiv (\hat{a}_{\ell,p}\ \hat{a}_{\ell,p+1}\ ...\ \hat{a}_{\ell+1,p}\ \hat{a}_{\ell+1,p+1}\ ...)^T \\ \hat{\boldsymbol{a}}^\dagger &\equiv (\hat{a}^\dagger_{\ell,p}\ \hat{a}^\dagger_{\ell,p+1}\ ...\ \hat{a}^\dagger_{\ell+1,p}\ \hat{a}^\dagger_{\ell+1,p+1}\ ...)^T, \end{aligned} \tag{3.17}$$

where, in this case, $\ell = -\ell_{\max}$ and $p = 0$ are the lowest order modes in consideration, $(\cdot)^T$ indicates the transpose operation, and $\hat{b}$ follows accordingly. With these vectors in mind, we define a corresponding two-photon amplitude matrix (see Appendix B)

$$\boldsymbol{\chi} \equiv \sum_{\ell p m q} \hat{e}_{\ell+1} \otimes \hat{e}_{p+1}\, \chi_{\ell-\ell_{\max},p;m-m_{\max},q}\, [\hat{e}_{m+1} \otimes \hat{e}_{q+1}]^T, \tag{3.18}$$

where $\hat{e}_i$ is a vector with one in the ith position, and the sum runs over $0 \leq \ell \leq 2\ell_{\max}+1$, $0 \leq p \leq p_{\max}$, $0 \leq m \leq 2m_{\max}+1$, and $0 \leq q \leq q_{\max}$. Using Eq. (3.17) and Eq. (3.18) we can rewrite Eq. (3.15) as

$$\hat{H} = \int d\mathbf{r}^3 \left(\widetilde{\hat{\boldsymbol{b}}}\, \boldsymbol{\chi}^\dagger\, \hat{\boldsymbol{a}} - \widetilde{\hat{\boldsymbol{a}}^\dagger} \boldsymbol{\chi}\, \hat{\boldsymbol{b}}^\dagger \right), \tag{3.19}$$

where we have introduced $\widetilde{(\cdot)}$ to denote the transpose. This Hamiltonian leads to the two mode squeezing operator

$$\hat{S}(\boldsymbol{\xi}) \equiv \exp\left[\widetilde{\hat{\boldsymbol{b}}}\, \boldsymbol{\xi}^\dagger\, \hat{\boldsymbol{a}} - \widetilde{\hat{\boldsymbol{a}}^\dagger} \boldsymbol{\xi}\, \hat{\boldsymbol{b}}^\dagger \right], \tag{3.20}$$

where $\boldsymbol{\xi} \equiv \int d\mathbf{r}^3\, \boldsymbol{\chi}\, t$ is the squeezing matrix. This unitary evolution is depicted in Fig. 3.1.

When $\boldsymbol{\xi}$ is symmetric, the left polar decomposition gives $\boldsymbol{\xi} = \boldsymbol{R}\exp[i\boldsymbol{\Theta}] = \exp[i\widetilde{\boldsymbol{\Theta}}]\widetilde{\boldsymbol{R}}$, where $\boldsymbol{R}$ and $\boldsymbol{\Theta}$ are Hermitian matrices. In general, $\boldsymbol{R}$ and $\boldsymbol{\Theta}$ do not commute. However, it follows that for functions f that are expandable in a power series, $f(\boldsymbol{R})e^{i\boldsymbol{\Theta}} = e^{i\boldsymbol{\Theta}}f(\widetilde{\boldsymbol{R}})$ and $f(\boldsymbol{R})e^{i\boldsymbol{\Theta}} = e^{i\widetilde{\boldsymbol{\Theta}}}f(\widetilde{\boldsymbol{R}})$ where f is even or odd respectively. Straightforward yet tedious repetition of the Baker-Campbell-Hausdorff relation allows us to find the Bogoliubov transformations for the multimode vectors:

$$\begin{aligned}
\hat{S}^\dagger(\boldsymbol{\xi})\,\hat{\boldsymbol{a}}\,\hat{S}(\boldsymbol{\xi}) &= \cosh(\boldsymbol{R})\hat{\boldsymbol{a}} - \sinh(\boldsymbol{R})e^{i\boldsymbol{\Theta}}\hat{\boldsymbol{b}}^\dagger \\
\hat{S}^\dagger(\boldsymbol{\xi})\,\hat{\boldsymbol{b}}\,\hat{S}(\boldsymbol{\xi}) &= \cosh(\boldsymbol{R})\hat{\boldsymbol{b}} - \sinh(\boldsymbol{R})e^{i\boldsymbol{\Theta}}\hat{\boldsymbol{a}}^\dagger \\
\hat{S}^\dagger(\boldsymbol{\xi})\,\hat{\boldsymbol{a}}^\dagger\,\hat{S}(\boldsymbol{\xi}) &= \cosh(\widetilde{\boldsymbol{R}})\hat{\boldsymbol{a}}^\dagger - \sinh(\widetilde{\boldsymbol{R}})e^{-i\widetilde{\boldsymbol{\Theta}}}\hat{\boldsymbol{b}} \\
\hat{S}^\dagger(\boldsymbol{\xi})\,\hat{\boldsymbol{b}}^\dagger\,\hat{S}(\boldsymbol{\xi}) &= \cosh(\widetilde{\boldsymbol{R}})\hat{\boldsymbol{b}}^\dagger - \sinh(\widetilde{\boldsymbol{R}})e^{-i\widetilde{\boldsymbol{\Theta}}}\hat{\boldsymbol{a}},
\end{aligned} \tag{3.21}$$

and their transposes

$$\begin{aligned}
\hat{S}^\dagger(\boldsymbol{\xi})\,\widetilde{\hat{\boldsymbol{a}}}\,\hat{S}(\boldsymbol{\xi}) &= \widetilde{\hat{\boldsymbol{a}}}\cosh(\widetilde{\boldsymbol{R}}) - \widetilde{\hat{\boldsymbol{b}}^\dagger}e^{i\widetilde{\boldsymbol{\Theta}}}\sinh(\widetilde{\boldsymbol{R}}) \\
\hat{S}^\dagger(\boldsymbol{\xi})\,\widetilde{\hat{\boldsymbol{b}}}\,\hat{S}(\boldsymbol{\xi}) &= \widetilde{\hat{\boldsymbol{b}}}\cosh(\widetilde{\boldsymbol{R}}) - \widetilde{\hat{\boldsymbol{a}}^\dagger}e^{i\widetilde{\boldsymbol{\Theta}}}\sinh(\widetilde{\boldsymbol{R}}) \\
\hat{S}^\dagger(\boldsymbol{\xi})\,\widetilde{\hat{\boldsymbol{a}}^\dagger}\,\hat{S}(\boldsymbol{\xi}) &= \widetilde{\hat{\boldsymbol{a}}^\dagger}\cosh(\boldsymbol{R}) - \widetilde{\hat{\boldsymbol{b}}}e^{-i\boldsymbol{\Theta}}\sinh(\boldsymbol{R}) \\
\hat{S}^\dagger(\boldsymbol{\xi})\,\widetilde{\hat{\boldsymbol{b}}^\dagger}\,\hat{S}(\boldsymbol{\xi}) &= \widetilde{\hat{\boldsymbol{b}}^\dagger}\cosh(\boldsymbol{R}) - \widetilde{\hat{\boldsymbol{a}}}e^{-i\boldsymbol{\Theta}}\sinh(\boldsymbol{R}).
\end{aligned} \tag{3.22}$$

With these transformations at our disposal, we can calculate the expectation values of many interesting quantities.

3.2.2 Quadrature Variance

In Section 1.4 we introduced the quadrature operators and discussed how their variances reveal information about the noise of the state of light. In this section, we investigate the "twin beam" labeled by the operators $\hat{a}$ and $\hat{b}$, which was initially a product state $|\mathbf{0}\rangle = |\{0\}_{l,p}\rangle_a \bigotimes |\{0\}_{m,q}\rangle_b$. However, after the nonlinearity, it is potentially an entangled

state since photons were created pairwise in the $\hat{a}$ and $\hat{b}$ modes, that is, it is not possible to find pure states $|\psi\rangle_a$ and $|\phi\rangle_b$ such that $\hat{S}(\boldsymbol{\xi})|\mathbf{0}\rangle = |\psi\rangle_a \bigotimes |\phi\rangle_b$. Therefore, we will investigate the variances of the joint quadrature operators, which we define as

$$\begin{aligned}\hat{\boldsymbol{X}}_1 =& \frac{1}{2^{3/2}}(\hat{\boldsymbol{a}} + \hat{\boldsymbol{a}}^\dagger + \hat{\boldsymbol{b}} + \hat{\boldsymbol{b}}^\dagger) \\ \hat{\boldsymbol{X}}_2 =& \frac{1}{i2^{3/2}}(\hat{\boldsymbol{a}} - \hat{\boldsymbol{a}}^\dagger + \hat{\boldsymbol{b}} - \hat{\boldsymbol{b}}^\dagger).\end{aligned} \tag{3.23}$$

Scalar Variance

We first investigate the scalar variance of the transverse multispatial-mode field. The scalar quadrature variance is defined as

$$\langle(\Delta\hat{X}_j)^2\rangle \equiv \langle\Delta\widetilde{\hat{\boldsymbol{X}}}_j\, \Delta\hat{\boldsymbol{X}}_j\rangle, \tag{3.24}$$

where $\Delta\hat{\boldsymbol{X}}_j \equiv \hat{\boldsymbol{X}}_j - \langle\hat{\boldsymbol{X}}_j\rangle$. In the spontaneous nonlinear interaction regime, that is, vacuum in the signal and idler input modes, we are assured that $\langle\hat{\boldsymbol{X}}_j\rangle = \mathbf{0}$ and we thus find

$$\langle(\Delta\hat{X}_j)^2\rangle = \langle\widetilde{\hat{\boldsymbol{X}}}_j\, \hat{\boldsymbol{X}}_j\rangle = \langle\{0\}_B, \{0\}_A|\hat{S}^\dagger\widetilde{\hat{\boldsymbol{X}}}_j\hat{S}\, \hat{S}^\dagger\hat{\boldsymbol{X}}_j\hat{S}|\{0\}_A, \{0\}_B\rangle, \tag{3.25}$$

where $|\{0\}_A, \{0\}_B\rangle$ is the vacuum state for the multimode twin beam, and $|\{0\}\rangle = |0_1, 0_2, ...\rangle$ is the typical multimode vacuum state. The list of modes in $|\{0\}\rangle$ naturally follow the same pattern as the vector of operators in Eq.(3.17). Using Eqs. (3.21)–(3.23) in Eq. (3.25) we find

$$\begin{aligned}\langle(\Delta\hat{X}_{1,2})^2\rangle &= \frac{1}{4}\mathrm{Tr}\big\{\cosh^2(\widetilde{\boldsymbol{R}}) + \sinh^2(\boldsymbol{R}) \\ &\quad \mp \big(\cosh(\widetilde{\boldsymbol{R}})\sinh(\boldsymbol{R})e^{i\boldsymbol{\Theta}} + \sinh(\boldsymbol{R})\cosh(\widetilde{\boldsymbol{R}})e^{-i\boldsymbol{\Theta}}\big)\big\} \\ &= \frac{1}{4}\mathrm{Tr}\big\{\cosh^2(\boldsymbol{R}) + \sinh^2(\boldsymbol{R}) \mp 2\sinh(\boldsymbol{R})\cosh(\boldsymbol{R})\cos(\boldsymbol{\Theta})\big\} \\ &= \frac{1}{4}\mathrm{Tr}\big\{\cosh(2\boldsymbol{R}) \mp \sinh(2\boldsymbol{R})\cos(\boldsymbol{\Theta})\big\},\end{aligned} \tag{3.26}$$

where in the second line we use the cyclicity of trace, the invariance under transpose, and the commutation properties of $\boldsymbol{R}$ and $\boldsymbol{\Theta}$ to find a familiar form, and in the final line present a compact form. Therefore, we see that the total quadrature variance is simply the sum of all the quadrature variances in each of the TSM's.

Variance Matrices

Next, we investigate the corresponding variance-covariance matrices:

$$\langle(\Delta\hat{\boldsymbol{X}}_j)^2\rangle \equiv \langle\Delta\hat{\boldsymbol{X}}_j\,\Delta\widetilde{\hat{\boldsymbol{X}}}_j\rangle = \langle\hat{\boldsymbol{X}}_j\,\widetilde{\hat{\boldsymbol{X}}}_j\rangle, \tag{3.27}$$

where again we have assumed $\langle\hat{\boldsymbol{X}}_j\rangle = 0$. Using Eqs. (3.21-3.23) in Eq. (3.27) we find

$$\langle(\Delta\hat{\boldsymbol{X}}_{1,2})^2\rangle = \frac{1}{8}\big[\cosh(2\boldsymbol{R}) + \cosh(2\widetilde{\boldsymbol{R}}) \mp \big(\sinh(2\boldsymbol{R})e^{i\boldsymbol{\Theta}} + \sinh(2\widetilde{\boldsymbol{R}})e^{-i\widetilde{\boldsymbol{\Theta}}}\big)\big]. \tag{3.28}$$

To investigate the correlations between $\hat{\boldsymbol{X}}_1$ and $\hat{\boldsymbol{X}}_2$ we calculate the cross-covariance matrix

$$\begin{aligned}\mathbf{cov}(\hat{\boldsymbol{X}}_1,\,\hat{\boldsymbol{X}}_2) &\equiv \frac{1}{2}\big(\langle\hat{\boldsymbol{X}}_1\,\widetilde{\hat{\boldsymbol{X}}}_2\rangle + \langle\hat{\boldsymbol{X}}_2\,\widetilde{\hat{\boldsymbol{X}}}_1\rangle^T\big)\\ &= \frac{i}{4}\big[\cosh 2\boldsymbol{R} - \cosh 2\widetilde{\boldsymbol{R}} + \sinh(2\boldsymbol{R})e^{i\boldsymbol{\Theta}} - \sinh(2\widetilde{\boldsymbol{R}})e^{-i\widetilde{\boldsymbol{\Theta}}}\big],\end{aligned} \tag{3.29}$$

which happens to equalize the general uncertainty relation

$$\langle(\Delta\hat{\boldsymbol{X}}_1)^2\rangle\,\langle(\Delta\hat{\boldsymbol{X}}_2)^2\rangle \geq \frac{1}{4}\big(\mathbf{cov}(\hat{\boldsymbol{X}}_1,\,\hat{\boldsymbol{X}}_2)\big)^2 + \frac{\boldsymbol{I}}{16}. \tag{3.30}$$

When the squeeze matrix is symmetric *and* Hermitian, it has real entries. Therefore, when $\boldsymbol{\xi} = \widetilde{\boldsymbol{\xi}}$ and $\boldsymbol{\xi} = \boldsymbol{\xi}^\dagger \implies \boldsymbol{R} = \widetilde{\boldsymbol{R}}$ and $e^{i\boldsymbol{\Theta}} = e^{-i\widetilde{\boldsymbol{\Theta}}}$. This reduces the variances to

$$\begin{aligned}\mathrm{cov}(\hat{\boldsymbol{X}}_1,\,\hat{\boldsymbol{X}}_2) &= 0\\ \langle(\Delta\hat{\boldsymbol{X}}_1)^2\rangle\,\langle(\Delta\hat{\boldsymbol{X}}_2)^2\rangle &= \frac{I}{16}.\end{aligned} \tag{3.31}$$

Furthermore, when $\boldsymbol{\xi}$ is positive semidefinite we have $e^{i\boldsymbol{\Theta}} = I$, and Eq. (3.28) reduces to the simple form

$$\langle (\Delta \hat{\boldsymbol{X}}_{1,2})^2 \rangle = \frac{1}{4} e^{\mp 2\boldsymbol{R}}. \tag{3.32}$$

3.2.3 Photons and Multimode Correlations

Now, we will investigate the average photon number of the squeezed state $|\xi\rangle$ and the correlations. We find

$$\begin{aligned}
\langle \hat{n}_a \rangle &= \langle \xi | \hat{\tilde{\boldsymbol{a}}}^\dagger \hat{\boldsymbol{a}} | \xi \rangle = \mathrm{Tr}\{\sinh^2(\boldsymbol{R})\} \\
\langle \hat{n}_b \rangle &= \langle \xi | \hat{\tilde{\boldsymbol{b}}}^\dagger \hat{\boldsymbol{b}} | \xi \rangle = \mathrm{Tr}\{\sinh^2(\boldsymbol{R})\} \\
\langle \hat{n}_a^2 \rangle &= \langle \xi | (\hat{\tilde{\boldsymbol{a}}}^\dagger \hat{\boldsymbol{a}})^2 | \xi \rangle = \frac{1}{4}\mathrm{Tr}\{\sinh^2(2\boldsymbol{R})\} + \mathrm{Tr}\{\sinh^2(\boldsymbol{R})\}^2 \\
\langle \hat{n}_b^2 \rangle &= \langle \xi | (\hat{\tilde{\boldsymbol{b}}}^\dagger \hat{\boldsymbol{b}})^2 | \xi \rangle = \frac{1}{4}\mathrm{Tr}\{\sinh^2(2\boldsymbol{R})\} + \mathrm{Tr}\{\sinh^2(\boldsymbol{R})\}^2,
\end{aligned} \tag{3.33}$$

which gives the number variance

$$\langle (\Delta \hat{n}_a)^2 \rangle = \langle (\Delta \hat{n}_b)^2 \rangle = \frac{1}{4}\mathrm{Tr}\{\sinh^2(2\boldsymbol{R})\}, \tag{3.34}$$

each of which reduces to the familiar result for the case of single transverse spatial modes. In similar fashion, the covariance is

$$\mathrm{cov}(\hat{n}_a, \hat{n}_b) = \frac{1}{4}\mathrm{Tr}\{\sinh^2(2\boldsymbol{R})\}. \tag{3.35}$$

Next, we wish to investigate the inter-spatial-mode photon-number correlations in a way that the covariance cannot. Typically, one would investigate the probability $P_{\ell,p}$ of finding photons in the ℓ, p mode. However, this information is naturally contained along the diagonal of the average photon number matrix

$$\bar{\boldsymbol{n}} = \langle \hat{\boldsymbol{a}}^\dagger \hat{\tilde{\boldsymbol{a}}} \rangle = \sinh^2(\boldsymbol{R}). \tag{3.36}$$

Thus, we calculate the photon-pair creation matrix which reveals the coupling strength between TSM's of the spatial modes $\hat{\boldsymbol{a}}$ and $\hat{\boldsymbol{b}}$:

$$\boldsymbol{M}_{a\leftrightarrow b} \equiv \langle \hat{\boldsymbol{a}}^\dagger \widetilde{\hat{\boldsymbol{b}}^\dagger} \rangle = \frac{1}{2} e^{-i\boldsymbol{\Theta}} \sinh(2\boldsymbol{R}). \tag{3.37}$$

When normalized, this matrix gives the probability of TSM's pairing in the nonlinear interaction, thus containing a photon pair.

3.2.4 Eigenmodes of Squeezing

In general, the squeezing matrix is neither symmetric nor Hermitian. However, under certain conditions, for example when the beam focal points are at the center of the non linearity, it can be normal. Therefore, the following analysis is valid, or a good approximation, for many experimental configurations. When $\boldsymbol{\xi}$ is normal, it can be diagonalized by a unitary. If we let $\boldsymbol{U}$ be the matrix whose columns are eigenvectors of $\boldsymbol{\xi}$, then we can diagonalize $\boldsymbol{\xi}$ according to $\boldsymbol{\xi}' \equiv \boldsymbol{U}^\dagger \boldsymbol{\xi} \boldsymbol{U}$. Furthermore, the decomposition yields the diagonal matrices $\boldsymbol{R}'$ and $\boldsymbol{\Theta}'$. The corresponding eigenmodes of squeezing are found according to $\hat{\boldsymbol{a}}' \equiv \boldsymbol{U}^\dagger \hat{\boldsymbol{a}}$, $\hat{\boldsymbol{b}}' \equiv \widetilde{\boldsymbol{U}} \hat{\boldsymbol{b}}$, $\hat{\boldsymbol{a}}^{\dagger\prime} \equiv \widetilde{\boldsymbol{U}} \hat{\boldsymbol{a}}^\dagger$, and $\hat{\boldsymbol{b}}^{\dagger\prime} \equiv \boldsymbol{U}^\dagger \hat{\boldsymbol{b}}^\dagger$. It follows that their Bogoliubov transformations have a particularly simple form. The ith modes in the eigenmode vectors become

$$\begin{aligned}
\hat{S}^\dagger(\boldsymbol{\xi})\, \hat{a}'_i\, \hat{S}(\boldsymbol{\xi}) &= \cosh R'_i\, \hat{a}'_i + \sinh R'_i\, e^{i\Theta'_i}\, \hat{b}_i^{\dagger\prime} \\
\hat{S}^\dagger(\boldsymbol{\xi})\, \hat{b}'_i\, \hat{S}(\boldsymbol{\xi}) &= \cosh R'_i\, \hat{b}'_i + \sinh R'_i\, e^{i\Theta'_i}\, \hat{a}_i^{\dagger\prime} \\
\hat{S}^\dagger(\boldsymbol{\xi})\, \hat{a}_i^{\dagger\prime}\, \hat{S}(\boldsymbol{\xi}) &= \cosh R'_i\, \hat{a}_i^{\dagger\prime} + \sinh R'_i\, e^{-i\Theta'_i}\, \hat{b}'_i \\
\hat{S}^\dagger(\boldsymbol{\xi})\, \hat{b}_i^{\dagger\prime}\, \hat{S}(\boldsymbol{\xi}) &= \cosh R'_i\, \hat{b}_i^{\dagger\prime} + \sinh R'_i\, e^{-i\Theta'_i}\, \hat{a}'_i,
\end{aligned} \tag{3.38}$$

where R'_i are the diagonal elements of $\boldsymbol{R}'$, and Θ'_i are the diagonal elements of $\boldsymbol{\Theta}'$. Thus, the eigenmodes of squeezing are fundamental in the sense that they transform according to the canonical two-mode squeezed vacuum equations [68]. They also define a basis in which to analyze the squeezing and determine which modes are squeezed the most. The largest λ_i

corresponds to the largest multimode squeezing and $\hat{a}'_i$ gives that collection of modes.

The question remains, whether one can use the eigenmodes of squeezing as a basis to represent our squeezed state $|\boldsymbol{\xi}\rangle$. Thus, we first need to test whether the eigenmodes satisfy the canonical commutation relation. Evidently,

$$[\hat{a}'_i, \hat{a}'^{\dagger}_j] = U^{\dagger}_{ik} U_{kj} = \delta_{ij}, \tag{3.39}$$

and we find that the squeezed state takes the particularly simple form

$$|\boldsymbol{\xi}\rangle_{\lambda} = \sum_{i,n} \operatorname{sech}(\lambda_i) \tanh^n(\lambda_i) |\{n\}_i\rangle_A |\{n\}_i\rangle_B, \tag{3.40}$$

where A, B indicate the two spatial modes $\hat{\boldsymbol{a}}, \hat{\boldsymbol{b}}$ respectively, and $|\{n\}_i\rangle$ is the multimode Fock state with n photons in the i^{th} eigenmode. We can use these states as our basis states since $\langle \hat{a}^{\dagger}_{\lambda} \hat{b}^{\dagger}_{\lambda'} \rangle = \delta_{\lambda,\lambda'}$, in other words, the photons are created pairwise in the same eigenmodes.

4 Theoretical Explanation of PSR Experiment

In this chapter we will revisit the topic of TSM squeezing generated via PSR. In Chapter 2 we discussed our experimental findings; we investigated the TSM structure by incorporating spatial masks and by changing the optical depth of the atomic vapor. We presented clear evidence for the presence of higher order spatial modes in the TSM structure of the squeezed vacuum beam. Now, we will use the theory developed in the previous chapter to investigate the PSR squeezing interaction.

4.1 Semiclassical Regime

4.1.1 TSM Generation

As we discussed in Section 1.2.2, there are several ways to model the polarization $\tilde{\mathbf{P}}$. In this case, we will take a phenomenological approach based on the expansion in Eq. 1.19. Since the pump beam is linear polarized, we can suppress the tensor nature of the susceptibility and write

$$\tilde{P}^{(3)}(\omega) = \epsilon_0 \chi^{(3)}(\omega)\ \tilde{E}(\omega)|\tilde{E}(\omega)|^2, \tag{4.1}$$

where, in this case, the argument ω simply reminds us that the interaction is degenerate in frequency. Inserting this into the wave equation (Eq. (1.17)) we find

$$\nabla^2 \tilde{E} - \frac{1}{c^2}\frac{\partial^2 \tilde{E}}{\partial t^2} = \frac{1}{c^2}\chi^{(3)}\frac{\partial^2}{\partial t^2}\ \tilde{E}\,|\tilde{E}|^2. \tag{4.2}$$

As before, we make the substitution $\tilde{E}(\boldsymbol{r}, t) = \mathcal{E}(\boldsymbol{r}_\perp, z)\exp[i(kz - \omega t)]$ and find the paraxial wave equation

$$(\frac{\partial}{\partial z} - \frac{i}{2k}\nabla_\perp^2)\mathcal{E} = \frac{ik}{2}\,\chi^{(3)}\ \mathcal{E}|\mathcal{E}|^2, \tag{4.3}$$

where the phase matching conditions have been naturally satisfied. Next, using the Born approximation, we make the substitution $\mathcal{E}_0 = \varepsilon_0\, u_{0,0}$ on the r.h.s., since the pump beam is

The majority of this chapter is derived from Refs. [1, 2] published under Copyright © 2011 by the American Physical Society.

in the LG $\ell = 0$, $p = 0$ mode:

$$(\frac{\partial}{\partial z} - \frac{i}{2k}\nabla_\perp^2)\mathcal{E} = \frac{ik}{2}\chi^{(3)}\ \varepsilon_0|\varepsilon_0|^2\, u_{0,0}|u_{0,0}|^2. \tag{4.4}$$

Thus, now the propagation equation is in a form suitable for our Green's function solution method. In this approximation we can regard the r.h.s. of Eq. (4.4) as the source $\wp$ of new mode structure to the beam, which further simplifies the notation. We pause to point out that, since the propagation equation inherits no ϕ dependence from either the atoms or the input fields, the beam solutions will be limited to $\ell = 0$ modes. This is clearly seen through the integral for the $c_{\ell,p}$ coefficients, by noting that $\wp = \wp(r, z)$, and separating the ϕ phase from the LG mode:

$$c_{\ell,p}(z) = \int r dr \wp(r, z)\ u^*_{\ell,p}(r, z) \int_0^{2\pi} d\phi\ e^{i\ell\phi}. \tag{4.5}$$

As one can see, the ϕ integral vanishes for $\ell \neq 0$. We can now write our final solutions for the spatial-amplitude function:

$$\mathcal{E} = \mathcal{E}_0(\boldsymbol{r}) + \alpha \sum_p u_{0,p}(\boldsymbol{r}) \int_{\text{cell}} dz' c_{0,p}(z'), \tag{4.6}$$

where

$$c_{0,p}(z) = 2\pi \int r dr\ u^*_{0,p}(\boldsymbol{r})\ \wp(\boldsymbol{r}), \tag{4.7}$$

and the the parameter α has been introduced to characterize the strength of the interaction. In principle, such a factor is not necessary, but in this case the model cannot capture the full complexity of the experiment, and we will use α as a fitting parameter to fit the theory to the measured data. Thankfully, in this case these integrals are relatively simple, and our calculation showed that the summation converges rapidly for $p \leq 5$. Equipped with the output beam structure, we will revisit the spatial mask experiment in which we translated the iris masks through a focus after the nonlinear cell [see Fig. 2.3(e) and 2.3(f)].

4.1.2 TSM Properties of the Focused Output Beam

Evaluating Eq. (4.6), we find that as we suspected, the semiclassical theory predicts a mixture of several different higher order modes. Now that we know the new mode structure of the beam, we can fit the output beam [Eq. (4.6)] to the transmission data using the fitting parameter α. The data was originally presented in Section 2.2, but we include it in Figs. 4.1(a) and 4.1(c) for quick reference. First, starting with $\alpha = 0$, it was apparent that mode structure of the LO had changed. The pump beam is actually slightly focused by the nonlinearity, so with $\alpha = 0$, we have the waist of the original beam $\mathcal{E}_0$, which makes our theoretical transmission plot narrower than the experimental transmission plot in Fig. 4.1(a). Therefore, we increased α until the two aligned, which shows that the higher order p-mode

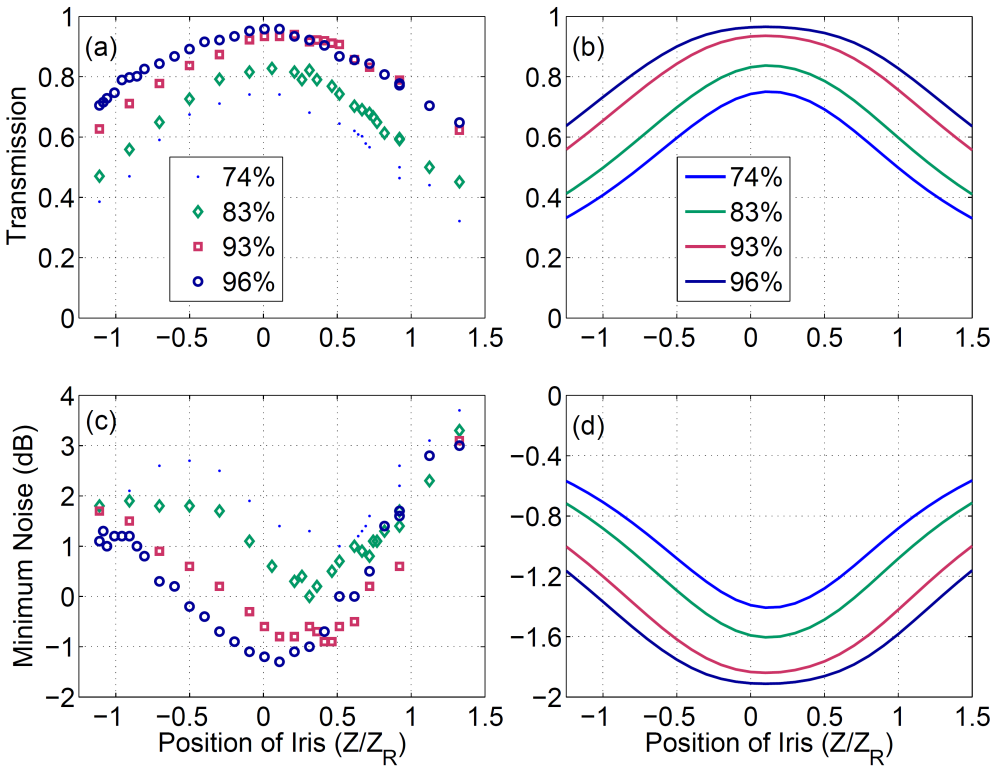

Figure 4.1. Comparison of the experimental and theoretical (left and right column) dependencies of the LO beam transmission (top row) and the squeezed field minimal noise power (bottom row) on the iris position for several fixed iris sizes. The legend denotes the peak transmission for each iris. Note that the Rayleigh range z_R =2.5 cm. To calculate transmission and noise power, we used Eq. (4.6) and Eq. (2.1).

structure is consistent with the self-focusing nature of the interaction. In Figure 4.1(b) we present the theoretical LO transmission through the iris. We find excellent agreement, for each iris size, even though a single α was used for every case. The only noteworthy deviation is for the 92% iris, and this is now believed to be an experimental error in the measurement.

Based on the beam splitter model in Eq. (2.1), we calculate the expected minimum noise as in Fig. 4.1(d). In the theoretical plot, the noise is always lower than shot noise since the model does not take into account the excess noise. But, we can still compare it with Fig. 4.1(c) and find the overall behavior is quite similar. In both plots, the minimum in the noise power traces shift to the right, that is, farther from the beam focus as the iris size shrinks. The qualitative agreement of these plots is further evidence of the LG structure of the squeezed vacuum beam. A more rigorous description necessarily requires a quantum treatment of both the light-matter interaction and the interaction with the spatial masks. Therefore, in Section 4.2 we will use our second quantization procedure and predict the distribution of the quantum noise in the individual LG modes. We have also developed a quantum treatment of the interaction with the spatial masks which can be found in Refs. [76, 77]

4.1.3 Optical Depth

The optical depth study in Chapter 2 revealed that squeezing could be enhanced by decreasing the atomic number density (N) and increasing the interaction length (L), in such a way to keep the effective optical depth ($d \propto NL$) constant. This is best observed in Fig. 2.5, where the double pass scheme beats the single-pass scheme. This observation can be explained in part by investigating the higher-order mode structure of the pump beam.

An example of higher-order mode generation in the pump field is shown in Fig. 4.2. As expected, for lower atomic density, the intensity distribution of the pump beam is well approximated by the the fundamental Gaussian mode $p = 0$. However, if we operate the experiment above the optimal atomic density, we can start observing clear signs of a more

complicated transverse structure in the output pump beam. Namely, Figure 4.2(c) shows a ringlike formation, characteristic of the higher-order LG modes. This behavior is even more clear in the mode-decomposition diagrams, shown in Figs. 4.2(b) and 4.2(d). As we showed in Eq. (4.5), no higher-order ℓ modes are expected due to the conservation of the optical angular momentum in the PSR process. It is clear that even though the fundamental Gaussian mode dominates, the contribution of the higher-order p modes increases dramatically with the temperature.

Similar behavior is also predicted by our theory. Figure 4.3 tracks the change in the amplitudes of the generated higher-order modes $|c_p|$ for $p = 0$ to $p = 4$, in the cases where the number density of atoms increases, or the length of the atomic medium increases. In

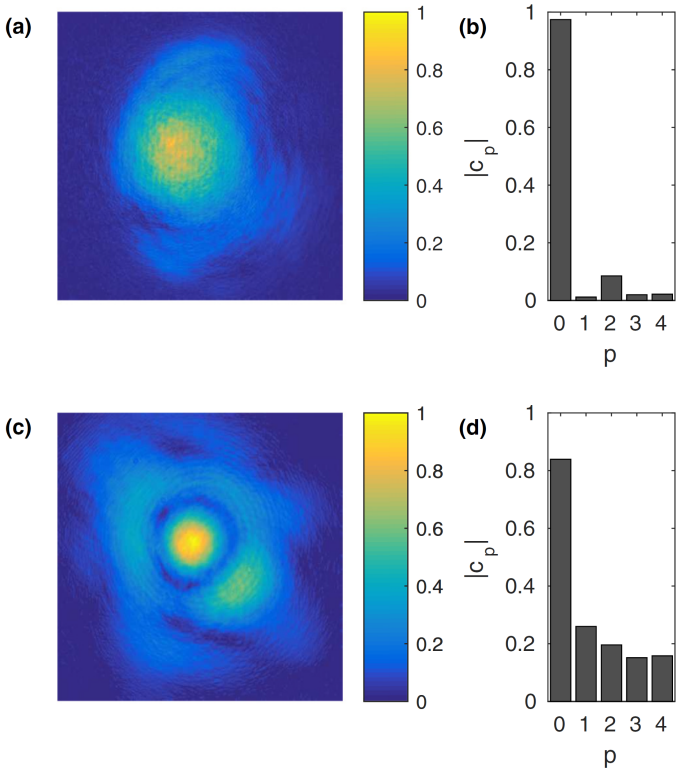

Figure 4.2. Transverse intensity distribution of the pump field (a) and the magnitude of the calculated deconvolution coefficients $|c_p|$ after the cell at room temperature ($T = 26^o$C, $N = 10^{10}$cm^{-3}). Small beam contamination due to diffraction gives rise to higher order $|c_p|$ coefficients. Corresponding results for the pump beam after the interaction with the vapor cell at high temperature ($T = 91^o$C, $N = 2.6^{12}$cm^{-3}) are shown in (c) and (d).

Figure 4.3(a) we plot the output mode structure of the pump field at the output of the vapor cell for several values of atomic density N. The first step in the plot corresponds to an empty vapor cell (N = 0), so we only see response in c_0 corresponding to the $u_{0,0}$ mode. The density increases to the optimal squeezing density $N_{\text{sngl}}^{\text{opt}}$ at the third step of the plot, and we are able to see the relative contribution of new modes at that coupling strength. Further increase of the atomic number density subsequently increases the contribution of the higher-order modes, which as we will show in the next section, can degrade the overall squeezing. When the length L of the atomic medium is increased at a constant atomic density $N_{\text{sngl}}^{\text{opt}}$, one observes a distinctly different behavior: As the interaction length increases, the strength of the contaminating modes ($p > 0$) goes down, potentially improving the squeezing. Such different effects for increasing the nominal optical depth NL should not be too surprising. The underlying interaction is nonlinear and strongly intensity-dependent, which means that the pump profile, and thereby the vacuum mode structure, can change quite drastically. In the next section, we will use our theory to predict how the noise suppression is distributed among the beam. Furthermore, we'll show how the higher order TSM structure can degrade the overall squeezing.

4.2 Quantum Regime

The tensor nature of this $\chi^{(3)}$ interaction is the fundamental phenomenon related to the PSR effect, and it is worked out in detail for classical fields [58]. This was eluded to in Section 2.1.1, where we discussed how the different polarization components interact in the nonlinearity. Quantized treatments have also been performed, which relate the observed noise suppression to the amount of polarization self-rotation observed in the medium [45]. The early work predicted levels of noise suppression, which have proven to be woefully over optimistic. This realization prompted more rigorous noise calculations [78] and our experimental study of the transverse spatial modes excited during the interaction [1, 2], which we presented in Chapter 2. With our preceding theory, we are finally able to perform a fully second-quantized analysis of the transverse spatial mode structure. For brevity, and to

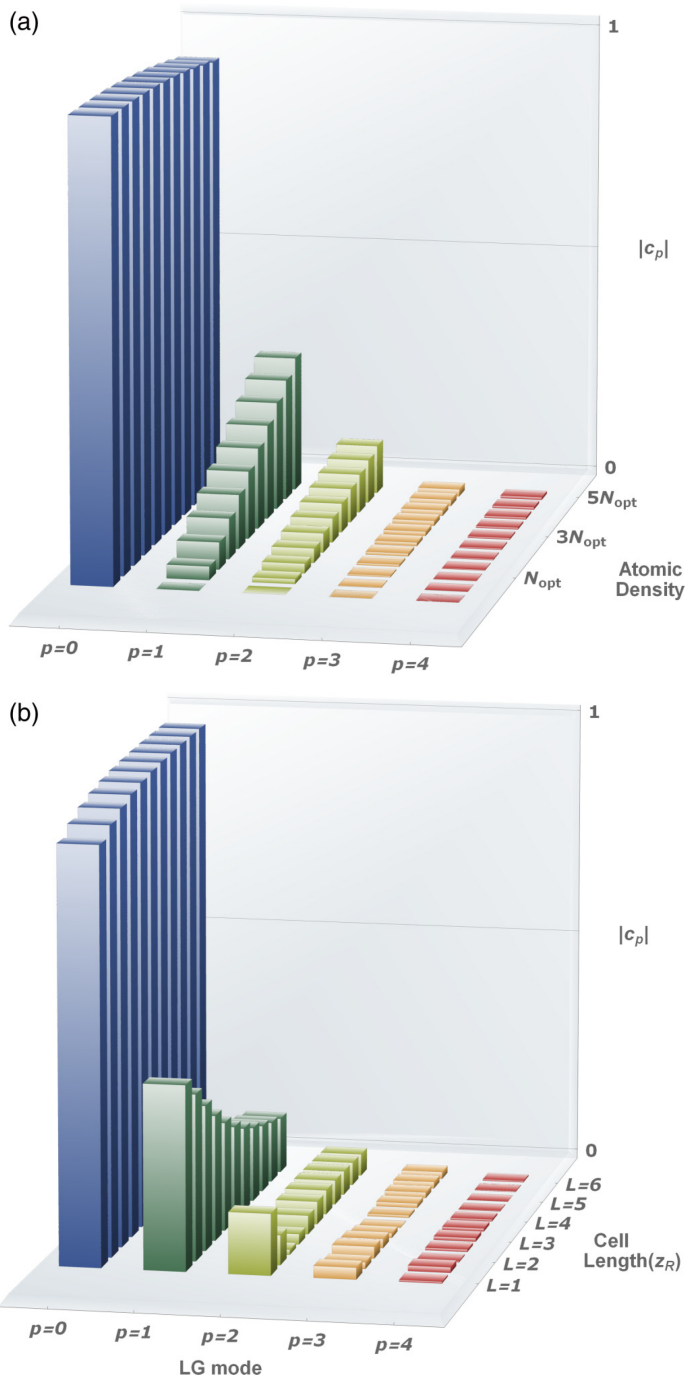

Figure 4.3. The calculated relative amplitudes of the first few higher-order TSMs as (a) the atomic number density N gradually increases or as (b) the length of the atomic medium L is increased, keeping the focus at the center of the cell. One can see that increasing the atomic density steadily increases the stimulation of higher-order modes. On the contrary, increasing the length can have the opposite effect and suppress higher-order modes.

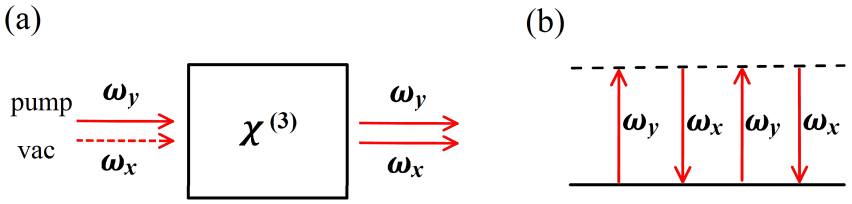

Figure 4.4. Description of the PSR effect used in our experiment. In (a) we depict the four wave mixing interaction between a y-polarized pump beam and vacuum fluctuations in the x polarization. Quantumly, we can describe the interaction using the tensor element χ_{xyxy}, that is, response in x due to stimulation in yxy, depicted in (b).

keep the proceeding relatively straightforward, we will analyze the PSR effect in terms of the resonance structure of the interaction. In other words, we will not consider spatial structure of $\chi^{(3)}$. The classical formulation, for general third-order interactions, divides the interaction into single- and two-photon resonant contributions, each with different photon polarization interaction processes. The PSR process can be analyzed as a single-photon resonant process (see Fig 4.4), and serves as a stepping stone to more complex interactions. Later in Chapter 6, we will discuss the two-photon resonant interactions in FWM (see Fig. 6.1) and other more complex spontaneous nonlinear interactions.

The single-photon resonance structure of PSR implies that this is a single mode interaction. In other words, since the photons scattered into the x polarization are separated by y-polarization excitation, it is reasonable to assume that the two x-polarization photons do not have transverse-spatial-mode correlations, that is, there is no cross talk between the two x-photon emissions. The absence of cross talk means that we should let $\hat{\boldsymbol{b}} \to \hat{\boldsymbol{a}}$ and thus have a single-spatial-mode squeezing process. We will see that the single-mode nature of this process suppresses the creation of modes with OAM, as is observed experimentally.

To make the preceding discussion abundantly clear, we'll start with the interaction Hamiltonian

$$H \propto \int d\mathbf{r}^3 \chi^{(3)} \left(\hat{E}_y^{(-)2}(\mathbf{r},t)\, \hat{E}_x^{(+)2}(\mathbf{r},t) - \text{h.c.} \right), \tag{4.8}$$

where $\chi^{(3)} = \chi^{(3)}_{xyxy}$ is the nonzero element of the third order tensor susceptibility, $\hat{E}^{(\pm)}$ corresponds to the positive and negative frequency components of the field, x corresponds to the vacuum mode, and y correspond to the pump mode. In Chapter 2, we discussed in detail the setup for the PSR experiment, which is beautiful in it's simplicity. The single pump beam in a $u_{0,0}$ mode co-propagates with the x-polarized vacuum, along the z axis, before and after the interaction with the atomic vapor. This, in conjunction with the degeneracy in frequency allows us to write the quantum fields as

$$\begin{aligned} \hat{E}_y^{(+)}(\mathbf{r},t) &= A_y\, u_{0,0}(\mathbf{r})\, \hat{y}\, e^{i(kz-\omega t)} \\ \hat{E}_x^{(+)}(\mathbf{r},t) &= \sum_{\ell,p} u_{\ell,p}(\mathbf{r})\, \hat{a}_{\ell,p}\, e^{i(kz-\omega t)}. \end{aligned} \tag{4.9}$$

Next, we can make the parametric approximation to rewrite the Hamiltonian Eq. (4.8) as

$$\hat{H} = \kappa \int d\mathbf{r}^3 \sum_{\ell p} \left(\chi^{(3)*}_{\ell,p} \hat{a}^2_{\ell,p} - \chi^{(3)}_{\ell,p} \hat{a}^{\dagger 2}_{\ell,p} \right), \tag{4.10}$$

where κ is a coupling constant, the effective susceptibility is

$$\chi^{(3)}_{\ell,p} \equiv C\, \chi^{(3)} \left(A_y\, u_{0,0}(\mathbf{r})\, u^*_{\ell,p}(\mathbf{r}) \right)^2, \tag{4.11}$$

C is a normalization constant, and the natural phase matching has allowed us to drop the exponential factor. From here, the two-photon amplitude matrix $\boldsymbol{\chi}$ takes the simpler diagonal form

$$\boldsymbol{\chi} \equiv \sum_{\ell p} \hat{e}_{\ell+1} \otimes \hat{e}_{p+1}\, \chi_{\ell-\ell_{\max},p} \left[\hat{e}_{\ell+1} \otimes \hat{e}_{p+1} \right]^T, \tag{4.12}$$

where again $\hat{e}_i$ is a vector with 1 in the i'th position, and the sum runs over $0 \le \ell \le 2\ell_{\max}+1$ and $0 \le p \le p_{\max}$. However, similar to what we showed in the previous section, we can reveal that the squeezing will be limited to $\ell = 0$ modes. Every element of the squeezing matrix is

proportional to the form

$$\int d^3\boldsymbol{r}\big(u_{0,0}(\mathbf{r})\,u^*_{\ell,p}(\mathbf{r})\big)^2 = \int r\,dr\,\big(u_{0,0}(\mathbf{r})\,u^*_{\ell,p}(r,z)\big)^2\,\int_0^{2\pi} d\phi\,e^{i\,2\ell\,\phi}, \tag{4.13}$$

where on the r.h.s we extracted the ϕ phase from the LG mode. As one can see, the ϕ integral vanishes for $\ell \neq 0$, and the squeezing matrix takes a simple diagonal form with elements

$$\xi_p = \int d^3\boldsymbol{r}\,C\,\chi^{(3)}\,A_y^2\,\big(u_{0,0}(\mathbf{r})\,u^*_{0,p}(\mathbf{r})\big)^2, \tag{4.14}$$

extending along the diagonal, where $0 \leq p \leq p_{\max}$. Thus, using the equations for the quadrature variance in Section 3.2, we know how the noise is distributed among the spatial modes. Furthermore, since $\boldsymbol{\xi}$ is diagonal, we are naturally working with the eigenmodes of squeezing. Thus, we can find the effective squeezing parameter r_p and squeezing angle θ_p for each p mode:

$$\xi_p = r_p e^{i\theta_p}, \tag{4.15}$$

where $r_p = |\xi_p|$. To visualize these results, we will use the the squeezed vacuum Wigner function, labeled here for each l, p mode:

$$\begin{aligned} W_{l,p}(x,y) = \frac{2}{\pi}\exp\Big[&- (y^2+x^2)\cosh r_{l,p} \\ &+\big((x^2-y^2)\cos\theta_{l,p} + 2xy\sin\theta_{l,p}\big)\sinh r_{l,p}\Big]. \end{aligned} \tag{4.16}$$

The Wigner function is a phase space distribution that contains all the information of the state. It is the mathematically rigorous analogy to the phase space sketches in Fig. 1.3, which can be thought of as a slice of the Wigner function.

Using quantum state tomography, we reconstructed the Wigner function for our squeezed vacuum state, with the best noise suppression we were able to achieve [see Fig. 4.5(a)]. This Wigner function looks very squeezed, but actually corresponds to noise suppression of 1.9 ± 0.2 dB below the SQL level in the maximally squeezed quadrature, which is a modest

amount of squeezing compared to the predictions of the single-mode theory [45, 78, 79]. However, our theory suggests that more significant squeezing could be hiding in the spatial mode structure of the beam. To show this, we use the coupling constant κ in Eq. (4.10) as a fitting parameter, adjusted so that the minimum quadrature noise predicted by our homodyne detection calculation, provides 1.9 dB noise suppression in the X_1 quadrature (with $\theta/2 = 0$). For reference, the Wigner function of our theoretical model is plotted in Fig. 4.5(b). Next, we will discuss the homodyne-detection calculation, and show how we reveal the squeezing in the TSMs.

The photocurrent-difference variance (see Section 1.4) is a weighted sum of quadrature

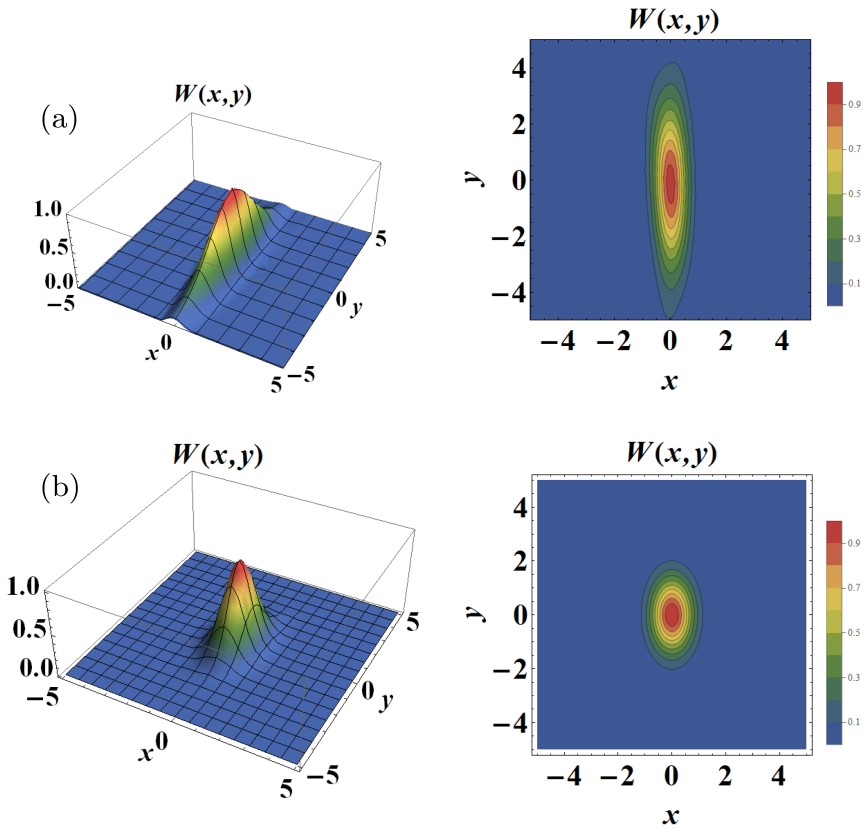

Figure 4.5. (a) Wigner function of the experimentally realized squeezed state and (b) an ideal theoretical minimum uncertainty state with 1.9 dB of squeezing along the X_1 quadrature, shown here in 3D and contour. The axis labels x and y are proportional to the X_1 and X_2 quadratures, respectively. The Wigner function has been rescaled by the peak amplitude of the vacuum Wigner function. In Figure 4.6 we show the underlying mode structure that recreates predicted by the theory.

variances (some squeezed, some anti-squeezed) of all modes which overlap the LO [68]. As we have previously shown, only the modes with $\ell = 0$ are relevant to our experiment due to symmetry and consideration of angular momentum. Then, one can show it takes the form

$$\left\langle (\Delta i_d)^2 \right\rangle \propto \sum_p |O_p|^2 [e^{-2r_p} \cos^2(\text{Arg } O_p) + e^{2r_p} \sin^2(\text{Arg } O_p)], \tag{4.17}$$

where we define the overlap integral O_p as

$$O_p \equiv \frac{\int \mathcal{E}_{\text{LO}}^* u_{0,p} \, d^3r}{\sqrt{\int |\mathcal{E}_{\text{LO}}|^2 \, d^3r}}, \tag{4.18}$$

$\mathcal{E}_{\text{LO}}$ is the local oscillator, and $u_{0,p}$ is the spatial function of the p^{th} mode.

To take care of the adjusting the parameter κ, we first recognize that for our measured state, Eq. (3.28) reduces to $\left\langle (\Delta \hat{X}_{1,2})^2 \right\rangle = (1/4)e^{\mp 2r_{\text{exp}}}$. Furthermore, in the limit of a strong LO, the photo-current difference variance is

$$\left\langle (\Delta i_d)^2 \right\rangle \propto 4|\mathcal{E}_{\text{LO}}|^2 \left\langle (\Delta \hat{X}(\theta))^2 \right\rangle \tag{4.19}$$

where $\hat{X}(\theta) = (1/2)(\hat{a}e^{-i\theta} + \hat{a}^\dagger e^{i\theta})$ is the field quadrature operator at the angle θ. Therefore, combining Eq. (4.17) and Eq. (4.19), we solve the following equation for κ:

$$|\mathcal{E}_{\text{LO}}|^2 e^{-2r_{\text{exp}}} = \sum_p |O_p|^2 [e^{-2\ r_p} \cos^2(\text{Arg } O_p) + e^{2\ r_p} \sin^2(\text{Arg } O_p)] \tag{4.20}$$

where $r_{\text{exp}} \approx 0.565$ is the experimental squeeze parameter and $|\mathcal{E}_{\text{LO}}|^2 = \int r dr d\phi \, \mathcal{E}_{\text{LO}}^* \mathcal{E}_{\text{LO}}$. Thus, we have determine the re-scaled LG squeeze parameters r_p' and point out that the squeeze angles $\theta_p = \text{Arg}(\xi_p)$ remain the same.

Figure 4.6 shows the Wigner functions for the squeezed LG modes, which comprise the squeezed state predicted by the theory. The $p = 3$ and higher modes are omitted since they show no appreciable squeezing. It is important to point out that if only the fundamental

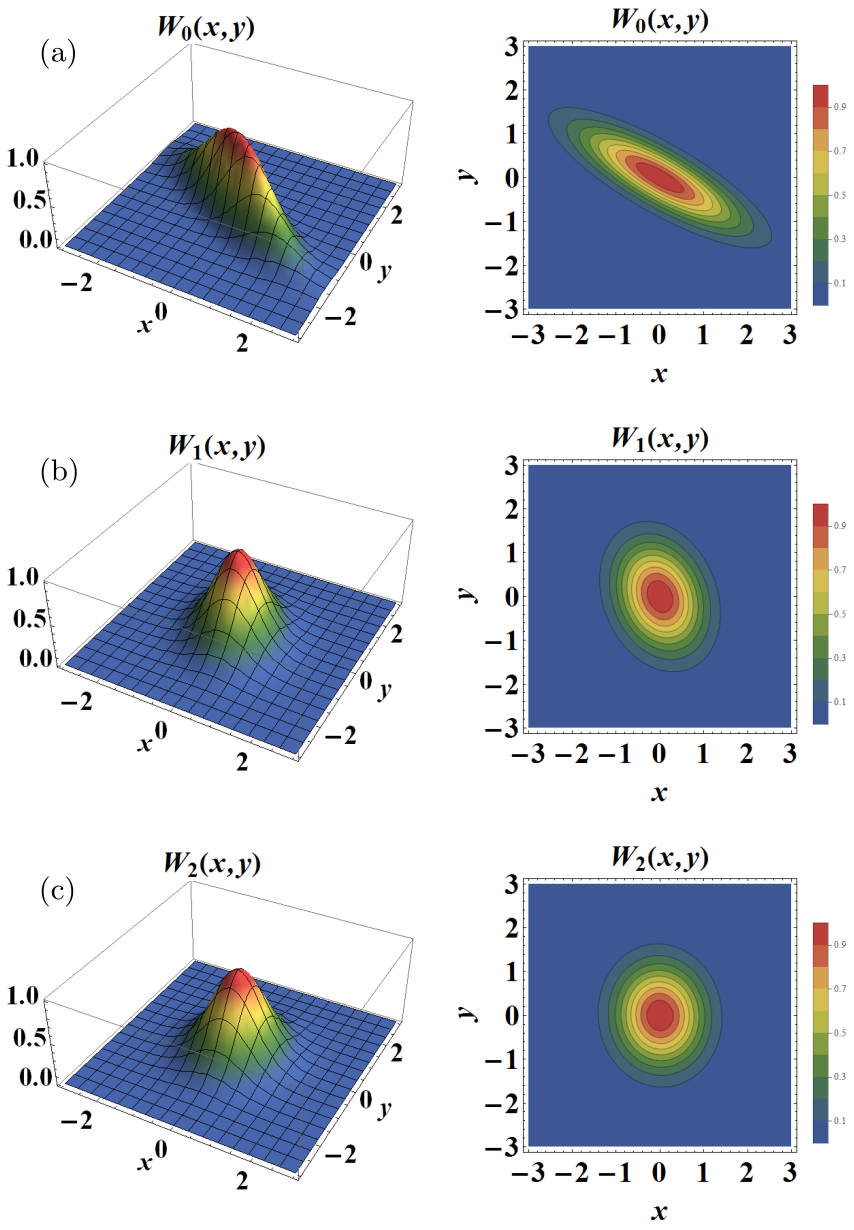

Figure 4.6. Wigner functions for the (a) p=0, (b) p=1, and (c) p=2 LG modes predicted by the theory. When measured simultaneously via homodyne detection, they result in the same squeezing depicted by the Wigner function in Fig. 4.5(b). In other words, since the homodyne detection scheme is ignorant to the underlying TSM mode structure, the hidden noise suppression is lost, and the noise combines in such a way to deteriorate squeezing. The $p = 3$ and greater modes are omitted since they appear essentially as vacuum modes. The axis labels x and y are proportional to the X_1 and X_2 quadratures respectively. The Wigner functions have been rescaled by the peak amplitude of the vacuum Wigner function.

mode $p = 0$ could be isolated, its minimum quadrature noise would have been measured to be more that 11 dB below the shot noise. The $p = 1$ by itself (if isolated) would have displayed -3 dB of squeezing, but at the different quadrature angle, and the trend continues for higher modes, quickly approaching a coherent state. Thus, we find that there is actually much more squeezing available in the individual modes, but in combination the overall noise suppression is much worse due to the fact that the squeezing angles are out of phase. Looking back to Eq. (4.14) and Eq. (4.15), it is easy to see now how the different Gouy phase for each mode can oscillate at a different rate and influence the squeezing angles. Extracting the phase factors, we can rewrite Eq. 4.14 as

$$\xi_p = \int d^3\boldsymbol{r}\, C\, \chi^{(3)}\, A_y^2 \left(|u_{0,0}(\mathbf{r})|\, |u_{0,p}^*(\mathbf{r})|\right)^2 e^{-i\,4pG(z)}, \tag{4.21}$$

where $G(z) \equiv \arctan(z/z_R)$. Thus, it is clear that it is the p dependence of the Gouy phase that gives rise to the different squeezing angles θ_p.

5 Simulations — OAM Transfer

In this chapter, we present simulations which showcase our semiclassical theory. First, we focus on experimentally relevant simulations related to PDC and spontaneous FWM. For PDC, we take the results of the experiment a step further by suggesting ways to enhance the mode structure of the generated beam. For FWM, we address an unresolved problem pertaining to the pathways of OAM transfer in spontaneous FWM. For each simulation, we will specify the polarization governing the interaction, along with the relevant beam and nonlinearity parameters. Furthermore, all beam profiles are plotted at $z = 0$, and are color coded to match the visible spectrum as closely as possible.

5.1 Stimulated Down Conversion

A rapidly evolving body of theoretical work is calling for entanglement in quantum systems with higher dimensions [80, 81]. Thus, as an exercise, we will study stimulated PDC as a way to understand the properties of down-converted twin beams when a cavity is not present to alter the mode structure. We model a PDC experiment, in which a 442-nm pump beam interacts with a 845-nm signal beam (in a 3-mm long BBO crystal) to create a 925-nm idler beam [8]. Due to the small incident angle of the signal beam and the relatively thin crystal, effects from the non-collinear geometry are negligible. The light-matter interaction in the crystal, depicted in Fig. 5.1(a), is governed by the polarization

$$\tilde{P}(\omega_i)^{(2)} = \epsilon_0 \chi^{(2)} \tilde{E}_p(\omega_p) \tilde{E}_s(\omega_s)^*, \tag{5.1}$$

where ω_p, ω_s, and ω_i are the angular frequencies of the pump, signal, and idler photons respectively. Furthermore, $\tilde{E}_p$ is the pump beam, $\tilde{E}_s$ is the signal beam, and the conjugation of $\tilde{E}_s$ corresponds to the creation of a photon in the input signal mode. Therefore, we see how the choice of pump and signal modes tailor the response of the idler beam; this phenomenon has been verified experimentally for relatively simple input beams [8]. The

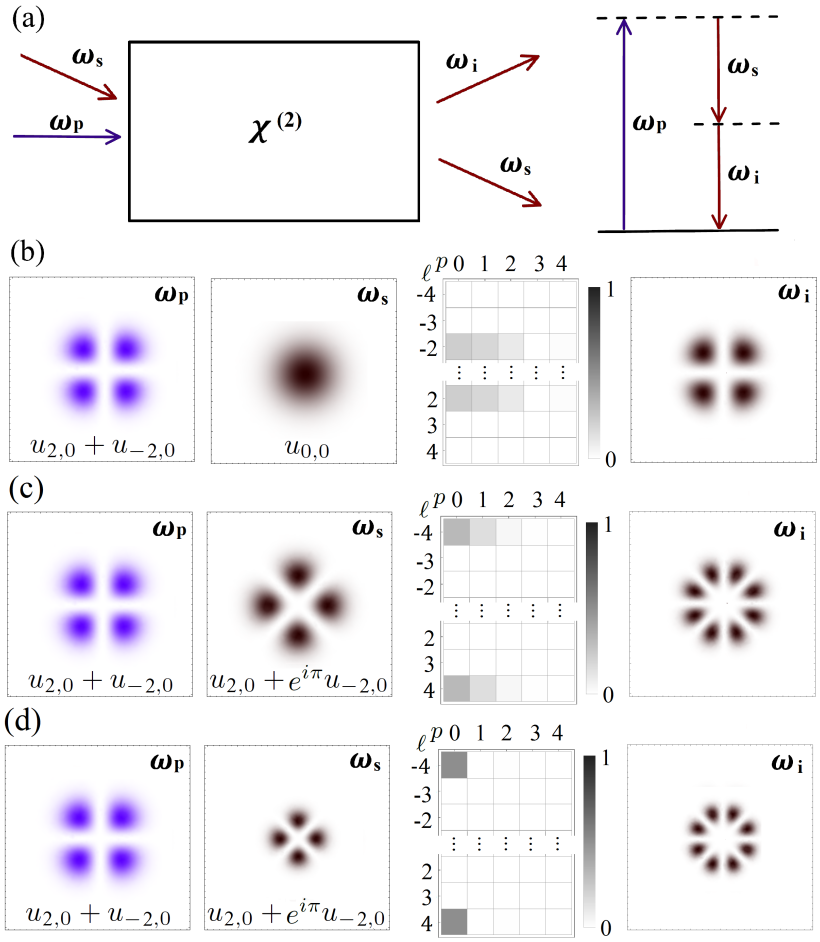

Figure 5.1. (a) Stimulated-down-conversion scheme of our simulation, (b) - (d) the input beam profiles of the pump and signal beams, a histogram giving the mode structure of the output (idler) beam, and the spatial profile of the output (idler) beam respectively. In (b) we use a $u_{0,0}$ signal as a baseline, then in (c) and (d), we show how the signal beam can be chosen to tailor a clean higher OAM superposition in the idler mode.

waist of the basis set, used to represent the generated beam, is set to match the waist of the pump beam. In reality, the nonlinear interaction will stimulate a continuum of LG modes with slightly different waists. Experimentally, one has to select a particular beam waist to target in the detection scheme. Therefore, we choose a "detection waist" and we will see how the interplay of the waist and Rayleigh range, of the input beams, effects the TSM structure of the generated beam at that particular waist. With these parameter chosen, we can insert

our polarization into the wave equation [Eq. (1.17)] and find

$$\nabla^2 \tilde{E}_i - \frac{1}{c^2}\frac{\partial^2 \tilde{E}_i}{\partial t^2} = \frac{1}{c^2}\chi^{(2)}\frac{\partial^2}{\partial t^2}\ \tilde{E}_p\, \tilde{E}_s. \tag{5.2}$$

As we have done before, we make the substitutions

$$\begin{aligned} \tilde{E}_p(\boldsymbol{r},t) &= \mathcal{E}_p(\boldsymbol{r}_\perp, z)\exp[i(k_p z - \omega_p t)] \\ \tilde{E}_s(\boldsymbol{r},t) &= \mathcal{E}_s(\boldsymbol{r}_\perp, z)\exp[i(k_s z - \omega_s t)] \\ \tilde{E}_i(\boldsymbol{r},t) &= \mathcal{E}_i(\boldsymbol{r}_\perp, z)\exp[i(k_i z - \omega_i t)] \end{aligned} \tag{5.3}$$

and find the paraxial wave equation

$$(\frac{\partial}{\partial z} - \frac{i}{2k_i}\nabla_\perp^2)\mathcal{E}_i\ e^{i(k_i z-\omega_i t)} = -\frac{1}{2ik_i}\,\chi^{(2)}\frac{(\omega_p-\omega_s)^2}{c^2}\ \mathcal{E}_p\ \mathcal{E}_s^*\ e^{i\left((k_p-k_s)z-(\omega_p-\omega_s)t\right)}, \tag{5.4}$$

where in this case we have kept the relative phases in order to demonstrate the phase matching. Since our interaction conserves energy and linear momentum, we will assume $\omega_i = \omega_p - \omega_s$ and $k_i = k_p - k_s$. This means we can drop the exponential factors and $(\omega_p - \omega_s)^2/c^2 = k_i^2$. Thus we have

$$(\frac{\partial}{\partial z} - \frac{i}{2k_i}\nabla_\perp^2)\mathcal{E}_i = \frac{i\,k_i}{2}\chi^{(2)}\ \mathcal{E}_p\ \mathcal{E}_s^*. \tag{5.5}$$

Now, we can use our Green's function solution to find the mode structure of the idler beam.

In this simulation, we investigate how to generate a high-OAM superposition in the idler mode. First, for reference, we consider that the signal beam is prepared in the $u_{0,0}$ mode with a waist that matches the pump beam. As one can see in Fig. 5.1(b), the idler beam responds in $\ell = \pm 2$ superposition, with a spreading in p modes. Each histogram depicts the probabilities $\mathscr{P}_{\ell,p}$ of modes being excited, that is, referring to Eq. (3.11),

$$\mathscr{P}_{\ell,p} \equiv \frac{|\int dz' c_{\ell,p}(z')|^2}{\sum_{\ell,p}|\int dz' c_{\ell,p}(z')|^2}. \tag{5.6}$$

Next, to increase OAM in the idler beam, we prepare a signal beam in the same superposition as the pump, but include a π phase shift between the two modes in the superposition, that is, the signal beam is now $u_{2,0} + e^{i\pi}u_{-2,0}$. In Figure 5.1(c) we see that this combination creates a destructive interference, which suppresses response at $\ell = 0$, and produces an idler beam, which responds at $\ell = \pm 4$ with a spreading in p modes. More simulations using this technique can be found in the following section. The stimulation of higher-order p modes corresponds, in part, to a less than ideal overlap of the beams. Therefore, in Fig. 5.1(d), we show that one can optimize the signal-beam waist to suppress the higher order p modes. The narrowing of the signal-beam waist w_0 (by $\approx$ 40%), in Fig. 5.1(d), corresponds to a reduction of the Rayleigh range $z_R = \pi w_0^2/\lambda$. In effect, the beams now expand closer to the same rate, which is apparently the optimized beam overlap through the interaction region. This observation is related to the Boyd criterion [17], which states that, the nonlinear interaction is strongest when the Rayleigh ranges of the interacting beams coincide. The effect observed here extends this observation to include an improvement in the mode structure. This simulation is very useful, since one cannot determine the p mode structure experimentally by simply analyzing the intensity pattern, e.g., differences in the petal structures of ω_i, in Figs. 5.1(c) and 5.1(d), are not discernible, even though Fig. 5.1(c) has a contaminated mode structure.

5.2 Spontaneous Four-Wave Mixing

Next, we present a simulation for non-degenerate four wave mixing, depicted in Fig. 5.2(a). In this scheme, two pump beams spontaneously create signal and conjugate beams, according to the polarization

$$\mathcal{P}(\omega_c)^{(3)} = \epsilon_0 \chi^{(3)} \mathcal{E}(\omega_{p1}) \mathcal{E}(\omega_{p2}) \mathcal{E}(\omega_s)^*, \tag{5.7}$$

where $\omega_p 1$, $\omega_p 2$, and ω_s are the angular frequencies of the two pump beams and signal-beam photons respectively. In our other simulations, all of the fields which generate the new beam are carefully selected input beams. This simulation is distinct since the bright signal and conjugate beams are spontaneously created during the interaction. Therefore, to predict the mode structure of the conjugate beam, we must make assumptions about the spontaneous

response creating the signal beam $\mathcal{E}_s$, otherwise we cannot calculate $\mathcal{E}_i$. Thus, we need to develop a model which allows us to predict the coupling of the atoms to the vacuum LG modes at the signal and conjugate wavelengths.

To investigate this problem, we simulate an interaction, which has been experimentally realized [17]. A 780-nm pump and a 776-nm pump stimulate a nonlinear interaction in Rb, which is the source of a 5230-nm signal beam and a 420-nm conjugate beam [see Fig. 5.2(a)]. In the experiment, the long wavelength beam remains unobserved. However unlikely, OAM transfer to this beam should not be ruled out as a possibility. Rather, the atoms can couple to any spatial light mode, which obeys OAM conservation, and thus we should account for each of these modes in our simulation. Therefore, in this simulation, we input a signal beam that is a balanced superposition of all OAM modes, which obey OAM conservation, and allow the integral in Eq. (3.11) to determine which modes are stimulated. Thus, we accommodate for the possible OAM transfer to the long-wavelength beam, and only restrict our analysis to incoherent superposition at the signal wavelength. The last assumption we will impose for this simulation is the matching of the Rayleigh ranges for all beams, i.e., we invoke the Boyd criterion [17]. In effect, we judiciously choose the widths of the beams to maximize the nonlinear interaction, and this suggests which waist modes should be targeted during detection.

The results are presented in Figs. 5.2(b)–5.2(f). From left to right, the columns correspond to the profile of the pumps, a histogram giving the mode structure of the conjugate beam, the profile of the conjugate beam, and lastly the experimental data from Ref. [17]. We see excellent qualitative agreement, when the signal beam is allowed to carry OAM. In particular, our simulation appears to take account of the relative brightness and shape of the lobes in the experimental data. In each case there are lobes that are elongated and dimmer than others and our simulation agrees with this observation. It is apparent that the richer mode structure that we predict for the conjugate beam can account for the variations in the lobe brightness, without drastically affecting the lobe structure. Therefore, we emphasize

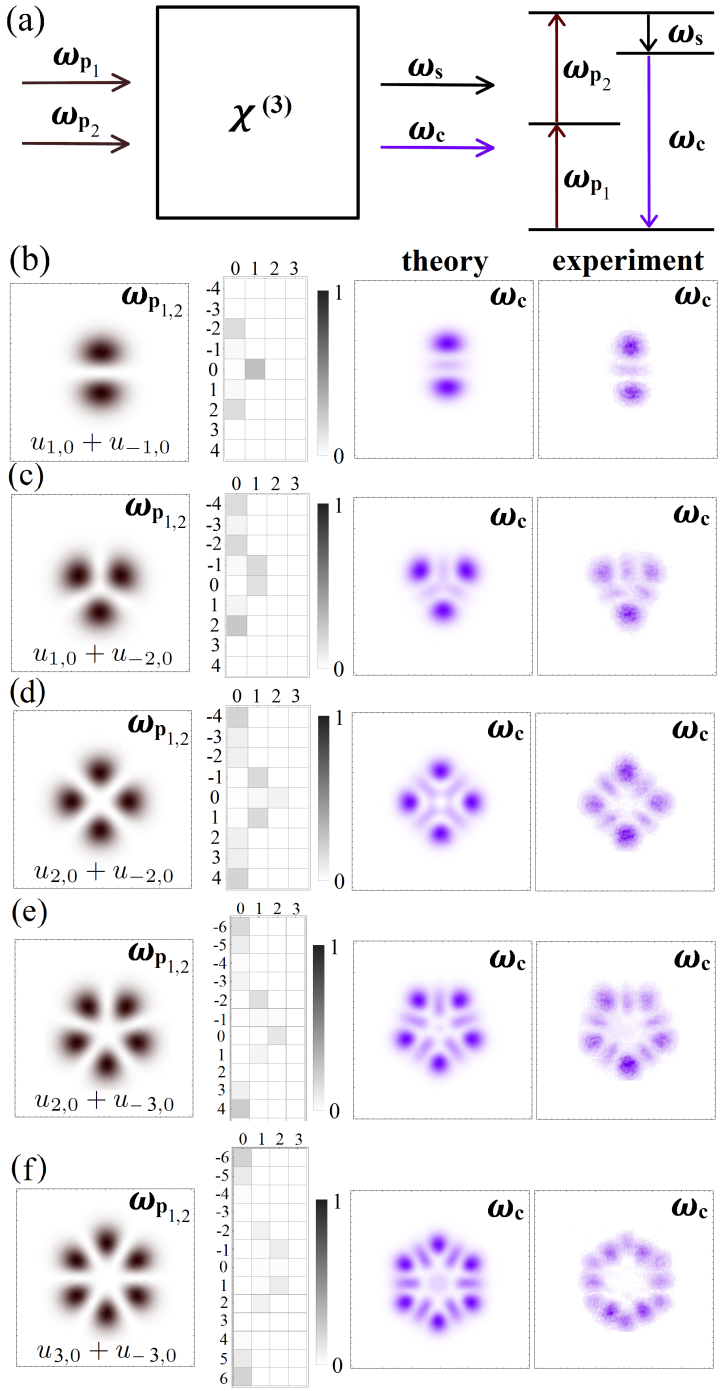

Figure 5.2. (a) Non-degenerate four-wave mixing scheme, which occurs in ^{87}Rb, (b)–(f) results of nonlinear interaction for different pump profiles; from left to right the columns correspond to the profile of the pump beams, a histogram giving the mode structure of the conjugate beam, the spatial profile of the conjugate beam, and lastly an experimental realization from Ref. [17]. A better qualitative agreement is observed when ω_s is allowed to take on any mode conserving OAM.

that a more careful analysis, such as the one we present here, is necessary when studying the mode structure of output beams, since a naive examination of the lobe structure can be very misleading.

We now transition from simulations of experiments which help to validate our theory, to more predictive simulations. We will show how our theory can be used as a tool to optimize the mode structure for other OAM addition, subtraction, and cancellation processes. The theme of these simulations is to develop methods which enhance the mode structure of the generated beams. They also serve as predictions which can be verified experimentally, relatively easily.

5.3 Second-Harmonic Generation

First we present a simulation for second-harmonic generation. An 1140-nm pump beam, with waist $w_0 = 0.1$ mm, interacts with a 3-mm long crystal to create a second-harmonic beam at 570 nm. The waist of the basis set, used to represent the generated beam, is set to match the waist of the pump beams (this suggests the waist to target during detection). The light-matter interaction in the crystal, depicted in Fig. 5.3(a), is governed by the polarization

$$\mathcal{P}(2\omega)^{(2)} = \epsilon_0 \chi^{(2)} \mathcal{E}(\omega_1)\mathcal{E}(\omega_2), \tag{5.8}$$

where the argument of the the polarization $\mathcal{P}$ is 2ω, indicating the second harmonic response, and the angular frequency of each field $\mathcal{E}$ indicates the distinct beam.

We first consider that two photons are annihilated from a single pump beam in the superposition $u_{1,0} + u_{-1,0}$, and the results are given in Fig. 5.3(b). One can see that along with the response at $\ell = \pm 2$, there is also response at $\ell = 0$, corresponding the cross terms in $(u_{1,0} + u_{-1,0})^2$. One can enhance the OAM transfer by creating a destructive interference to remove the response at $\ell = 0$. This can be done by including a second pump beam, according to the geometry in Fig. 5.3(c), with a π phase shift in the superposition, that is, a rotated profile. The conservation of linear momentum dictates that, in order to have a

response at 2ω in the geometry of Fig. 5.3(c), a photon must be annihilated from each pump beam. As one can see in Fig. 5.3(d), this geometry (along with the phase shift) suppresses the response at $\ell = 0$ and provides a cleaner mode structure. This technique can be quite useful and can be implemented in more complex situations, as we will show in the following examples.

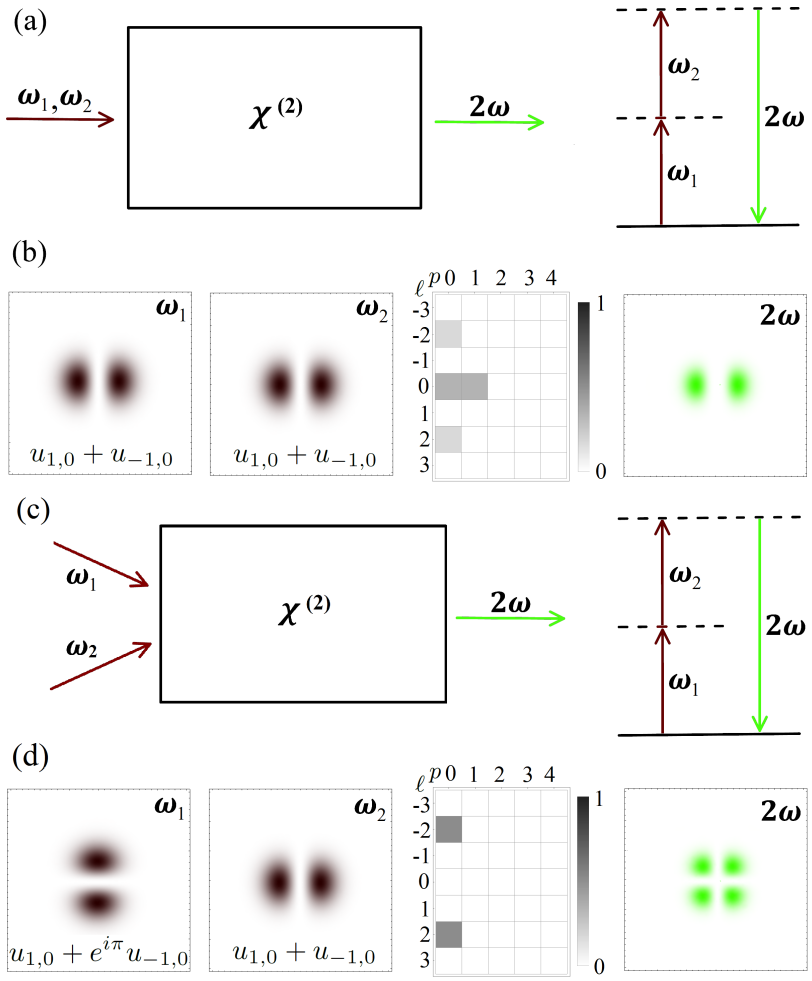

Figure 5.3. (a,c) Depiction of the the two second-harmonic generation schemes of our simulation. In (b) and (d) we show the input-beam profile, which is supplying the two pump photons, a histogram giving the mode structure of the output beam, and the spatial profile of the output beam, respectively. In (b) both pump photons come from a $u_{1,0} + u_{-1,0}$ superposition. In (c) and (d), a phase shift and a new geometry is chosen such that destructive interference cancels the response at $\ell = 0$ [seen in (b)]. The pump photons are in the far-infrared at 1140 nm, and thus the 2nd harmonic response is at 570 nm.

5.4 Third-Harmonic Generation

Next, we present a simulation for third-harmonic generation. An 1140-nm pump beam, with waist $w_0 = 0.1\,\text{mm}$, interacts with a 3-mm long crystal to create a third-harmonic beam at 380 nm. The light-matter interaction in the crystal, depicted in Fig. 5.4(a), is governed by the polarization

$$\mathcal{P}(3\omega)^{(2)} = \epsilon_0 \chi^{(2)} \mathcal{E}(\omega_1)\mathcal{E}(\omega_2)\mathcal{E}(\omega_3), \tag{5.9}$$

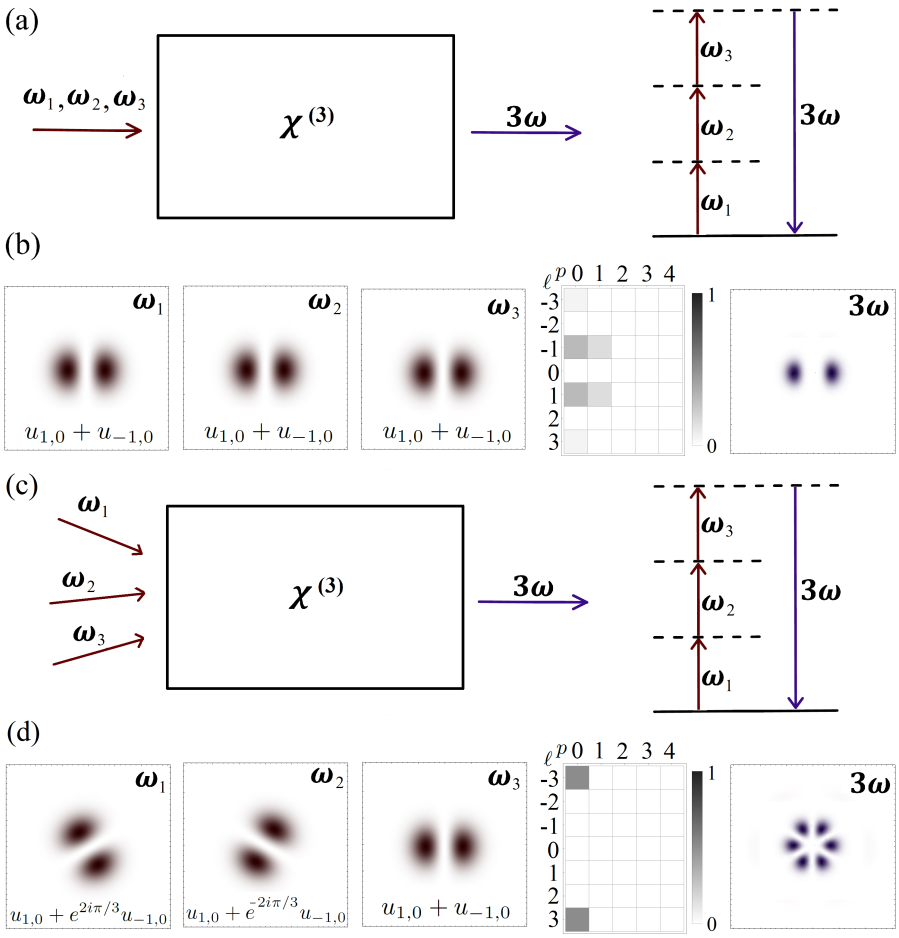

Figure 5.4. (a,c) Depiction of the two simple third-harmonic generation schemes of our simulation. In (b) and (d) we show the input-beam profiles, which are supplying the three pump photons, a histogram giving the mode structure of the output beam, and the spatial profile of the output beam, respectively. In (b) all pump photons come from a $u_{1,0} + u_{-1,0}$ superposition. In (c) and (d), phase shifts and a new geometry is chosen such that destructive interference cancels the response at $\ell = \pm 1$ as seen in (b). The pump photons are in the far-infrared at 1140 nm, and thus the 3rd harmonic response is at 380 nm.

where the argument of the the polarization $\mathcal{P}$ is 3ω, indicating the third harmonic response, and the angular frequency of each field $\mathcal{E}$ indicates the distinct beam. As in the previous simulation, we first consider that three pump photons are annihilated from a single pump beam in the superposition $u_{1,0} + u_{-1,0}$, and the results are given in Fig. 5.4(b). One can see from the histogram that, along with the response at $\ell = \pm 3$, there is also response at $\ell = \pm 1$, corresponding the cross terms in $(u_{1,0} + u_{-1,0})^3$. To clean up the OAM transfer, one needs to create an interference to destroy the response at $\ell = \pm 1$. We deploy the same tactic as in the SHG simulation, but in this case include three pump beams, two of which have the phase shift $\pm 2\pi/3$ between the two modes. One can see in Figs. 5.4(c) and 5.4(d) that if one photon is annihilated from each of the three pump beams, that the response at $\ell = \pm 1$ is destroyed and a clean OAM transfer is established. Again, as we described in the previous subsection, one could realize this result by judiciously choosing the angles of the incident beams according to conservation of linear momentum, such that the generated beam is aligned along the z axis. So we see that this can be a very useful technique for the up-conversion of OAM, especially in the absence of a cavity, which would naturally clean the mode structure.

5.5 Four-wave Mixing

Next, we present a simulation for degenerate four-wave mixing, depicted in Fig. 5.5(a), in which we demonstrate the addition, subtraction, and cancellation of OAM. Two 650-nm pump beams and a signal beam interact in a 7-cm long nonlinear cell to create a conjugate beam according to the polarization

$$\mathcal{P}(\omega_c)^{(3)} = \epsilon_0 \chi^{(3)} \mathcal{E}(\omega_p) \mathcal{E}(\omega_p) \mathcal{E}(\omega_s)^*, \tag{5.10}$$

where ω_p and ω_s are the angular frequencies of the pump and signal photons respectively. We now investigate ways to tailor the response of the conjugate beam. In both cases the pump beams remain in the form $u_{1,0} + u_{-2,0}$ and $u_{1,0} + e^{i\pi} u_{-2,0}$, and we choose to vary

the signal beam. We showed in the previous two simulations that, when the pump beams are properly rotated with respect to each other, that cross terms can be canceled, that is, response at $\ell = -1$ is suppressed. Therefore, if the seed beam were simply a $u_{0,0}$, then the conjugate beam would respond at $\ell = 2$ and $\ell = -4$, as we see in Fig. 5.5(b). However, suppose we would prefer the field to respond at $\ell = \pm 3$, then we would choose the signal to be in a $u_{-1,0}$ mode and effectively add another unit of angular momentum to the conjugate beam, as seen in Fig. 5.5(c). This approach can be taken to the extreme by choosing the

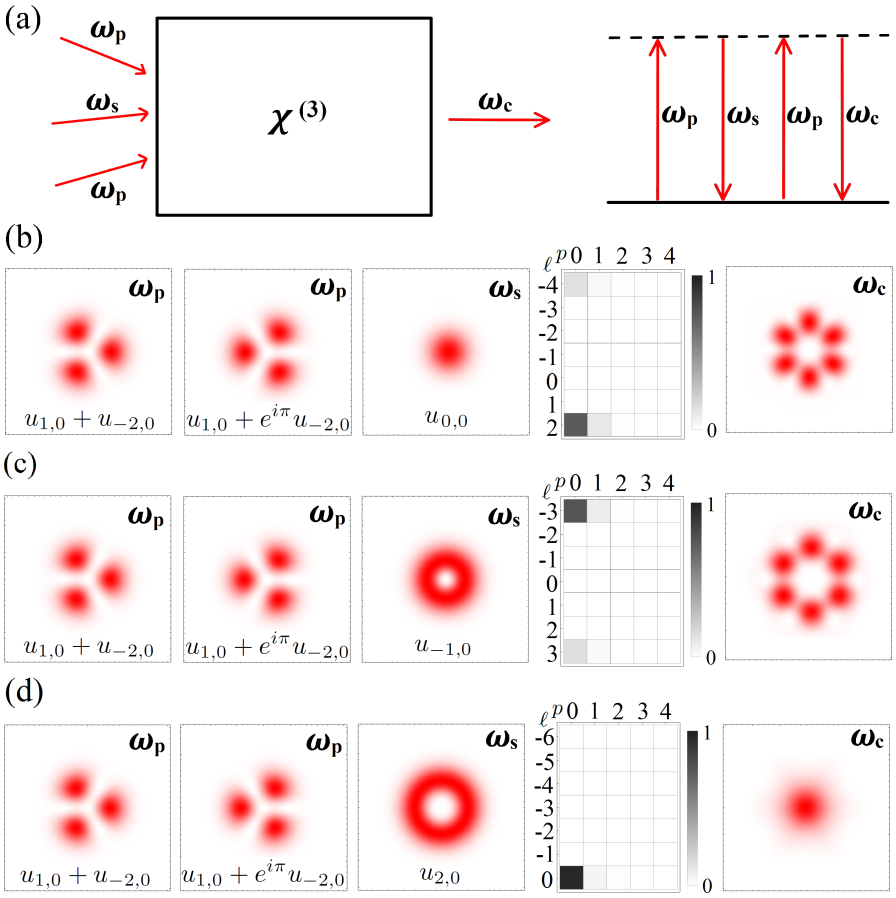

Figure 5.5. (a) Depiction of the simple degenerate four-wave mixing scheme of our simulation. In (b) through (d) we show the pump-beam profiles, the signal-beam profile, a histogram giving the mode structure of the output (conjugate) beam, and the spatial profile of the output (conjugate) beam respectively. In (b) the pump beams are of the form $u_{1,0} + u_{-2,0}$ and $u_{1,0} + e^{i\pi}u_{-2,0}$ and the signal beam is a $u_{0,0}$ mode. In (c) the pump beams remain the same and the signal beam is a $u_{-1,0}$ mode. In (d) the pumps stay the same but the signal beam is changed to $u_{2,0}$. This is a degenerate scheme and all beams are 650 nm.

seed to be in a $u_{2,0}$ mode, and effectively subtracting two units of angular momentum from the conjugate beam, as seen in Fig. 5.5(d). In this case, response at $\ell = 0$ and $\ell = -6$ are the two modes allowed by OAM conservation. However, we see that response at $\ell = -6$ is naturally suppressed. This is because even though $\ell = -6$ is a potential OAM pathway, the mode overlap is so poor that exciting this mode is extremely unlikely. Thus, we expose one more, of possibly many ways, to completely suppress OAM transfer into unwanted modes.

6 Simulations — Spontaneous Nonlinear Interactions

In this chapter we use our second quantization theory to show how one can understand the complex TSM mode structure stimulated during nonlinear-optical interactions. In fact, some interactions may not require the full capability of our theory. To that end, we simulate several interactions, progressing from simple to complex, demonstrating the utility of this theory as a powerful analysis tool.

6.1 Four-Wave Mixing

First, we investigate the polarization self-rotation effect observed in ^{87}Rb (see Fig. 6.1). We began this study in Section 4.2. There, we worked out the second quantization procedure to simulate PSR and model our experimental findings. In this Chapter, we are working out more predictive simulations, but we start with PSR again because it serves as a stepping stone to investigating other FWM and DC processes. Furthermore, it shows how to take our general second quantization process, and implement it for a particular nonlinear interaction model. Therefore, in this Chapter we will be extremely careful to show how slight changes in the model result in changes to the interaction and correlations between the TSM's. Once these ideas have been established, we will transition to showing how beam parameters and beam composition can manipulate the quantum properties of the spontaneously generated beams. But first, we will contrast the single- and two-photon resonant interactions in FWM.

6.1.1 PSR with Single-Photon Resonance

The first and simplest case to consider is the single-photon resonance scheme in Fig. 6.1(b). Since the photons scattered into the x polarization are separated by a y-polarization excitation, it is reasonable to assume that the two x-polarization photons do not have transverse-spatial-mode correlations, that is, there is no cross talk between the two-photon emissions. As we did in Section 4.2, we take Eq. (3.20), let $\hat{\boldsymbol{b}} \rightarrow \hat{\boldsymbol{a}}$ and thus have a single-spatial-mode

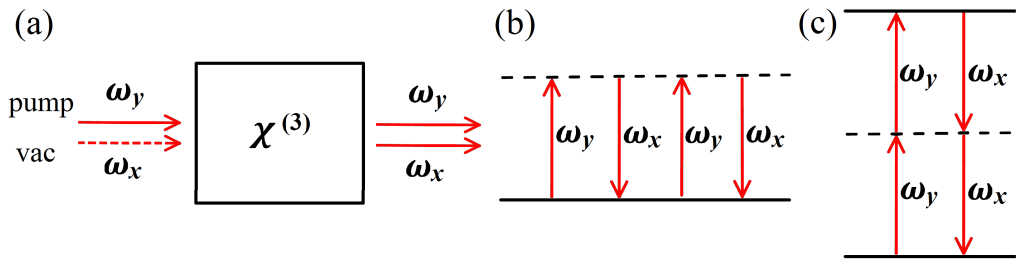

Figure 6.1. Setup and energy diagrams describing the PSR effect in ^{87}Rb. In (a) we show a linear polarized pump beam interacting with vacuum fluctuations in the orthogonal polarization. Two tensor elements of the semiclassical susceptibility tensor survive: (b) depicts the single-photon resonance associated with the χ_{xyxy} element, that is, a response in x due to stimulation in yxy, and (c) describes the two-photon resonance associated with the χ_{xyyx} element, that is, a response in x due to stimulation in yyx. The input and output fields are co-propagating.

squeezer. This led to a diagonal squeezing matrix with elements given by

$$\xi_p = \int d^3\boldsymbol{r}\, C\, \chi^{(3)}\, A_y^2 \left(u_{0,0}(\mathbf{r})\, u_{0,p}^*(\mathbf{r})\right)^2, \tag{6.1}$$

and thus we know $\xi_p = r_p e^{i\theta_p}$, where $r_p = |\xi_p|$. We use this calculation as a baseline simulation with which to compare the more sophisticated interactions. Thus, we scale the strength of the interaction such that $\bar{n} = 1$, and examine how $\bar{n}$, $\Delta\hat{\boldsymbol{X}}_1$, $\Delta\hat{\boldsymbol{X}}_2$, and $\boldsymbol{M}_{a\leftrightarrow b}$ change in each case.

For the first simulation, we assume a 795-nm pump beam, in a $u_{0,0}$ mode with a 80-μm waist, is focused at the center of a $3z_R$ long nonlinear cell. First, we will examine the quadrature noise matrices [see Fig. 6.2(a)]. As a visualization tool, the plots along the diagonal represent the quadrature noise. The gray Gaussian represents the projection of the multimode Wigner function onto the particular TSM quadrature. The dashed black Gaussian is the projection of the vacuum Wigner function and serves as a reference. Thus we can quickly observe how the noise suppression, if at all, is distributed among the spatial modes, and the inset number gives the amount of squeezing given in dB. The off-diagonal elements of the quadrature matrices are the covariance, and the strength of covariance is given by the color map in the bar legend. As expected, there is no response in $\ell \neq 0$

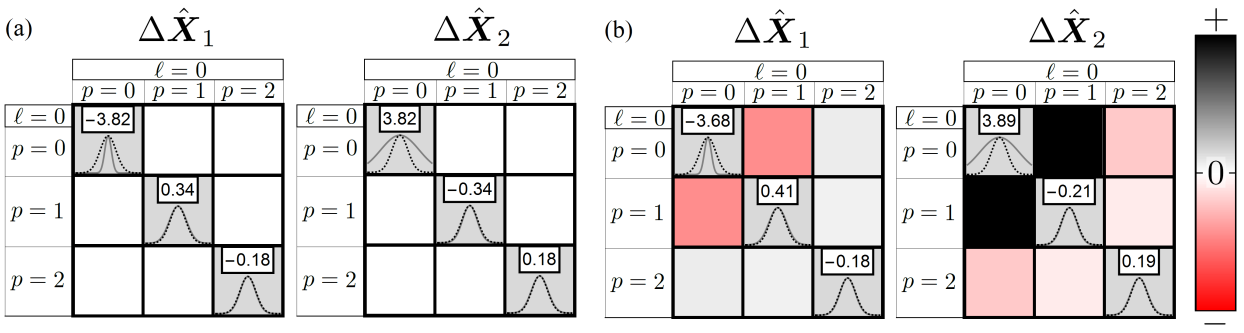

Figure 6.2. PSR noise matrices for the single-spatial-mode quadratures $\hat{\boldsymbol{X}}_1$ and $\hat{\boldsymbol{X}}_2$, in (a) the absence of TSM cross talk and (b) with p-mode cross talk. The noise in the quadrature is depicted along the diagonal as the projection of the multimode Wigner function onto the particular TSM quadrature. The dashed black Gaussian is the projection of the vacuum state, thus the diagonal elements allow one to quickly observe how the noise suppression, if at all, is distributed among the spatial modes. The inset number is the amount of squeezing given in dB. The off-diagonal elements represent the covariance between different spatial modes in the quadrature. In (a) there is no cross talk between the x-polarization modes, thus the covariance is zero. In (b) the p-mode cross talk is present and indicated by the nonzero off-diagonal elements.

modes, and we see a slight amount of squeezing in the higher-order p modes, but it is mostly concentrated in the $u_{0,0}$ mode. But what if cross talk between the p modes is taking place? There would still be no azimuthal structure to detect, but there would indeed be a more complex p-mode structure that will effect the squeezing in the system.

Next, we allow for cross talk between p modes in the x polarization. Mathematically, this means we now accommodate for the two spatial modes $\hat{\boldsymbol{a}}$ and $\hat{\boldsymbol{b}}$, as in Eq. (3.20), and insert the restriction $\delta_{\ell,m}$. Furthermore, this provides for the off-diagonal elements of the squeezing matrix, which now has elements

$$\xi_{p,q} = \int d^3\boldsymbol{r}\, C\, \chi^{(3)}\, A_y^2 \left(u_{0,0}(\mathbf{r})\right)^2 u^*_{0,p}(\mathbf{r})\, u^*_{0,q}(\mathbf{r}), \tag{6.2}$$

where one should recall that p and q correspond to the radial index of $\hat{\boldsymbol{a}}$ and $\hat{\boldsymbol{b}}$ respectively. In Figure 6.2(b) we show the quadrature noise matrices for this simulation. Although subtle in the figure, there is actually $\sim 3\%$ increase in quadrature noise in the $u_{0,0}$ squeezed mode and $\bar{n} \sim 1.14$. This trend agrees with previous findings, that in general the population

of higher-order modes will deteriorate the performance of non-classical processes, including squeezing [1]. Furthermore, we now observe covariance between TSMs, the color indicating whether the variances are positively or inversely related. It is also noteworthy that now, there is not an effective squeezing parameter for each mode. Rather, all we know is the projection of the multimode Wigner function on the respective quadrature, given along the diagonal of the variance-covariance matrix. The modes are potentially entangled, and this is the focus of our current research. Now, we can only observe the amount of correlations between the modes in each quadrature, which is a prelude to examining the coupling strength quantified by the coupling matrix $\boldsymbol{M}_{a\leftrightarrow b}$. This we save for the next section, where we show that the mode structure is in general much more complicated, by simulating a general four-wave-mixing scheme with a two-photon resonance.

6.1.2 FWM with Two-Photon Resonance

The two-photon resonance in Fig. 6.1(c) will lead to a more complicated mode structure, since the two x-polarized photons are emitted in cascade, permitting full cross talk. For example, it is well known that even when the pump beam carries no OAM, the scattered photons can in principle carry opposite ℓ, thus conserving OAM. This of course happens much less frequently than excitation in the $u_{0,0}$ mode, which dominates because of the ideal overlap with the pump. Our theory allows us to investigate this complicated mode structure.

The squeezing matrix is much more complicated now, but we will evaluate an element as an example. Let us examine $\xi_{7,2}$ which is given by Eq. (3.18):

$$\xi_{7,2} = \int d^3\boldsymbol{r}\, C\, \chi^{(3)}\, A^2 \left(u_{0,0}(\mathbf{r})\right)^2 u^*_{1,1}(\mathbf{r})\, u^*_{-1,2}(\mathbf{r}), \tag{6.3}$$

where $\ell_{\max} = m_{\max} = 3 = p_{\max} = q_{\max}$. Thus, we see that this element corresponds to the interaction of the the (1,1) mode in $\hat{\boldsymbol{a}}$ and the (-1,2) mode in $\hat{\boldsymbol{b}}$. Once the full matrix is constructed, it is relatively simple to find the left-polar decomposition $\boldsymbol{\xi} = \boldsymbol{R}\exp(i\boldsymbol{\Theta})$, and

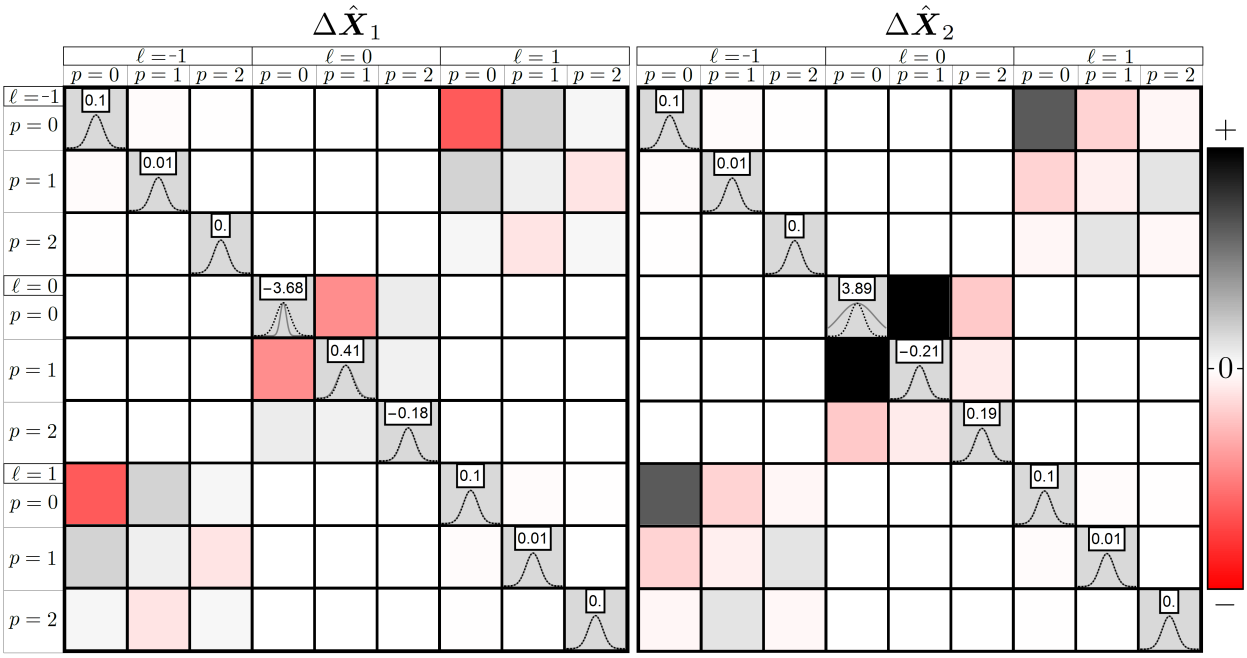

Figure 6.3. Noise matrices for the joint quadratures $\hat{\boldsymbol{X}}_1$ and $\hat{\boldsymbol{X}}_2$, when full cross talk is present in a two-photon-resonance scheme. The noise in the quadrature is depicted by the solid Gaussian along the diagonal, and the off-diagonal elements represent the covariance between different spatial modes in the quadrature. Red is negative, white is zero, and black is positive covariance. The inset gives the squeezing in dB.

use the formula in Eq. (3.28) to find the variance matrices. As expected, this simulation shows a response at $\pm\ell$ along with the p-mode structure (see Fig. 6.3). Surprisingly, there is no increase in noise of the $u_{0,0}$ mode despite the more complicated structure, and the average photon number increasing to $\bar{n} = 1.25$. Another qualitative observation is the obvious correlation between positive covariance with the noisy quadrature, and negative covariance with the squeezed quadrature. It seems that overall cooperative noise fluctuations in quadrature correspond directly to excess noise, whereas opposing noise fluctuations among the spatial corresponds to noise suppression.

In Figure 6.4(a) we plot a histogram of the photon-creation matrix $\boldsymbol{M}_{a\leftrightarrow b}$ given by Eq. (3.37). It shows the mode structure of the quantum beam and identifies which *pairs of modes* are most likely to be populated. Response along the diagonal indicates that the photon pair are created in identical TSMs. Contrastingly, off-diagonal response indicates that photon pairs can be excited in different TSMs. In Fig. 6.4(b) we plot a histogram

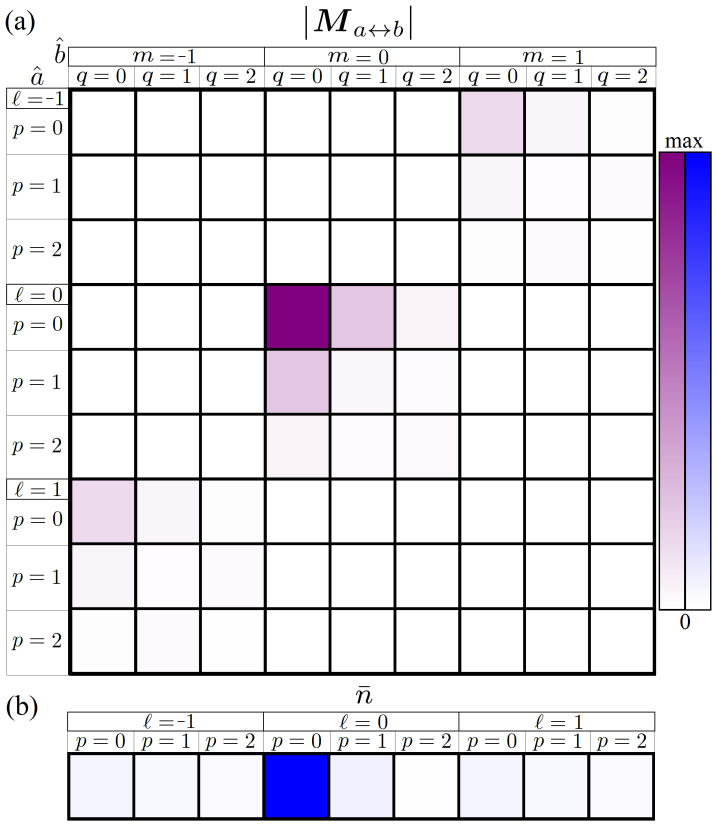

Figure 6.4. (a) Photon-creation matrix given by Eq. (3.37) and (b) the average photon number per mode for degenerate four-wave-mixing in a two-photon resonant scheme where full TSM cross talk is present. For the blue scale, max= 1.25.

of the diagonal elements of $\langle \boldsymbol{n} \rangle \equiv \langle \hat{\boldsymbol{a}}^\dagger \widetilde{\hat{\boldsymbol{a}}} \rangle$, that is, $\bar{n}$ per mode. This is a relatively simple system and the parameters of the interaction have already been optimized for concentrating squeezing in a single mode, that is, the mode structure, beam waist, and focal position. In general, there will be much more cross talk and this theory can be used as a tool to tailor the quantum-mode structure. Furthermore, this type of analysis is a very convenient tool for systems heralding a single photon, or creating an indistinguishable or entangled photon pair. However, knowing which mode is squeezed the most, or which mode has more photons on average, will not necessarily allow one to maximize the performance of their process. For this we will simulate a parametric-down-conversion process and show how one can recover from the negative effects of the higher-order mode structure.

6.2 Parametric Down Conversion

In this section, we simulate type-II down-conversion of 405-nm light into two 810-nm photons [see Figs. 6.5(a) and 6.5(b)]. Ideally, the down-converted photons would share the same transverse-spatial mode as the pump photon. As a visual reference, in Fig. 6.5(c) we plot the quadrature noise for an idealized two-mode-squeezed vacuum state with $\bar{n} = 1$. We know however that things are not so simple. In actuality, there is a complex interaction among the transverse-spatial modes.

To demonstrate this, we simulate this interaction, allowing full cross talk among the spatial modes, but scaling the overall strength of the nonlinearity such that $\bar{n}$ remains one. In this way, we can see how the noise suppression may leak into the other transverse spatial

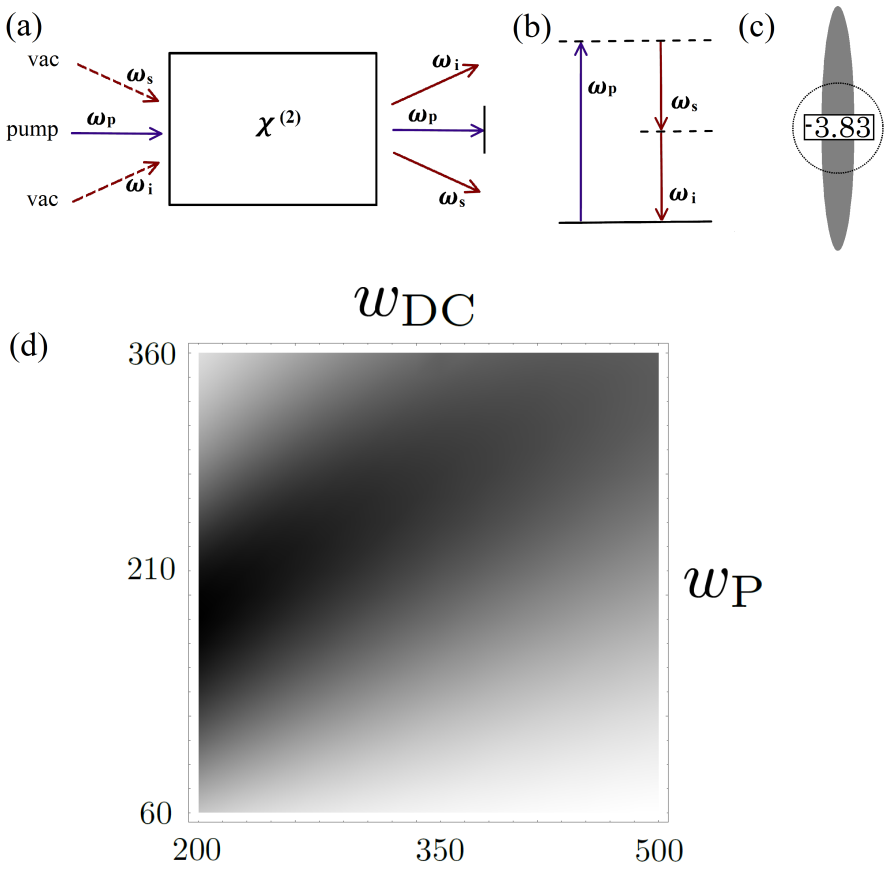

Figure 6.5. (a) Schematic of our PDC simulation, (b) energy level diagram, (c) noise ellipse of an ideal squeezed state with $\bar{n} = 1$ (inset gives squeezing in dB), and (d) density plot (μm), discussed in the main text . The density plot reveals a parameter island where (0,0) coupling is dominant *and* most of the down-converted photons are sent to the $0, 0$ mode.

modes. To set a benchmark, we must choose the pump beam waist and the DC photon collection waist to investigate. Suppose then that we want to find the combination of waists that has the strongest response in the $u_{0,0}$ mode. To do so we calculate $|M_{00}|/\sum_{i,j}|M_{ij}| \times n_{00}/\sum_i n_{ii}$, where M_{ij} and n_{ij} are matrix elements of $\boldsymbol{M}_{a\leftrightarrow b}$ and $\boldsymbol{n}$ respectively. Varying the pump and DC waists over a wide experimental range, we find the results, in Fig. 6.5(d), which reveal an optimal parameter region. Thus, we choose $w_{\mathrm{P}} = w_{\mathrm{DC}} = 200$ μm as our benchmark simulation. In the following, we limit the LG parameters to $-1 \leq \ell \leq 1$ and $0 \leq p \leq 2$ for display purposes.

In Fig. 6.6(a) we show the noise matrices for the joint quadratures $\hat{\boldsymbol{X}}_1$ and $\hat{\boldsymbol{X}}_2$ using the optimal waists. One can see that the noise and covariance are qualitatively similar to the two-photon resonant simulation in Fig. 6.3. However, the squeezing has leaked into the higher-order modes more drastically. Furthermore, in Figs. 6.7(a) and 6.7(b) we see that the cross talk between the modes has also been enhanced, but this is not necessarily a good thing. For example, in a homodyne measurement, the observed noise suppression will just be the sum of all the noise from each mode that overlaps the local oscillator (see Section 1.4). Thus, leakage into higher-order modes can be detrimental to noise suppression as a resource. To recover from this leakage, one can projectively filter out the modes with the most squeezing. For example, we can see that the $u_{0,0}$ mode has the most squeezing, and thus a naive approach might use a single mode fiber to isolate this mode. However, better squeezing can be extracted by using the eigenmodes of squeezing.

Employing our theory in Sec. 3.2.4, we can find the collection of transverse spatial modes which have quadrature noise suppression beyond what is observed in the $u_{0,0}$ mode alone. This is possible because our choice of quadratures was somewhat arbitrary, in other words, it does not take into account the squeezing parameter and squeezing angle of each mode. The eigenmode approach, in effect, judiciously chooses the proper quadrature measurement for each transverse-spatial mode, and thus improves the observed noise suppression. This approach may seem mysterious, but the alternative of calculating the Wigner function for

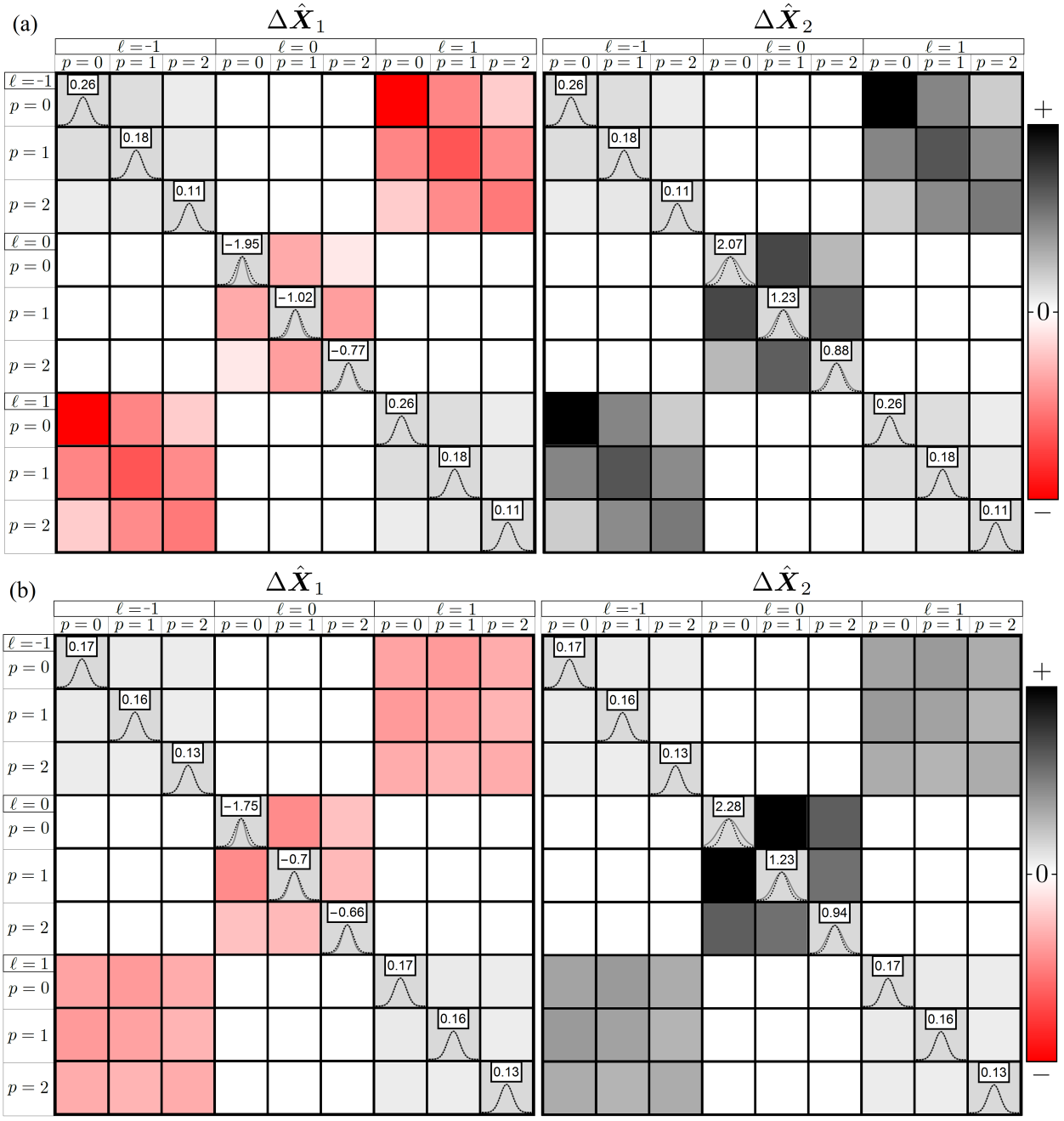

Figure 6.6. (a) Noise matrices for the joint quadratures $\hat{\boldsymbol{X}}_1$ and $\hat{\boldsymbol{X}}_2$, when full cross talk is present in a type-II PDC scheme, and (b) the noise matrices when the crystal is pumped by the first eigenmode. In (a), although $\bar{n} = 1$, we can see a reduction in the maximum squeezing performance, compared the ideal situation of only a single transverse spatial mode. In (b) we see that the squeezing changed marginally but the covariance elements experienced the most significant change. This suggests the mode coupling has been altered, and this can be seen clearly by comparing Figs. 6.7 and 6.8(a). We limit $-1 \leq \ell \leq 1$ and $0 \leq p \leq 2$ for display purposes.

this multimode Gaussian squeezed state is quite a difficult problem, and an open area of research in itself. Thankfully, the noise suppression in each eigenmode obeys the canonical two-mode squeezed-vacuum equation, thus we can plot the actual noise ellipse for each of the eigenmodes $\Delta\hat{\boldsymbol{X}}_\lambda$, along with the average photon number per eigenmode $\bar{n}_\lambda$ [see Fig. 6.7(c)]. The variance $\Delta\hat{\boldsymbol{X}}_{\lambda=1} \sim 0.28$ as compared to 0.32 in the $u_{0,0}$ mode, a ~ 0.6 dB reduction. Therefore, one can access an increased amount of noise suppression by detecting the λ_1 eigenmode.

Next we will investigate how pumping the crystal with an eigenmode effects the noise suppression and mode structure. The largest eigenvalue is λ_1; thus we use this eigenmode for our simulation. Mathematically, we prepare the pump beam in the superposition $\sum_i [\boldsymbol{U}^\dagger \boldsymbol{u}]_{1i}$, where $\boldsymbol{u}$ is a vector of LG modes with the same structure as Eq. 3.17. In Fig. 6.6(b) we show the noise matrices for the joint quadratures $\hat{\boldsymbol{X}}_1$ and $\hat{\boldsymbol{X}}_2$. The most striking change is the covariance, which has become mostly uniform over all the modes. Furthermore, we see that there has not been any increase in noise suppression in any of the LG modes individually. However, in Fig. 6.7(d) we see how the tailored pump beam can increase the amount of noise suppression in the first few eigenmodes, and shift each $\bar{n}_\lambda$ toward the first eigenmode. Now, the variance is $\Delta\hat{\boldsymbol{X}}_{\lambda=1} \sim 0.23$ as compared to 0.32 in the $u_{0,0}$ mode initially, a ~ 1.4 dB reduction.

The change in mode structure is best understood by comparing the photon creation matrices in Fig. 6.7(a) and Fig. 6.8(a). In Figure 6.8(a) we see that response in the $\ell = \pm 1$ modes has been suppressed, and the coupling in the $\ell = 0$ modes has been enhanced. Furthermore, we see that $\bar{n}$ per mode has shifted toward the $u_{0,0}$ mode. The same is true for pumping with other eigenmodes, except the shifts may be different. For example, pumping with the λ_3 eigenmode enhances the coupling of the $\ell = \pm 1$ modes and suppresses $\ell = 0$. This exercise demonstrates that even if the eigenmodes can't be collected, they can suggest ways to change the pump beam to tailor the mode structure of the DC twin beam.

Next, suppose that we want to maximize the heralding efficiency in a PDC experiment

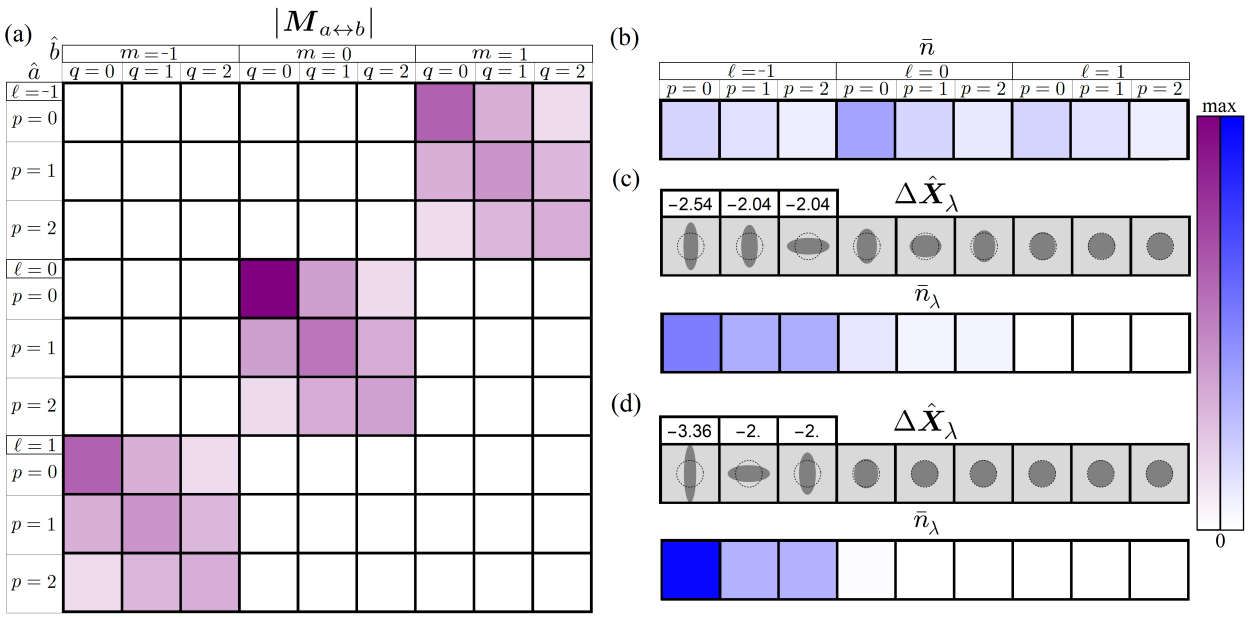

Figure 6.7. (a) Photon creation matrix given by Eq. (3.37), (b) the average photon number per mode for our PDC scheme [corresponding to Fig. 6.6(a)], and (c,d) the noise ellipses and average photon number for each of the eigenmodes of squeezing, progressing from left to right, starting with λ_1. In (c) the crystal is pumped with a $u_{0,0}$ mode and in (d) with the λ_1 eigenmode [corresponding to Fig. 6.6(b)]. In (d) we observe an increase in the amount of noise suppression and a shift in the concentration of $\bar{n}_\lambda$ toward the first eigenmode. The blue scale is set to max= 0.75 for (b)–(d).

using single-mode fibers. Then for every (0,0) photon that is detected in the $\hat{\boldsymbol{a}}$ mode, we need a matching (0,0) photon in the $\hat{\boldsymbol{b}}$ mode. Now, take the previous PDC simulation as an example. Examining Fig. 6.8(a), we see that that if a (0,0) photon in the $\hat{\boldsymbol{a}}$ mode heralds a photon in the $\hat{\boldsymbol{b}}$ mode, there is a significant chance that it will actually be a higher order p mode. Therefore, it would be rejected by the single-mode fiber and suppress the heralding efficiency.

So we see that we need to judiciously choose the pump mode structure and collection waist to suppress the off-diagonal elements. To do so, we find that we can pump with a $u_{0,0}$ mode, and increase the waist to 400 μm, keeping the collection waist at 200 μm. As we see in Fig. 6.8(c), doing so suppresses the off-diagonal elements, but it is at the expense of drastically increasing the coupling to higher order modes. In fact, the coupling extends far outside the range of this plot, up to $p = 20$. Furthermore, in Fig. 6.8(d) we see that the $u_{0,0}$

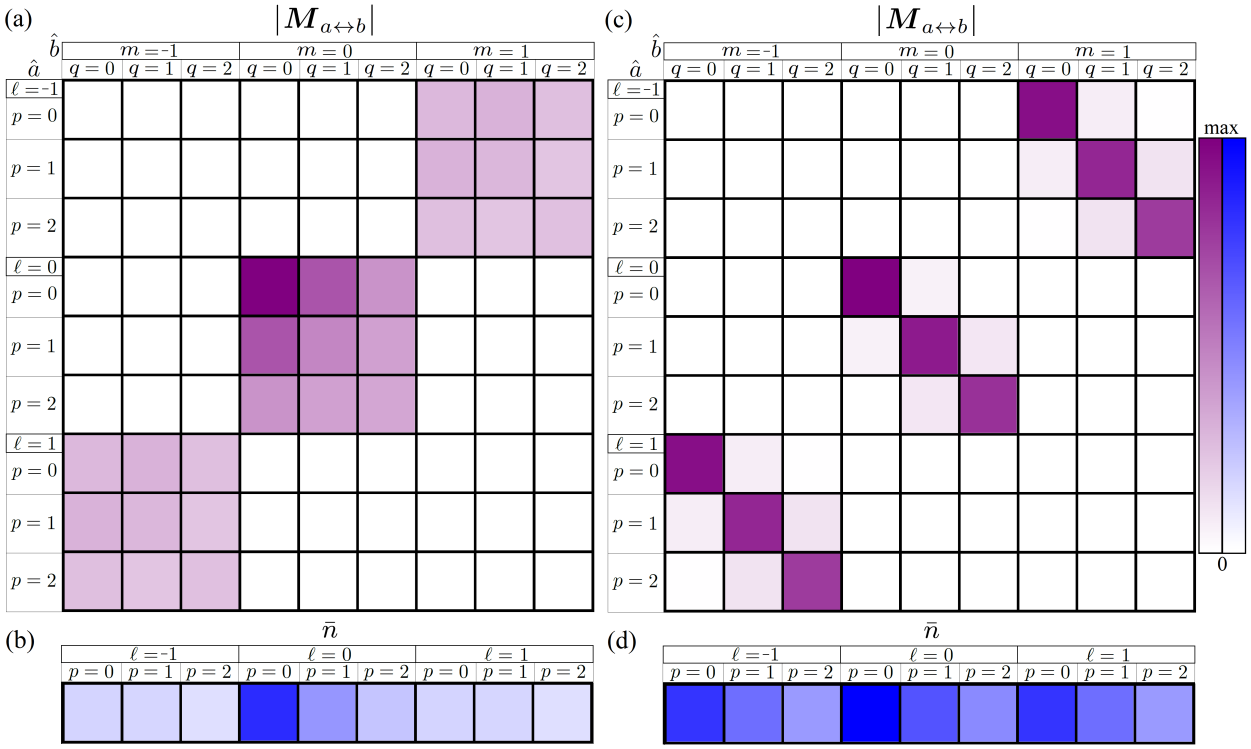

Figure 6.8. (a) Photon-creation matrix given by Eq. (3.37) and (b) the average photon number per mode when the crystal is pumped with the λ_1 eigenmode. In (c) and (d) the pump mode is a $u_{0,0}$ mode but the waist has been increased to 400 μm. This configuration is ideal for heralding efficiency since it suppresses the of off-diagonal coupling. In other words, it insures that the photon pair are in the same p mode. The blue scale is set to max= 0.5 for (b) and max= 0.1 for (d).

mode no longer dominates the interaction. Therefore, concluding our investigation, we see how the heralding efficiency can be enhanced at the expense of the heralding rate. Although this result is not new, it provides different theoretical explanation and insight to this body of work.

7 Conclusion

We report a general theory for calculating the spatial mode structure of beams generated during nonlinear interactions. We accomplish this by making a first-order Born approximation to the inhomogeneous paraxial wave equation. Therefore, it is akin to the weak scattering problem of the nonlinear Schrödinger equation. The theory is general in the sense that, it may be implemented for any complete orthonormal set of spatial mode functions. We use the theory to simulate orbital angular momentum transfer in several nonlinear optical processes, with an emphasis on analyzing and tailoring the resulting mode structure for optimal performance. This includes the processes of orbital angular momentum addition, subtraction, and cancellation in harmonic generation, parametric down conversion, and four-wave mixing.

The first-order Born approximation has limitations. In general, it is only valid for input light which is sufficiently weak, such that the nonlinearity is small. Additionally, it may only be adequate for thin slabs and dilute vapors of nonlinear media, and for scenarios in which the pump beams are assumed to be undepleted, and the spatial structure unaltered. However, we describe how successive iterations of the Born approximation can be performed using our theory. Although this theory is based on a first-order approximation, we show that it can model the mode structure of experimental data remarkably well.

In doing so we are able to show that a naive analysis of the lobe structure in intensity patterns can be very misleading. One may be tempted to assume, based on lobe structure, that OAM transfer is limited to certain pathways. However, our analysis shows that the rich mode structure resulting from a more complete consideration of all the pathways, actually accounts for symmetries in the resulting beam pattern. On a final note, this validation of the theory is assurance that the theory is accurately predicting the classical mode structure, which can in turn be used for second-quantized treatments of these interactions.

To make our theory even more robust, future work will involve analyzing the efficiency of

tailoring the mode structure, e.g., the ability to suppress higher-order modes, and fine tune the methods we have suggested based upon the strength of the nonlinearity, the intensity of the input light, the angle of incidence, etc. Additionally, for the case of stimulated nonlinear processes, we have shown that the waists of the input beams can be chosen to tailor the mode structure of the generated beam. Thus, it would also be worthwhile to analyze the efficiency of this method as well, and elucidate whether there are trade offs that degrade the performance.

We have also developed a second quantization procedure which predicts the transverse-spatial-mode structure of quantum beams created in nonlinear optical interactions. We used this theory to predict the variance, covariance, and relative coupling strength between the modes. Furthermore, we identify the eigenmodes of the interaction and use these to show how they can be used to enhance the noise suppression observed in the system and manipulate the mode coupling. To utilize the theory, we simulate several interactions, including polarization self-rotation, four-wave mixing, and parametric down-conversion. In each case, we concentrate on exposing the underlying transverse-spatial-mode structure, suggesting ways to tailor it by changing the properties of the pump beam, and enhancing the quantum resources by changing the properties of the detection scheme. The theme of these simulations is enhancing quadrature squeezing or single-photon heralding protocols. In these schemes, optimization typically leads to a simplification of the mode structure, since in general, the cross talk of the modes is detrimental to these processes.

The next step is to investigate how to harness the complicated mode structure instead of suppressing it. Therefore, we will analyze the properties of OAM path entanglement in several spontaneous nonlinear interactions and suggest how this (potentially higher-order) entanglement can be used as a resource. This will be done in two contexts. First, we analyze the connectivity of the state, thus determining the utility in cluster-state quantum computing protocols. Second, we will calculate the entropy of entanglement, which is a signature of entanglement that gives the number of qubits that can be distilled from the

state. Once these quantities are known, we will develop new optimization procedures to show how one can improve the performance of these protocols. In contrast to our previous simulations, this will most likely lead to finding new ways of boosting the cross talk between modes and the connectivity of the entangled state.

References

[1] M. Zhang, R. N. Lanning, Z. Xiao, J. P. Dowling, I. Novikova, and E. E. Mikhailov, "Spatial multimode structure of atom-generated squeezed light," *Phys. Rev. A*, vol. 93, no. 1, p. 013853, 2016.

[2] M. Zhang, M. A. Guidry, R. N. Lanning, Z. Xiao, J. P. Dowling, I. Novikova, and E. E. Mikhailov, "Multipass configuration for improved squeezed vacuum generation in hot rb vapor," *Phys. Rev. A*, vol. 96, no. 1, p. 013835, 2017.

[3] R. N. Lanning, Z. Xiao, M. Zhang, I. Novikova, E. E. Mikhailov, and J. P. Dowling, "Gaussian-beam-propagation theory for nonlinear optics involving an analytical treatment of orbital-angular-momentum transfer," *Phys. Rev. A*, vol. 96, no. 1, p. 013830, 2017.

[4] R. N. Lanning, Z. Xiao, M. Zhang, I. Novikova, E. E. Mikhailov, and J. P. Dowling, "Quantized nonlinear gaussian-beam dynamics—tailoring multimode squeezed-light generation," *Phys. Rev. A*, vol. 98, no. 4, p. 043824, 2018.

[5] L. Allen, M. W. Beijersbergen, R. Spreeuw, and J. Woerdman, "Orbital angular momentum of light and the transformation of laguerre-gaussian laser modes," *Phys. Rev. A*, vol. 45, no. 11, p. 8185, 1992.

[6] A. M. Yao and M. J. Padgett, "Orbital angular momentum: origins, behavior and applications," *Adv. Opt. Photonics*, vol. 3, no. 2, pp. 161–204, 2011.

[7] A. Mair, A. Vaziri, G. Weihs, and A. Zeilinger, "Entanglement of the orbital angular momentum states of photons," *Nature*, vol. 412, no. 6844, p. 313, 2001.

[8] D. Caetano, M. Almeida, P. S. Ribeiro, J. Huguenin, B. C. dos Santos, and A. Khoury, "Conservation of orbital angular momentum in stimulated down-conversion," *Phys. Rev. A*, vol. 66, no. 4, p. 041801, 2002.

[9] J. Courtial, K. Dholakia, L. Allen, and M. J. Padgett, "Second-harmonic generation and the conservation of orbital angular momentum with high-order laguerre-gaussian modes," *Phys. Rev. A*, vol. 56, no. 5, p. 4193, 1997.

[10] Y. Ueno, Y. Toda, S. Adachi, R. Morita, and T. Tawara *Opt. Express*, vol. 17, no. 22, p. 20567, 2009.

[11] R. Pugatch, M. Shuker, O. Firstenberg, A. Ron, and N. Davidson, "Topological stability of stored optical vortices," *Phys. Rev. Lett.*, vol. 98, no. 20, p. 203601, 2007.

[12] V. Boyer, A. M. Marino, R. C. Pooser, and P. D. Lett, "Entangled images from four-wave mixing," *Science*, vol. 321, no. 5888, p. 544, 2008.

[13] M. Cao, L. Zhang, Y. Yu, F. Ye, D. Wei, W. Guo, S. Zhang, H. Gao, and F. Li, "Transfer and conversion of images based on eit in atom vapor," *Opt. Lett.*, vol. 39, no. 9, pp. 2723–2726, 2014.

[14] R. de Oliveira, G. Borba, W. Martins, S. Barreiro, D. Felinto, and J. Tabosa, "Nonlinear optical memory for manipulation of orbital angular momentum of light," *Opt. Lett.*, vol. 40, no. 21, pp. 4939–4942, 2015.

[15] J. Tabosa and D. Petrov, "Optical pumping of orbital angular momentum of light in cold cesium atoms," *Phys. Rev. Lett.*, vol. 83, no. 24, p. 4967, 1999.

[16] D.-S. Ding, Z.-Y. Zhou, B.-S. Shi, X.-B. Zou, and G.-C. Guo, "Linear up-conversion of orbital angular momentum," *Opt. Lett.*, vol. 37, no. 15, pp. 3270–3272, 2012.

[17] G. Walker, A. Arnold, and S. Franke-Arnold, "Trans-spectral orbital angular momentum transfer via four-wave mixing in rb vapor," *Phys. Rev. Lett.*, vol. 108, no. 24, p. 243601, 2012.

[18] G. Gariepy, J. Leach, K. T. Kim, T. J. Hammond, E. Frumker, R. W. Boyd, and P. B. Corkum, "Creating high-harmonic beams with controlled orbital angular momentum," *Phys. Rev. Lett.*, vol. 113, no. 15, p. 153901, 2014.

[19] A. A. Zhdanova, M. Shutova, A. Bahari, M. Zhi, and A. V. Sokolov, "Topological charge algebra of optical vortices in nonlinear interactions," *Opt. Express*, vol. 23, no. 26, pp. 34109–34117, 2015.

[20] A. M. Akulshin, R. J. McLean, E. E. Mikhailov, and I. Novikova, "Distinguishing nonlinear processes in atomic media via orbital angular momentum transfer," *Opt. Lett.*, vol. 40, no. 6, pp. 1109–1112, 2015.

[21] A. M. Akulshin, I. Novikova, E. E. Mikhailov, S. A. Suslov, and R. J. McLean, "Arithmetic with optical topological charges in stepwise-excited rb vapor," *Opt. Lett.*, vol. 41, no. 6, pp. 1146–1149, 2016.

[22] G. Borba, S. Barreiro, L. Pruvost, D. Felinto, and J. Tabosa, "Narrow band amplification of light carrying orbital angular momentum," *Opt. Express*, vol. 24, no. 9, pp. 10078–10086, 2016.

[23] J. D. Swaim, K. N. David, E. M. Knutson, C. Rios, O. Danaci, and R. T. Glasser, "Atomic vapor as a source of tunable, non-gaussian self-reconstructing optical modes," *Sci. Rep.*, vol. 7, p. 42311, 2017.

[24] A. C. Dada, J. Leach, G. S. Buller, M. J. Padgett, and E. Andersson, "Experimental high-dimensional two-photon entanglement and violations of generalized bell inequalities," *Nat. Phys.*, vol. 7, no. 9, pp. 677–680, 2011.

[25] J. Romero, D. Giovannini, S. Franke-Arnold, S. Barnett, and M. Padgett, "Increasing the dimension in high-dimensional two-photon orbital angular momentum entanglement," *Phys. Rev. A*, vol. 86, no. 1, p. 012334, 2012.

[26] R. Fickler, R. Lapkiewicz, W. N. Plick, M. Krenn, C. Schaeff, S. Ramelow, and A. Zeilinger, "Quantum entanglement of high angular momenta," *Science*, vol. 338, no. 6107, pp. 640–643, 2012.

[27] P. Gupta, T. Horrom, B. E. Anderson, R. Glasser, and P. D. Lett, "Multi-channel entanglement distribution using spatial multiplexing from four-wave mixing in atomic vapor," *J. Mod. Opt.*, vol. 63, no. 3, pp. 185–189, 2016.

[28] M. I. Kolobov, *Quantum imaging*. Springer Science and Business Media, 2007.

[29] M. Tsang, "Quantum imaging beyond the diffraction limit by optical centroid measurements," *Phys. Rev. Lett.*, vol. 102, no. 25, p. 253601, 2009.

[30] V. Giovannetti, S. Lloyd, L. Maccone, and J. H. Shapiro, "Sub-rayleigh-diffraction-bound quantum imaging," *Phys. Rev. A*, vol. 79, no. 1, p. 013827, 2009.

[31] G. Brida, M. Genovese, and I. R. Berchera, "Experimental realization of sub-shot-noise quantum imaging," *Nat. Photonics*, vol. 4, no. 4, p. 227, 2010.

[32] S. D. Huver, C. F. Wildfeuer, and J. P. Dowling, "Entangled fock states for robust quantum optical metrology, imaging, and sensing," *Phys. Rev. A*, vol. 78, no. 6, p. 063828, 2008.

[33] P. M. Anisimov, G. M. Raterman, A. Chiruvelli, W. N. Plick, S. D. Huver, H. Lee, and J. P. Dowling, "Quantum metrology with two-mode squeezed vacuum: parity detection beats the heisenberg limit," *Phys. Rev. Lett.*, vol. 104, no. 10, p. 103602, 2010.

[34] V. Giovannetti, S. Lloyd, and L. Maccone, "Advances in quantum metrology," *Nat. Photonics*, vol. 5, no. 4, p. 222, 2011.

[35] K. R. Motes, J. P. Olson, E. J. Rabeaux, J. P. Dowling, S. J. Olson, and P. P. Rohde, "Linear optical quantum metrology with single photons: exploiting spontaneously generated entanglement to beat the shot-noise limit," *Phys. Rev. Lett.*, vol. 114, no. 17, p. 170802, 2015.

[36] T. Purdy, P.-L. Yu, R. Peterson, N. Kampel, and C. Regal, "Strong optomechanical squeezing of light," *Phys. Rev. X*, vol. 3, no. 3, p. 031012, 2013.

[37] R. Singh, G. D. Cole, J. Cripe, and T. Corbitt, "Stable optical trap from a single optical field utilizing birefringence," *Phys. Rev. Lett.*, vol. 117, no. 21, p. 213604, 2016.

[38] J. Cripe, N. Aggarwal, R. Singh, R. Lanza, A. Libson, M. J. Yap, G. D. Cole, D. E. McClelland, N. Mavalvala, and T. Corbitt, "Radiation-pressure-mediated control of an optomechanical cavity," *Phys. Rev. A*, vol. 97, no. 1, p. 013827, 2018.

[39] T. Jennewein, C. Simon, G. Weihs, H. Weinfurter, and A. Zeilinger, "Quantum cryptography with entangled photons," *Phys. Rev. Lett.*, vol. 84, no. 20, p. 4729, 2000.

[40] V. Scarani, H. Bechmann-Pasquinucci, N. J. Cerf, M. Dušek, N. Lütkenhaus, and M. Peev, "The security of practical quantum key distribution," *Rev. Mod. Phys.*, vol. 81, no. 3, p. 1301, 2009.

[41] S. Pirandola, C. Ottaviani, G. Spedalieri, C. Weedbrook, S. L. Braunstein, S. Lloyd, T. Gehring, C. S. Jacobsen, and U. L. Andersen, "High-rate measurement-device-independent quantum cryptography," *Nat. Photonics*, vol. 9, no. 6, p. 397, 2015.

[42] M. Wilde, *Quantum Information Theory*. Cambridge University Press, 2013.

[43] C. Weedbrook, S. Pirandola, R. García-Patrón, N. J. Cerf, T. C. Ralph, J. H. Shapiro, and S. Lloyd, "Gaussian quantum information," *Rev. Mod. Phys.*, vol. 84, no. 2, p. 621, 2012.

[44] C. Gerry and P. Knight, *Introductory Quantum Optics*. Cambridge University Press, 2005.

[45] A. Matsko, I. Novikova, G. Welch, D. Budker, D. Kimball, and S. Rochester, "Vacuum squeezing in atomic media via self-rotation," *Phys. Rev. A*, vol. 66, no. 4, p. 043815, 2002.

[46] E. E. Mikhailov and I. Novikova, "Low-frequency vacuum squeezing via polarization self-rotation in rb vapor," *Opt. Lett.*, vol. 33, no. 11, pp. 1213–1215, 2008.

[47] S. Barreiro, P. Valente, H. Failache, and A. Lezama, "Polarization squeezing of light by single passage through an atomic vapor," *Phys. Rev. A*, vol. 84, no. 3, p. 033851, 2011.

[48] I. H. Agha, G. Messin, and P. Grangier, "Generation of pulsed and continuous-wave squeezed light with 87 rb vapor," *Opt. Express*, vol. 18, no. 5, pp. 4198–4205, 2010.

[49] M. Reid and D. Walls, "Generation of squeezed states via degenerate four-wave mixing," *Phys. Rev. A*, vol. 31, no. 3, p. 1622, 1985.

[50] R. Slusher, L. Hollberg, B. Yurke, J. Mertz, and J. Valley, "Observation of squeezed states generated by four-wave mixing in an optical cavity," *Phys. Rev. Lett.*, vol. 55, no. 22, p. 2409, 1985.

[51] P. Kumar and M. I. Kolobov, "Degenerate four-wave mixing as a source for spatially-broadband squeezed light," *Opt. Comm.*, vol. 104, no. 4-6, pp. 374–378, 1994.

[52] C. McCormick, V. Boyer, E. Arimondo, and P. Lett, "Strong relative intensity squeezing by four-wave mixing in rubidium vapor," *Opt. Lett.*, vol. 32, no. 2, pp. 178–180, 2007.

[53] V. Boyer, A. Marino, and P. Lett, "Generation of spatially broadband twin beams for quantum imaging," *Phys. Rev. Lett.*, vol. 100, no. 14, p. 143601, 2008.

[54] N. Corzo, A. M. Marino, K. M. Jones, and P. D. Lett, "Multi-spatial-mode single-beam quadrature squeezed states of light from four-wave mixing in hot rubidium vapor," *Opt. Express*, vol. 19, no. 22, pp. 21358–21369, 2011.

[55] A. Marino, J. Clark, Q. Glorieux, and P. Lett, "Extracting spatial information from noise measurements of multi-spatial-mode quantum states," *The European Physical Journal D*, vol. 66, no. 11, p. 288, 2012.

[56] M. Holtfrerich and A. Marino, "Control of the size of the coherence area in entangled twin beams," *Phys. Rev. A*, vol. 93, no. 6, p. 063821, 2016.

[57] C. Embrey, M. Turnbull, P. Petrov, and V. Boyer, "Observation of localized multi-spatial-mode quadrature squeezing," *Phys. Rev. X*, vol. 5, no. 3, p. 031004, 2015.

[58] R. W. Boyd, *Nonlinear Optics*. Academic Press, 2003.

[59] S. Castelletto, I. P. Degiovanni, V. Schettini, and A. Migdall, "Spatial and spectral mode selection of heralded single photons from pulsed parametric down-conversion," *Opt. Express*, vol. 13, no. 18, pp. 6709–6722, 2005.

[60] G. Brida, I. P. Degiovanni, M. Genovese, M. L. Rastello, and I. Ruo-Berchera, "Detection of multimode spatial correlation in pdc and application to the absolute calibration of a ccd camera," *Opt. Express*, vol. 18, no. 20, pp. 20572–20584, 2010.

[61] S. P. Walborn, C. Monken, S. Pádua, and P. S. Ribeiro, "Spatial correlations in parametric down-conversion," *Phys. Rep.*, vol. 495, no. 4-5, pp. 87–139, 2010.

[62] K. Y. Spasibko, T. S. Iskhakov, and M. V. Chekhova, "Spectral properties of high-gain parametric down-conversion," *Opt. Express*, vol. 20, no. 7, pp. 7507–7515, 2012.

[63] P. Sharapova, A. M. Pérez, O. V. Tikhonova, and M. V. Chekhova, "Schmidt modes in the angular spectrum of bright squeezed vacuum," *Phys. Rev. A*, vol. 91, no. 4, p. 043816, 2015.

[64] S. Castelleto, I. P. Degiovanni, A. Migdall, and M. Ware, "On the measurement of two-photon single-mode coupling efficiency in parametric downconversion photon sources," *N. J. Phys.*, vol. 6, p. 87, 2004.

[65] H. E. Guilbert and D. J. Gauthier, "Enhancing heralding efficiency and biphoton rate in type-i spontaneous parametric down-conversion," *IEEE Journal of Selected Topics in Quantum Electronics*, vol. 21, no. 3, pp. 215–224, 2015.

[66] J. Schneeloch and J. C. Howell, "Introduction to the transverse spatial correlations in spontaneous parametric down-conversion through the biphoton birth zone," *J. Opt.*, vol. 18, no. 5, p. 053501, 2016.

[67] X. Ma and W. Rhodes, "Multimode squeeze operators and squeezed states," *Phys. Rev. A*, vol. 41, no. 9, p. 4625, 1990.

[68] R. S. Bennink and R. W. Boyd, "Improved measurement of multimode squeezed light via an eigenmode approach," *Phys. Rev. A*, vol. 66, no. 5, p. 053815, 2002.

[69] A. Zangwill, *Modern electrodynamics*. Cambridge University Press, 2013.

[70] A. Siegman, *Lasers*. University Science Books, Sausalito CA, 1986.

[71] T. Horrom, R. Singh, J. P. Dowling, and E. E. Mikhailov, "Quantum-enhanced magnetometer with low-frequency squeezing," *Phys. Rev. A*, vol. 86, p. 023803, Aug 2012.

[72] S. Barreiro, P. Valente, H. Failache, and A. Lezama, "Polarization squeezing of light by single passage through an atomic vapor," *Phys. Rev. A*, vol. 84, p. 033851, Sep 2011.

[73] M. Zhang, J. Soultanis, I. Novikova, and E. E. Mikhailov, "Generating squeezed vacuum field with nonzero orbital angular momentum with atomic ensembles," *Opt. Lett.*, vol. 38, pp. 4833–4836, Nov 2013.

[74] B. E. Saleh, M. C. Teich, and B. E. Saleh, *Fundamentals of photonics*. Wiley New York, 1991.

[75] G. Barton, *Elements of Green's Functions and Propagation*. Oxford University Press, New York NY, 1989.

[76] Z. Xiao, R. N. Lanning, M. Zhang, I. Novikova, E. E. Mikhailov, and J. P. Dowling, "Why a hole is like a beam splitter: A general diffraction theory for multimode quantum states of light," *Phys. Rev. A*, vol. 96, no. 2, p. 023829, 2017.

[77] Z. Xiao, "Multimode approach to classical and quantum diffraction," *LSU Doctoral Dissertations*, no. 4178, 2017.

[78] A. Lezama, P. Valente, H. Failache, M. Martinelli, and P. Nussenzveig, "Numerical investigation of the quantum fluctuations of optical fields transmitted through an atomic medium," *Phys. Rev. A*, vol. 77, no. 1, p. 013806, 2008.

[79] T. Horrom, A. Lezama, S. Balik, M. D. Havey, and E. E. Mikhailov, "Quadrature noise in light propagating through a cold 87rb atomic gas," *J. of M. Opt.*, vol. 58, no. 21, pp. 1936–1941, 2011.

[80] S. Gröblacher, T. Jennewein, A. Vaziri, G. Weihs, and A. Zeilinger, "Experimental quantum cryptography with qutrits," *N. J. Phys.*, vol. 8, no. 5, p. 75, 2006.

[81] M. Mirhosseini, O. S. Magana-Loaiza, M. N. OSullivan, B. Rodenburg, M. Malik, M. P. Lavery, M. J. Padgett, D. J. Gauthier, and R. W. Boyd, "High-dimensional quantum cryptography with twisted light," *N. J. Phys.*, vol. 17, no. 3, p. 033033, 2015.

Appendix A Green's Function Solution Method

In Section 3.1, we introduced our spatial mode propagation equation and constructed an IVP to restate the problem in a compact form. The first step in solving our inhomogeneous IVP [Eq. (3.2)] is to solve the homogeneous IVP in free space, i.e., for $\wp = 0$:

$$\begin{aligned} \text{DE}: &\ \hat{L}\mathcal{E} = 0 \\ \text{IV}: &\ \mathcal{E}_0. \end{aligned} \tag{A.1}$$

Using a Green function method [75], we search for a propagator K defined by

$$\hat{L}\ K(\mathbf{r} \mid \mathbf{r}') = 0 \quad (z > z') \tag{A.2a}$$

$$K(\mathbf{r} \mid \mathbf{r}') = \delta(r - r')\delta(\phi - \phi') \quad (z = z') \tag{A.2b}$$

$$K \to 0 \quad (r \to \infty), \tag{A.2c}$$

such that when K is known, the homogeneous problem is solved:

$$\mathcal{E}_{\text{hom}} = \int r'dr'd\phi'\ K(\mathbf{r} \mid \mathbf{r}')\mathcal{E}_0(\mathbf{r}')\ |_{z=z'}. \tag{A.3}$$

The $z = z'$ restraint is a standard condition placed by the boundary conditions which define the propagator, i.e., Eq. (A.2b).

Proof. We check our solution Eq. (A.3) by operating the differential operator $\hat{L}$ and find

$$\begin{aligned} \hat{L}\mathcal{E}_{\text{hom}} &= \int r'dr'd\phi' \left(\hat{L}\ K(\mathbf{r} \mid \mathbf{r}')\right) \mathcal{E}_0(\mathbf{r}') \\ &= \int r'dr'd\phi' \left(0\right) \mathcal{E}_0(\mathbf{r}') \\ &= 0. \end{aligned} \tag{A.4}$$

The second line follows trivially since the propagator K obeys Eq. (A.2a). Thus we see $\mathcal{E}_{\text{hom}}$ is a solution to Eq. (A.1). ■

To proceed, we recognize the property in Eq. (3.7) and explicitly define our propagator in terms of the LG modes:

$$K(r,\phi,z|r',\phi',z') \equiv \sum_{\ell,p} u^*_{\ell,p}(r',\phi',z')u_{\ell,p}(r,\phi,z). \tag{A.5}$$

Inserting Eq. (A.5) into Eq. (A.2), we verify our choice of the propagator:

$$\hat{L}\,K = \sum_{\ell,p} u^*_{\ell,p}(\mathbf{r}')\big(\hat{L}\,u_{\ell,p}(\mathbf{r})\big) = 0 \quad (z > z') \tag{A.6a}$$

$$K(\mathbf{r} \mid \mathbf{r}') = \delta(r-r')\delta(\phi-\phi') \quad (z = z') \tag{A.6b}$$

$$u_{\ell,p} \to 0 \implies K \to 0 \quad (r \to \infty). \tag{A.6c}$$

Therefore, the homogeneous problem is solved, and we can turn our attention back to the inhomogeneous problem Eq. (3.2).

To solve the inhomogeneous problem, again in free space, we need a Green function G defined by

$$\hat{L}\,G(\mathbf{r} \mid \mathbf{r}') = \delta(r-r')\delta(\phi-\phi')\delta(z-z') \tag{A.7a}$$

$$G(\mathbf{r} \mid \mathbf{r}') = 0 \quad (z < z') \tag{A.7b}$$

$$G \to 0 \quad (r \to \infty), \tag{A.7c}$$

such that when G is known, the inhomogeneous problem is solved:

$$\mathcal{E} = \int r'dr'd\phi'dz'\, G(\mathbf{r}\,|\,\mathbf{r}')\wp(\mathbf{r}'). \tag{A.8}$$

Proof. We check our solution Eq. (A.8) by operating the differential operator $\hat{L}$ and find

$$\begin{aligned}\hat{L}\mathcal{E} &= \int r'dr'd\phi'dz' \left(\hat{L}\, G(\mathbf{r}\,|\,\mathbf{r}')\right) \wp(\mathbf{r}') \\ &= \int r'dr'd\phi'dz'\, \delta(\mathbf{r}-\mathbf{r}')\, \wp(\mathbf{r}') \\ &= \wp(\mathbf{r}).\end{aligned} \tag{A.9}$$

The second line follows from our definition of the Green function, Eq. (A.7a), and the third line follows trivially from the definition of the Dirac delta function. Thus we see $\mathcal{E}$ is a solution to Eq. (3.2). ■

Building on the method for solving the homogeneous problem, we explicitly define our Green function G in terms of the LG modes

$$G(r,\phi,z|r',\phi',z') \equiv \Theta(z-z')K(r,\phi,z|r',\phi',z'), \tag{A.10}$$

where $\Theta(z-z')$ is the Heaviside step function. Next, inserting Eq. (A.10) into Eq. (A.7), we verify our choice of Green function:

$$\begin{aligned}\hat{L}\, G &= (\frac{\partial}{\partial z} - \frac{i}{2k}\nabla_\perp^2)\Theta(z-z')K(r,\phi,z|r',\phi',z') \\ &= K\frac{\partial}{\partial z}\Theta(z-z') + \Theta\frac{\partial}{\partial z}K - \Theta\frac{i}{2k}\nabla_\perp^2 K \\ &= K\delta(z-z') + \Theta(z-z')\,(\frac{\partial}{\partial z}K - \frac{i}{2k}\nabla_\perp^2 K) \\ &= K\delta(z-z') + \Theta(z-z')\,\hat{L}K \\ &= \delta(r-r')\delta(\phi-\phi')\delta(z-z'),\end{aligned} \tag{A.11}$$

and thus we see that Eq. (A.7a) is satisfied, secondly, Eq. (A.7b) is satisfied since we know $G|_{z<z'} = 0$, by definition of the Heaviside function, and lastly, Eq. (A.7c) is satisfied since $r \to 0 \implies u_{\ell,p} \to 0 \implies G \to 0$. Therefore, we have derived a valid propagator and Green function and can now write the final solution by combining our two previous solutions Eq. (A.3) and Eq. (A.8). However, we would first like to simplify the notation in Eq. (A.8). It

is likely that the source $\wp$ doesn't contribute until some position $z' = z_i$, and for $z > z' = z_i$, the Heaviside function reduces to 1, leaving only the propagator K. Furthermore, the source likely only contributes up to some position z_f and thus we may safely modify the dz integral. With these final considerations, we can write the complete solution to Eq. (3.2):

$$\begin{aligned}\mathcal{E} &= \int r'dr'd\phi'\, K(\mathbf{r}\,|\,\mathbf{r}')\mathcal{E}_0(\mathbf{r}')\,|_{z=z'} + \int_{z_i}^{z_f} dz' \int r'dr'd\phi'\, K(\mathbf{r}\,|\,\mathbf{r}')\wp(\mathbf{r}') \\ &= \mathcal{E}_0 + \sum_{\ell,p} u_{\ell,p}(\mathbf{r}) \int_{z_i}^{z_f} dz' \int r'dr'd\phi'\, u^*_{\ell,p}(\mathbf{r}')\wp(\mathbf{r}').\end{aligned} \tag{A.12}$$

Although the problem is solved, we can further employ the LG modes to simplify our calculations. Suppose we expand the nonlinear source in terms of the LG modes, i.e.,

$$\wp(r,\phi,z) = \sum_{\ell,p} c_{\ell,p}(z)\, u_{\ell,p}(r,\phi,z), \tag{A.13}$$

where $c_{\ell,p}(z) = \int rdrd\phi\, u^*_{\ell,p}(r,\phi,z)\wp(r,\phi,z)$. One should notice that, in contrast to expanding an arbitrary Gaussian beam in terms of the LG modes, the expansion coefficients for a nonlinear source distribution *are not independent of the position* z. Thus, each infinitesimal slice of the source contributes to the new field $\mathcal{E}$ in the following way. We insert Eq. (A.13) into Eq. (A.12) and invoke the orthogonality of the LG modes one last time to arrive at

$$\mathcal{E}(\mathbf{r}) = \mathcal{E}_0(\mathbf{r}) + \sum_{\ell,p} u_{\ell,p}(\mathbf{r}) \int_{z_i}^{z_f} dz' c_{\ell,p}(z'). \tag{A.14}$$

This result corresponds to Eq. (3.11) from the main text.

Lastly, we emphasize the z-dependence of the $c_{\ell,p}$ coefficients, which represent the amplitudes of the new mode structure of the beam. On one hand, these coefficients allow one to study how the new beam evolves during the interaction in the nonlinear medium. On the other, in the case that the first Born approximation does not hold, one can use this theory for successive iterations. For example, if the pump beam is known to be modified by the nonlinear material, then one can model this by a propagation equation for the pump, and

use the solution as a second Born approximation for the new frequency components of the field, i.e.,

$$\wp(\mathcal{E}_0) \rightarrow \wp(\mathcal{E}_1) = \wp\Big(\mathcal{E}_0 + c_{\ell,p}(z)\, u_{\ell,p}(\mathbf{r})\Big), \tag{A.15}$$

where in this case, $c_{\ell,p}$ are the result of a propagation equation for the pump.

Appendix B Two-Photon Amplitude Matrix

We define the two photon amplitude matrix in such as way that it extends over the azimuthal modes, from negative to positive, and increments the radial index along the way:

$$\boldsymbol{\chi} \equiv \sum_{ijvw} \hat{e}_{i+1} \otimes \hat{e}_{j+1}\, \chi_{i-\ell_{\max},j;k-v_{\max},w}\, [\hat{e}_{v+1} \otimes \hat{e}_{w+1}]^T, \tag{B.1}$$

where $\hat{e}_i$ is a vector with one in the i'th position, and the sum runs over $0 \leq i \leq 2\ell_{\max}+1$, $0 \leq j \leq p_{\max}$, $0 \leq v \leq 2m_{\max}+1$, and $0 \leq w \leq q_{\max}$. This operational notation may not be clear, so we also include $\boldsymbol{\chi}$ in matrix notation

$$\boldsymbol{\chi} = \begin{pmatrix} \chi_{\ell,p;m,q} & \chi_{\ell,p;m,q+1} & \cdots & \chi_{\ell,p;m+1,q} & \chi_{\ell,p;m+1,q+1} & \cdots \\ \chi_{\ell,p+1;m,q} & \chi_{\ell,p+1;m,q+1} & \cdots & \chi_{\ell,p+1;m+1,q} & \chi_{\ell,p+1;m+1,q+1} & \cdots \\ \vdots & \vdots & & \vdots & \vdots & \\ \chi_{\ell+1,p;m,q} & \chi_{\ell+1,p;m,q+1} & \cdots & \chi_{\ell+1,p;m+1,q} & \chi_{\ell+1,p;m+1,q+1} & \cdots \\ \chi_{\ell+1,p+1;m,q} & \chi_{\ell+1,p+1;m,q+1} & \cdots & \chi_{\ell+1,p+1;m+1,q} & \chi_{\ell+1,p+1;m+1,q+1} & \cdots \\ \vdots & \vdots & & \vdots & \vdots & \end{pmatrix}. \tag{B.2}$$

where $\ell = -\ell_{\max}$ and $p = 0$ are the lowest order modes to be investigated. For example, if a particular simulation required the investigation of $-1 \leq \ell \leq 1$ and $0 \leq p \leq 2$, then we would begin incrementing from $\ell = m = -1$ and $p = q = 0$.

Appendix C Copyright Information

Please see the figure below regarding the American Physical Society copyright policy, taken from https://journals.aps.org/copyrightFAQ.html.

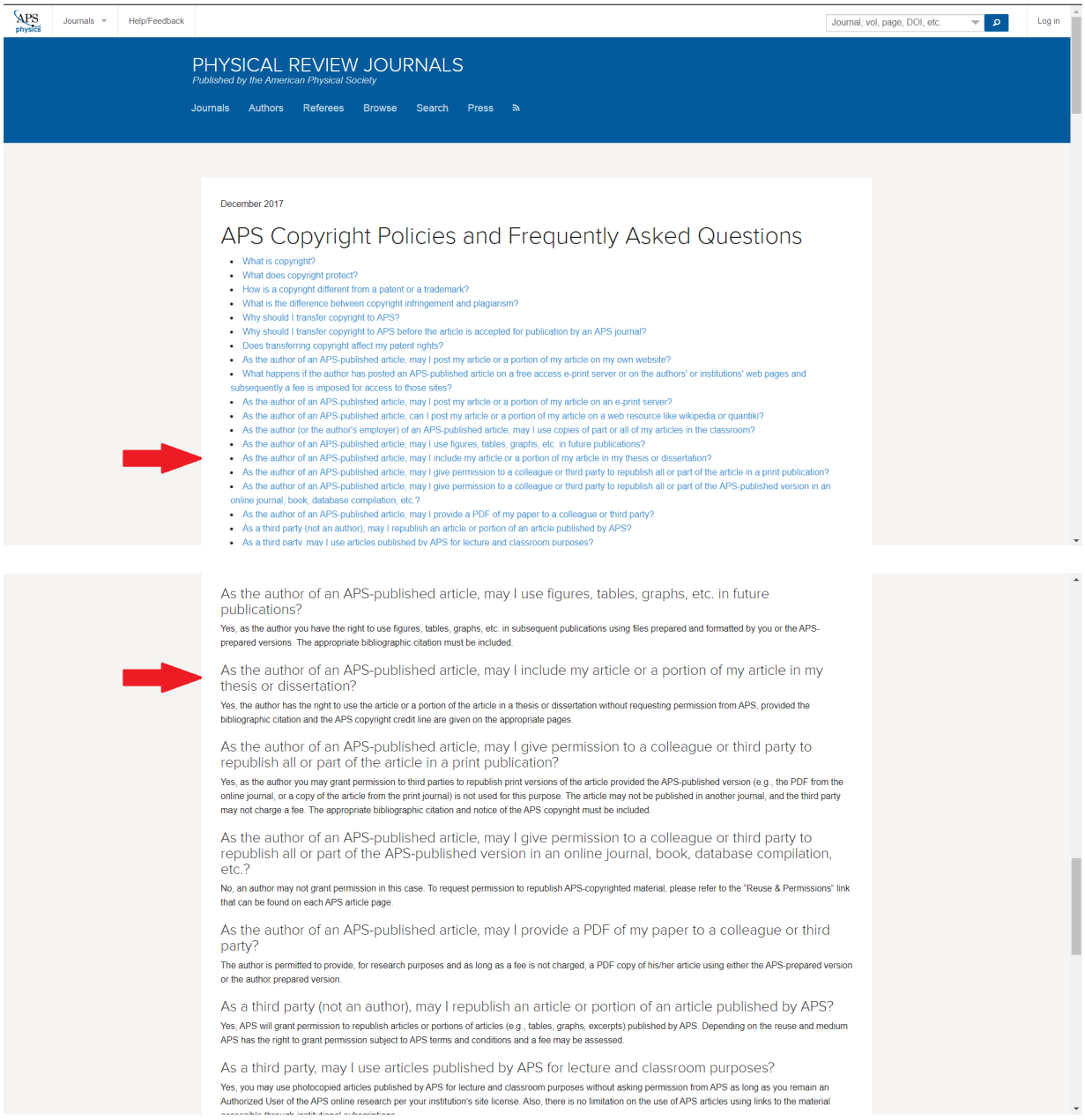

Figure C.1. The American Physical Society copyright policy regarding the use of copyrighted articles in the thesis or dissertation of an author. Please see the red arrows which indicate the policies relevant to this thesis.

Vita

Robert Nicholas Lanning was born in 1981 and grew up in Orange, TX. He worked in the auto-accessory business until 2008 when he decided to go back to school to pursue a degree in physics. He graduated from Lamar University in 2012 with a B.S. in physics and a B.S. in mathematics. Thereafter, he taught physics at Lamar State College Port Arthur for two semesters while applying to graduate schools. He chose LSU such that he could join the Quantum Science and Technologies Group and work under the supervision of Jonanthan P. Dowling. In his spare time, Nick enjoys playing with his son, playing guitar, and racing motorcycles in Baja California, Mexico.